UNIVERSITÀ DEGLI STUDI DI BERGAMO

PROCEEDINGS OF THE DIPSI WORKSHOP 2018

Droplet Impact Phenomena & Spray Investigations

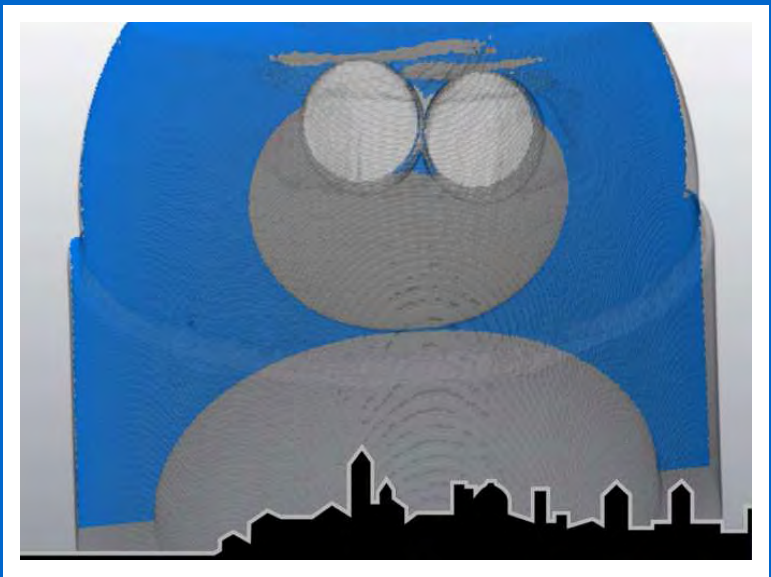

X-ray microCT of 3D multiple interfaces: two glass spheres and a water drop in dodecane

BERGAMO, ITALY, 18TH MAY 2018

UNIVERSITÀ DEGLI STUDI DI BERGAMO

PROCEEDINGS OF THE DIPSI WORKSHOP 2018

Droplet Impact Phenomena & Spray Investigations

BERGAMO, ITALY, 18TH MAY 2018

PROCEEDINGS OF THE DIPSI WORKSHOP 2018
Droplet Impact Phenomena & Spray Investigations

Editors
Gianpietro Elvio Cossali and Simona Tonini
Department of Engineering and Applied Sciences
Università degli Studi di Bergamo
Viale Marconi 5, 24044 Dalmine, Italy
e-mail: elvio.cossali@unibg.it
simona.tonini@unibg.it

p. 60 - cm 29,7
ISBN – 978-88-97413-27-1

Preface

This Book of Proceedings contains the extended abstracts of the contributions presented at the DIPSI Workshop 2018 on Droplet Impact Phenomena and Spray Investigation, organised by the Università degli Studi di Bergamo on Friday 18th May 2018 in Bergamo, Italy.

This workshop, which is now at its twelfth edition, represents an important opportunity to share the recent knowledge on droplets and sprays in a variety of research fields and industrial applications.

The event is supported by the Department of Engineering and Applied Sciences of the Università degli Studi di Bergamo, the Research Training Group 2160/1 DROPIT, University of Stuttgart, Luchsinger S.r.l. and EyePro System S.r.l.

Bergamo, September 2018

Prof. Gianpietro Elvio Cossali

Contents

The effect of injector shearing of water-in-diesel emulsion on micro-explosion behaviour

M.R. Heikal*[1,2], Mhadi A. Ismael[1], A. Rashid A. Aziz[1], Cyril Crua[2]
[1]Center for Automotive Research and Electric Mobility, Universiti Teknologi PETRONAS, Perak, Malaysia
[2]Advanced Engineering Centre, University of Brighton, Brighton BN2 4GJ, United Kingdom
*Corresponding author: mrh@brighton.ac.uk

Introduction

One of the possible and promising ways for reducing both nitrogen oxides (NOx) and particulate matter (PM) in diesel engines is the use of the water-in-diesel emulsions which have been investigated by different researchers [1].It is generally accepted that when water in diesel emulsion is subjected to high temperature in the combustion chamber, secondary atomization occurs resulting in a reduction in emissions and lower specific fuel consumption. This is attributed mainly to the phenomena of micro-explosion as suggested by different authors [2]. Micro-explosion is caused by the exposure of the primary emulsion droplet to a high-temperature environment whereby the small water droplets dispersed inside the fuel vaporize earlier than the fuel shattering the emulsion droplet into many smaller droplets known as droplets [3]. The smaller droplets tend to evaporate more quickly and form a better air-fuel mixture.

Previous observations of the occurrence of micro-explosion for isolated emulsion droplets showed that these events are influenced significantly by the number and size distributions of the dispersed phase. Fine dispersed droplets (1-2 μm diameter) did not give rise to micro-explosion[4], and the optimum dispersed droplet size was found to be of the order of 5 μm [5].The reason for fine dispersed water droplets to inhibit or delay micro-explosion is believed to be due to their lower coalescence rate [6]. A limitation of these direct observation of micro-explosion events is that the size of the isolated dispersed water (emulsion) droplets tend to be several orders of magnitude larger than the droplets found in typical diesel sprays.

There is, however, a great deal of disagreement on the performance of emulsions in engines. We believe that this may be due to the effect of the FIE equipment on the size and number distribution of the dispersed phase in the emulsion. Emulsions are subjected to intense shear in the fuel pump and injector nozzle which may lead to change in the distributions and sizes of the emulsion droplets [7]. This study was aimed investigating the impact of injector nozzle on dispersed water and thereby, its effect on micro-explosion and hence the combustion performance of the engine.

Material and methods

Emulsion preparation

The emulsions were custom-blended for this study with a mechanical stirrer using a reference diesel fuel, surfactant (Span 80) and water concentrations of 15% by volume. The emulsion properties are shown in Table 1.

Table 1. Water In diesel emulsion properties

Fuel/ Emulsion	Density at 25 ºC (Kg/m3)	Viscosity at 40 ºC (mm2/s)	Surface Tension at 25 °C (N/m)	Cal. value (MJ/Kg)
Neat diesel	825.01	3.21	43.20	27.08
15%W	856.12	9.44	37.20	26.75

Experimental setup

Two experimental setups were used in the current study. Firstly, a common-rail, electronically-controlled injection system was used to generate and induce the high pressure sprays into the sample collector to investigate the impact of the injection nozzle orifice on the properties of the emulsion. The emulsions were examined using a digital microscope (Olympus BX51) with 50× magnification and 10 μm depth of field to acquire high-magnification images of the dispersed water droplets. A developed MATLAB image processing algorithm was used to detect and measure dispersed water droplet sizes.

Secondly, the collected emulsions from the spray (at injection pressures of 50, 100, 150 MPa) were suspended over a hot plate at Lidenfrost conditions using a micro syringe needle to visualize the droplet micro-explosion phenomena. The complete setup for the experiments including the visualization system and temperature recording are shown in Figure 1. A National Instrument controller was employed to trigger the high-speed camera for image capturing and recording of the measured temperatures of the suspended emulsion droplet. The image acquisition rate was set at 500 fps at a resolution of 1280 × 1024 pixels throughout the experiments.

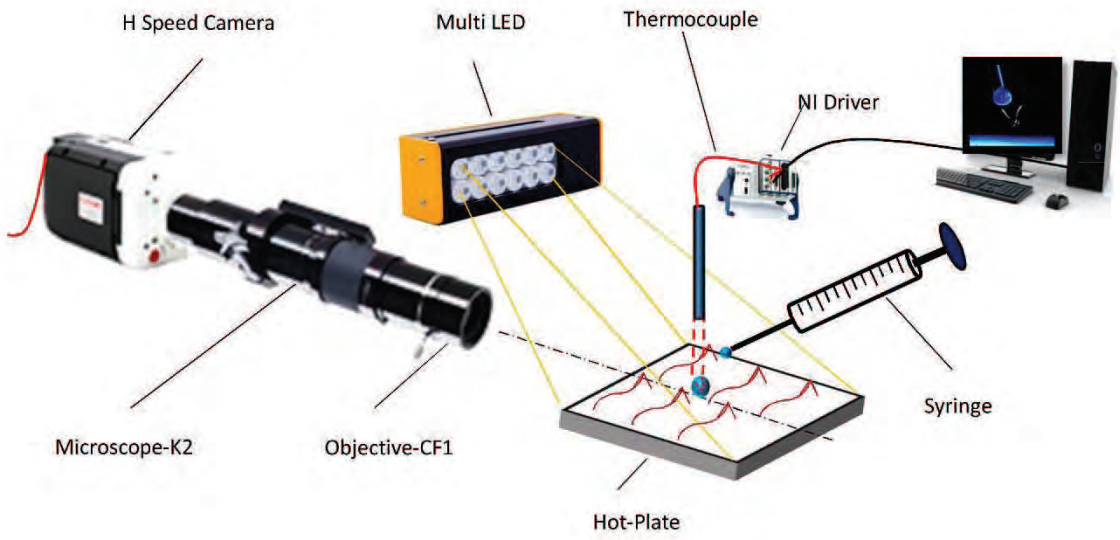

Figure 1. Experimental setup for single droplet micro-explosion

Results and Discussion

Impact of injector nozzle on the dispersed droplet size

Figure 2 shows the effect of injector nozzle shear on a water-in-diesel emulsion made with 15%W in the fuel tank (1 bar) and different injection pressure as seen under an optical microscope at 50X magnification. The injector nozzle shifted the emulsion distributions' modes to a smaller diameter and the dispersed water droplet size decreased steadily with the increase in injection pressure. This is caused by the elevated shear and temperatures exerted by the injector's nozzle onto the emulsion.

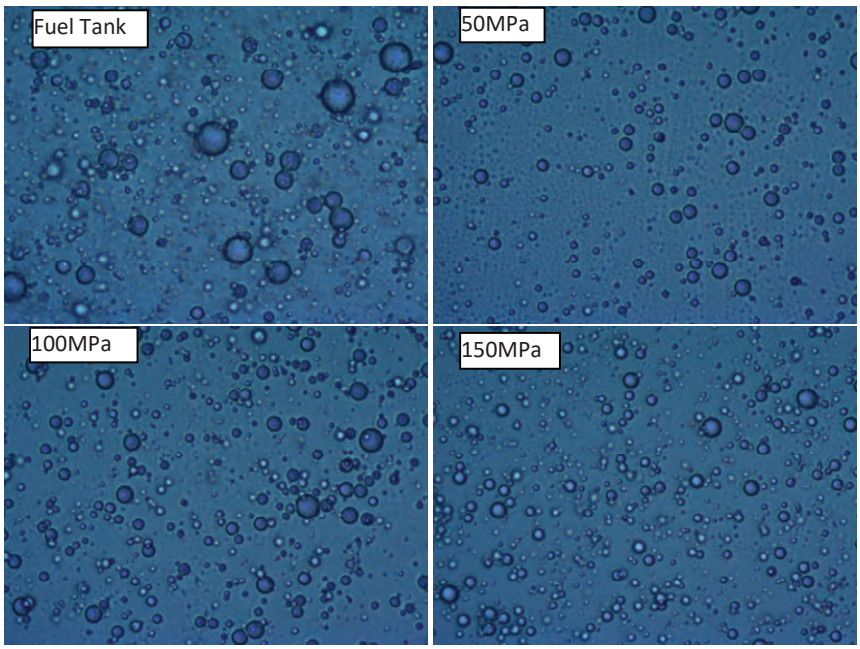

Figure 2. Images of water-in-diesel emulsion samples for 15%v/v water content, examined under an optical microscope at 50× magnification for the emulsion in the fuel tank, and after injection at 50, 100 and 150 MPa.

To ascertain whether the emulsion's water had separated out of the blends we measured the density of the samples, and then used a mixing model to compute the water concentration for each sample. Figure 3 shows the effect of different injection pressures on water concentration. As the water concentration is linearly related to the emulsion's density, this result indicates that some water separated or evaporated out of the emulsion. With the increase of injection pressure, the water concentration was reduced. The loss of water during the injection can be attributed to high temperature and pressure in the injector orifice causing the water evaporation. This evaporation can be attributed to the NOx reduction inside the engine.

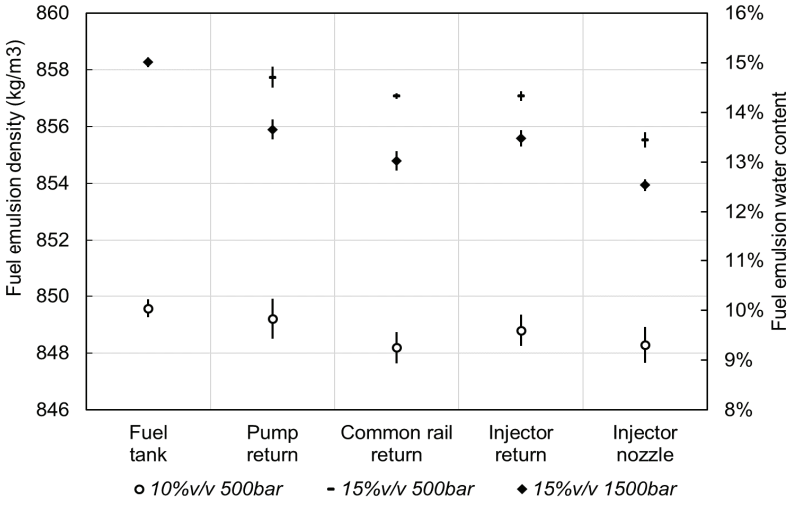

Figure3. Effect of the injection pressure on the density of the emulsified fuel and the water content in the emulsion.

Impact of injector nozzle on micro-explosion behavior

Figure 4 shows image sequences of a droplet for the evolution of micro-explosion phenomena of emulsion made with 15% water concentration by volume. Samples from the fuel tank (A) and after the injection pressure at 150MPa were tested at the Leidenfrost conditions to determine the effect of injection pressure on the micro-explosion phenomena. The results showed that the micro-explosion behavior was significantly affected by the injector shearing, hence. With the increase of injection pressure, micro-explosion time was delayed (from 1.4s in the fuel tank to 2.5 after the injector at 150 MPa) due to reduction in dispersed water droplet size and water content in the emulsion.

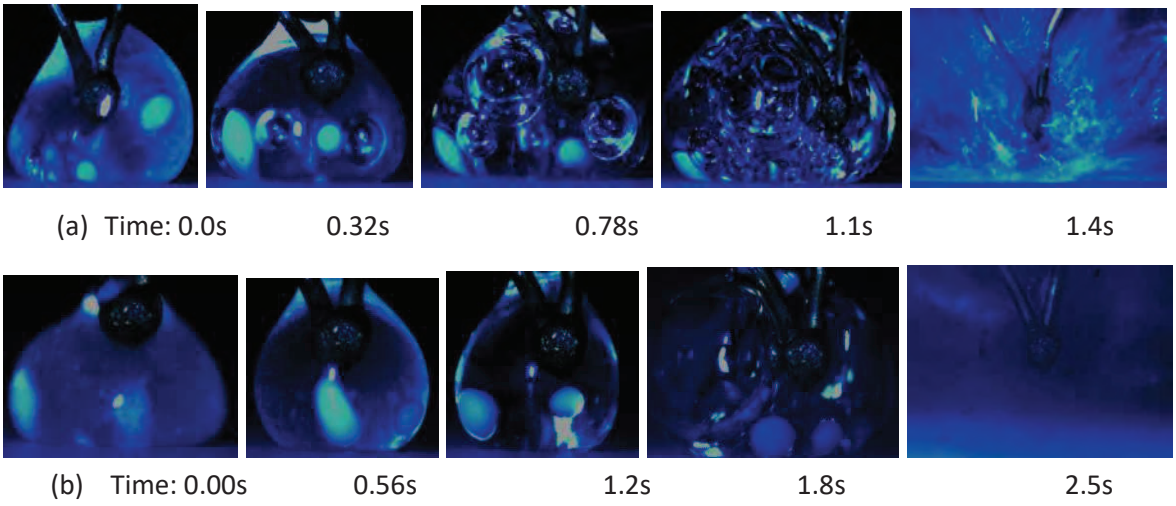

Figure 4. Sequences of images showing micro-explosion behavior of an emulsion made with 15% water content taken from the tank (a) and after the injection at 150 MPa (b).

References

[1] Lif A, Holmberg K. Water-in-diesel emulsions and related systems. Adv Colloid Interface Sci 2006;123–126:231–9. doi:10.1016/j.cis.2006.05.004.

[2] Shinjo J, Xia J, Megaritis A, Ganippa LC. Secondary atomization and vapor mixing characteristics of diesel / biodiesel / bioethanol fuel droplets due to puffing / microexplosion 2015:1–8.

[3] Kadota T, Tanaka H, Segawa D, Nakaya S, Yamasaki H. Microexplosion of an emulsion droplet during Leidenfrost burning. Proc Combust Inst 2007;31 II:2125–31. doi:10.1016/j.proci.2006.07.001.

[4] Kimoto, K., Owashi, Y., & Omae Y. The vaporizing behavior of the fuel droplet of water-in-oil emulsion on the hot surface. Bull JSME 1986;258:4247–55. doi:10.1248/cpb.37.3229.

[5] Mura E, Josset C, Loubar K, Huchet G, Bellettre J. Effect of dispersed water droplet size in microexplosion phenomenon for water in oil emulsion. At Sprays 2010;20:791–9. doi:10.1615/AtomizSpr.v20.i9.40.

[6] Khan MY, Karim ZAA, Aziz ARA, Morgan R, Crua C. Puffing and Microexplosion Behavior of Water in Pure Diesel Emulsion Droplets During Leidenfrost Effect Pu ffi ng and Microexplosion Behavior of Water in Pure Diesel. Combust Sci Technol 2017;189:1186–97. doi:10.1080/00102202.2016.1275593.

[7] Mohan S, Narsimhan G. Coalescence of Protein-Stabilized Emulsions in a High-Pressure Homogenizer 1997;15:1–15.

Influence of solubility effects and diffusion coefficient models on the drop vaporization rate at high pressure

G. Lamanna*[1], C. Steinhausen[1], P. Palmetshofer[1], B. Weigand[1]
Institute of Aerospace Thermodynamics, University of Stuttgart, Germany
*Corresponding author: grazia.lamanna@itlr.uni-stuttgart.de

Introduction

In modern rocket engines, gas turbines and internal combustion engines, fluids are injected in a high pressures atmosphere at fuel states either close to or exceeding the critical point. Under these conditions, fuel droplets may experience a thermodynamic transition into a supercritical state during thier lifetime. Comprehensive reviews on the subject can be found in Givler and Abraham [1] Yang [2] and in Bellan [3]. Recently, Crua et al. [4] introduced an empirical regime map to predict the transition of microscopic droplets from classical evaporation to the diffusive mixing regime. In the present work, we analyze the influence of solubility effects and of diffusion coefficient models on the droplet vaporisation rate.

Influence of diffusion coefficient models

Most diffusion models used in droplet evaporation studies are based on an expression derived from the Chapman-Enskog or the hard-spheres theory [5]. At low and moderate pressures, the binary diffusion coefficient ($\mathcal{D}$) is inversely proportional to pressure (or density) variations and directly proportional to temperature with exponents varying in the range $1.5 < n < 1.75$. This dependency can be found in the correlations of Wilke & Lee (WL) and Fuller et al. (FSG) [5] and it basically implies that, for a given temperature, the product $\rho\mathcal{D}$ is constant. At high pressure, the product $(\rho\mathcal{D})$ is no longer constant but decreases with increasing density, due to gas non-idealities and mixture composition effects. Several approaches have been proposed to model these more complex dependencies. Lito et al. [6] introduced a correlation based on Chapman-Enskog theory, especially tailored for application to supercritical fluid extraction. Alternatively, ideal diffusion coefficient models are corrected by including empirical factors that include an explicit density and composition dependence. In this context, Riazi et al. [7] introduced a density-dependent and a viscosity-dependent correction factors. Harstad and Bellan [8], instead, employed a kinetic theory expression similar to Wilke & Lee. The correlation is then corrected by two empirical factors that have been fitted to experimental data. Finally, Krishna and van Baten [9] proposed a thermodynamic correction factor Γ that results in a reduction of the effective diffusion coefficient close to the critical point or close to the binodal curve. According to [9], the binary diffusion coefficient can be expressed as

$$\mathcal{D} = \mathcal{D}_{id} Z \Gamma \tag{1}$$

where Z is the compressibility that describes the deviation of a real gas from ideal gas behavior. The correction factor Γ is defined as

$$\Gamma = 1 + x_g \, \partial \ln \phi_g / \partial x_g \tag{2}$$

where x_g is the gas mole fraction and ϕ_g represents the gas fugacity coefficient. An overview of the different models is provided in Table 1.

Influence of solubility effects

For a quantitative description of solubility effects, one can introduce the so-called enhancement factor f_e. The latter represents the increase in the vapour saturation pressure due to the solubility of an inert gas in the liquid phase and it is defined as

$$f_e = y_{v,eq} \, p / p_{v,sat} \tag{3}$$

Table 1. Overview of binary diffusion coefficient models and relative correction factors. $\Omega(p)$ is the collision integral and E_d is a mixture specific energy parameter fitted to experimental data, $\omega(\rho)$ is a reduced density dependent high-pressure correction factor, p_c is the critical pressure and F is a correction factor.

	Ideal gas	p-dependence	T-dependence	x-dependence
Wilke-Lee [5]	Yes	p^{-1}	$T^{1.5}$, $\Omega(p)$	none
Fuller et al. (FSG) [5]	Yes	p^{-1}	$T^{1.75}$	none
Riazi et al. [7]	No	$\rho(p)$	$\mu(T)/\mu_{id}(T)$, $\mathcal{D}_{id}(T)$, $\rho_{id}(T)/\rho(T)$	$\mu(x)/\mu_{id}(x)$, $p_c(x)$, $\rho_{id}(x)/\rho(x)$
Harstad-Bellan [8]	No	$\rho(p)$	$T^{0.5}$, $\rho(T)$, $\Omega(p)$	$\rho(x)$, $\omega(\rho)$
Lito et al. [6]	No	$\rho(p)$	T, $\rho(T)$, $exp[(-E_d)/(R_gT))]$	$\rho(x)$, $F(\rho)$
Z-corr. FSG [9]	No	p^{-1}, $Z(p)$	$T^{1.75}$, $Z(T)$	$Z(x)$
Γ / Z -corr. FSG [9]	No	p^{-1}, $Z(p)$	$T^{1.75}$, $Z(T)$	$Z(x)$, $\Gamma(x)$

where $y_{v,eq}$ represent the equilibrium vapor mass fraction at the droplet interface and $p_{v,satt\,he}$ saturation pressure of the pure vapor. The enhancement factor takes into account the following effects, namely non-idealities in the liquid and gaseous phase, inert gas mole fraction dissolved in the liquid phase and the so-called Poynting effect. The latter represents the sorrection to the equilibrium mass fraction $y_{v,eq}$ due to the high-pressure conditions. Taking into account that the driving force for phase transition is the difference in chemical potential, the Gibbs-Duhem relation yields:

$$\Delta\mu = v(\Delta p_v) - s\Delta T \tag{4}$$

where $\Delta p_v = (p_{v,s} - p_{v\infty})$. Being $p_{v,s} = y_{v,eq}\, p = f_e\, p_{v,sat}$, it follows that solubility effects may lead to a significant increase of the rate of vaporization, when f_e is larger than one. Note that the above definition of the enhancement factor relies on a binary fluid phase-equilibrium calculation. Basically, for a given ambient pressure and temperature, it assumes that the inert gas dissolves instantaneously in the liquid drop. In reality, the actual vapor mass fraction ($y_{v,eff} \neq y_{v,eq}$) depends upon the rate of inert gas diffusion in the liquid phase. Given the uncertainty in the modelling of binary diffusion coefficients in compressible liquids, no accurate and reliable estimate of $y_{v,eff}$ can be currently obtained.

Results and Discussion

The present section is organized as follows. First, the accuracy of the different binary diffusion coefficient models - listed in Table 1 - is analyzed by including a direct comparison with the available experimental data. Second, the influence of binary diffusion coefficient models on solubility effects and consequently on the droplet vaporization rate is discussed. Third the possible evolution path of the droplet state is analyzed from a thermodynamic point of view.

As can be seen in Figure 1(a), the pressure dependence is well described over a large range of pressure by all models considered. Deviations from the ideal gas (alias p^{-1}) trend are observed only at chamber pressures as high as 800-1000 bar. Note, in addition, that Γ-corrected $\mathcal{D}_{id}$-models are as accurate as the Lito et al.'s model [6], developed specifically for supercritical fluids. A good agreement throughout the entire pressure range is provided only by the Harstad & Bellan correlation [8], which is fitted to the experimental data. Larger discrepancies are observed when considering the temperature dependence. As shown in Figure 1(b), ideal models (e.g. Wilke/Lee or Fuller et al.) greatly overestimate the experimental values for the binary diffusion coefficient close to the critical mixture temperature. At the same time, the introduction of the Γ-correction to $\mathcal{D}_{id}$-models results in a considerable improvement in the predictions, which is comparable in accuracy to the Lito et al. correlation, developed specifically for high pressure conditions.

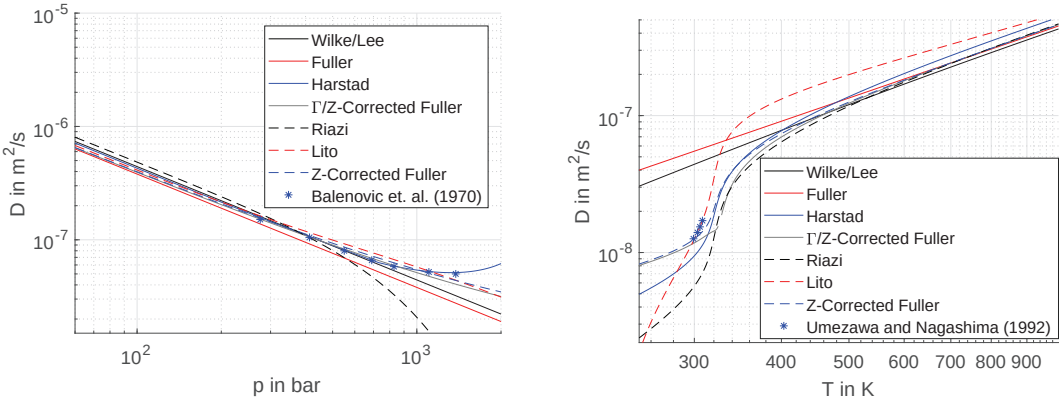

(a) Propane in helium, T = 298 K (b) *n*-heptane in CO_2, $p = 1.05 \cdot 10^7$ Pa

Figure 1. Pressure and temperature dependence of different binary diffusion coefficient models and comparison with experiments.

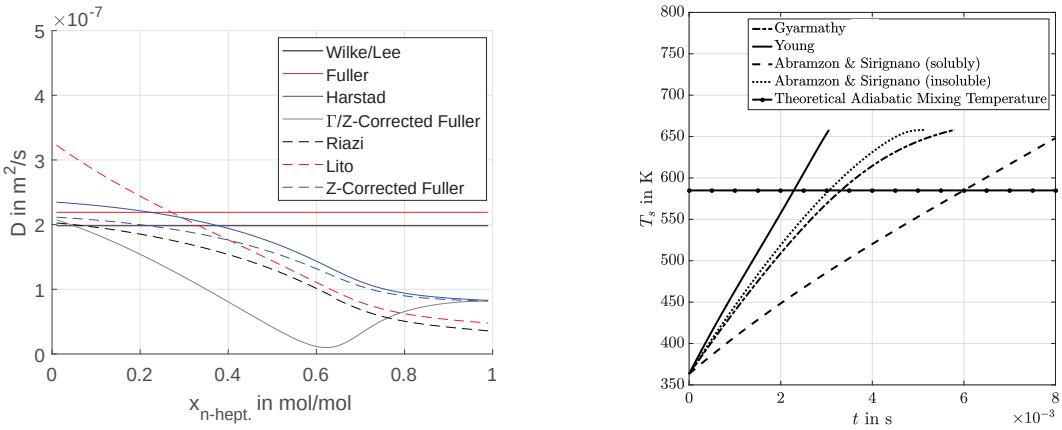

(a) *n*-heptane in CO_2, T = 540 K, $p = 7.38 \cdot 10^6$ Pa (b) *n*-dodecane in N_2, T = 1200 K, $p = 1.06 \cdot 10^7$ Pa

Figure 2. Concentration dependence of different binary diffusion coefficient models and influence on the droplet evaporation rate. Initial droplet temperature: 363 K

Concerning the dependence on mixture composition, $\mathcal{D}_{id}$-models are independent upon the inert gas concentration. All other non-ideal models show a similar trend in the gaseous region (i.e. $x_{n\text{-}hept} < 0.6$), dominated by a strong density dependency. At the critical mixture composition (roughly $x_{n\text{-}hept} = 0.63$), only the Γ/Z-corrected model exhibits a minimum. Large discrepancies in models' predictions are, instead, observed in the liquid-like region ($x_{n\text{-}hept} > 0.63$), where the use of gas-derived corrections is not recommended. Non-ideal liquid diffusion models or empirical correlations should be preferred in the liquid-like region. This uncertainty in the estimation of the binary diffusion coefficient in the liquid droplet hampers the correct estimation of the actual vapor mass fraction ($y_{v,eff}$) at the droplet surface. As explained in the previous section, this leads to an inaccurate estimation of the vapor pressure at the droplet surface and ultimately to an erroneous evaluation of the droplet vaporization rate. The importance of solubility effect is shown in Figure 2(b) for two limiting cases, namely zero and complete solubility of inert gas. As can be seen, the droplet lifetime is almost doubled, when solubility effects are encompassed under the assumption of instantaneous relaxation to a state of binary fluid phase-equilibrium (i.e. $p_{v,s} = y_{v,eq}\, p$), as shown by the simulations with the Abramzon and Sirignano evaporation model. In reality, the effective vapor mass fraction ($y_{v,eff}$) is lower than the equilibrium vapor mass fraction ($y_{v,eq}$) due to the finite inert gas diffusion rate into the liquid droplet. Consequently, the actual evaporation rate will be intermediate among the due limiting cases, considered in Figure 2(b). Given the uncertainty in the modelling of binary diffusion coefficients in compressible liquids, no accurate and reliable estimate of $y_{v,eff}$ can be currently obtained, leading to high uncertainties in the modelling of droplet evaporation at high pressure conditions.

As final remark, we would like to point out that the evaporation process has an important influence on the thermodynamic evolution of the liquid droplet. Indeed, the progression of the droplet temperature is controlled by three energetic contributions according to

$$m_d c_{p,l} \frac{dT}{dt} = -\dot{E}_g - \dot{M}L - \dot{M}h_{vs} \quad (5)$$

where $\dot{E}_g$ represents the energy transfer from the gaseous region, $\dot{M}L$ and $\dot{M}h_{vs}$ the droplet cooling rate due to evaporation. Consequently, for low volatile fluids and high energy transfer rates from the gas phase, the drop gradually heats up to the critical mixing temperature, thus causing the disintegration of the immiscible interface due to the vanishing of surface tension and the transition to the dense-fluid mixing regime. This situation is depicted in Figure 3(a). The opposite occurs for high volatile fluids and low energy transfer from the gas phase, as shown in Figure 3(b). In this case, the drop slowly relaxes towards its equilibrium temperature and the mixture formation is controlled by the evaporation process and not by dense gas mixing.

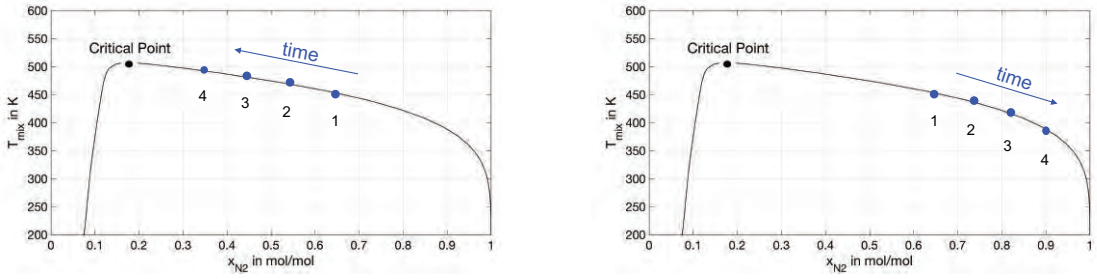

(a) low volatile fluid droplet (b) high volatile fluid droplet

Figure 3. Possible evolution paths for an evaporating droplet: (a) high volatile fluids and (b) low volatile fluids.

References

[1] Givler, S., Abraham, J., Progress in Energy and Combustion Science 22: 1-28 (1996).
[2] Yang, V., Proceedings of the Combustion Institute 28: 925-942 (2000).
[3] Bellan, J., Progress in Energy and Combustion Science 2: 329-366 (2000).
[4] Crua, C., Manin, J., Pickett, L. M., Fuel 208: 535-548 (2017).
[5] Poling, B., Prausnitz, J., and O'Connell J., The Properties of Gases and Liquids, McGraw-Hill, 2001.
[6] Lito, P.F., Magalhães, A.L., Gomes, J.R.B., Silva, C.M., Journal of chromatography. A 1290:1-26 (2013).
[7] Riazi, M.R., Whitson, C.H., Industrial & Engineering Chemistry Research 32(12): 3081-3088 (1993).
[8] Harstad, K., Bellan, J., Industrial & Engineering Chemistry Research 43(2): 645-654 (2004).
[9] Krishna, R., van Baten, J.M., Chemical Engineering Science 153: 174-187 (2016).

Spray Formation and Propagation in Open and Enclosed Reactors

U. Fritsching*[1,2], L. Buss[1], H.F. Meier[3], D. Noriler[4]
[1] Leibniz Institute for Materials Engineering – IWT Bremen, Bremen, Germany
[2] Department of Particle and Process Engineering, University of Bremen, Bremen, Germany
[3] Department of Chemical Engineering, University of Blumenau, Blumenau, Brazil
[4] School of Chemical Engineering, University of Campinas, Campinas, Brazil
*Corresponding author: ufri@iwt.uni-bremen.de

Introduction

Spray processes for particle and powder production typically are performed within an enclosed environment (spray tower or spray chamber). To synthesize metal and metal-oxide particles in nanoscale range, the flame spray pyrolysis (FSP) process can be applied and, in order to design advanced nanomaterials and to improve their properties, as well as to increase the production rate of the process, variations of such process and reactor/atomizer design have been analysed in several studies [1–5]. Most previous investigations on FSP process [6-9] consider an open reactor configuration which leads to a specific gas entrainment that primarily is controlled by the jet strength. However, with this setup, the control of the combustion environment is not so easy [10] and, depending on the requested particle characteristics, it might be hard to achieve them. Enclosing the reactor and applying a oxidizer co-flow gas allows to control the fuel-to-oxidizer ratio [11] in situations where it is required, such as for the synthesis of carbon black [12] and/or production of pure metal-oxide nanoparticles [13–15]. By enclosing the reactor, however, higher flame temperatures (since natural entrainment, and, therefore, its quenching effect is suppressed) and larger nanoparticles (since the particle coagulation and sintering are temperature-dependent) are observed [16]. In the conventional FSP process, a liquid precursor is dissolved in an organic fuel which is atomized into a spray of fine droplets. These droplets evaporate, and the vapor is instantaneously ignited due to the energy provided by a support flame. The fuel combustion produces enough energy to decompose and oxidize the precursor, resulting in a supersaturated environment of metallic oxide vapor which induces the particle nucleation and growth [17]. The spray formation and its propagation are affected by the shape and size of the enclosure as well as the amount of co-flowing gas, and, therefore, these phenomena in the enclosing spray chamber are to be controlled by flow control measures as, for instance, the superficial secondary gas flow.

In this contribution, spray processes for powder production – e.g. FSP process for nano-sized particle synthesis – is analyzed numerically by computational fluid dynamics (CFD) simulations. The role of the entrainment flow and recirculation areas in the enclosure is highlighted. In this sense, the influence of geometrical setups (open and enclosed reactor) at different operating conditions on the flame temperature and spray behavior as well as on the reactor temperature and temperature-residence-time distribution of the gas and the particles are investigated. Based on the natural gas entrainment into the spray flame, the appropriate amount of co-flowing gas satisfying the entrainment requirement of the spray is derived. Supplying this amount of co-flowing gas to the enclosed reactor setup results in a quite similar flame behavior as found for the open reactor. On the other hand, reducing the co-flow gas rate, strong vortex and recirculation zones are formed, which are typically observed in confined jets with reduced co-flow [18], and the temperature increases considerably, resulting in larger nanoparticle sizes [19]. The numerical results are analyzed and compared to the findings of previous studies.

Reactor Geometry and Numerical Domain

Figure 1 depicts a sketch of the two reactor setups used in this work. Figure 1a presents the open configuration, which consists of a twin-fluid atomizer surrounded by a support flame that is positioned in the center of a metallic plate. In the enclosed configuration, Figure 1b, the metallic plate is smaller and is surrounded by a porous plate, through the which the co-flowing gas is fed, positioned on the bottom of enclosure tube. The enclosure consists of a quartz tube with inner diameter of 0.1 m, height of 0.5 m and thickness of 0.003 m. The atomizer nozzle used here is described in detail by Mädler et al. [6]. The computational simulations are performed using a bi-dimensional (2D) axisymmetric approach, Figure 1c, in a numerical grid of ~175,000 hexahedral cells, considering a cylindrical domain with 0.1 m of diameter and 0.5 m of height. The applied computational mesh is refined in the region closest to the atomizer nozzle, where large gradients of velocity, temperature, and chemical species are found.

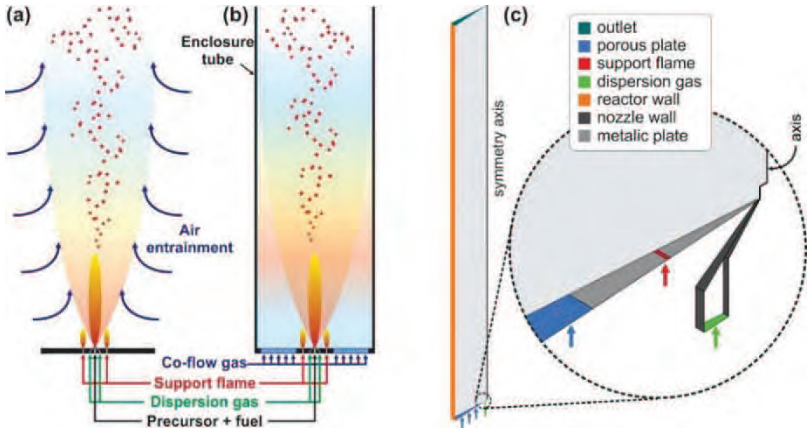

Figure 1. Sketch of FSP reactor in (a) open setup and (b) enclosed configuration; (c) 2D axisymmetric numerical domain.

Operating and Boundary Conditions

In this study, the boundary conditions (Table 1) are adjusted as adiabatic and impermeable wall for the nozzle and metallic plate walls; fixed mass flow for oxidant, support flame inlet and co-flow gas; and pressure boundary (fixed static pressure and zero gradients for the remaining variables) for the top and side limits (open reactor). Regarding the simulation setup applied to the enclosed configuration, heat transfer through the reactor walls must be considered since overestimation in the temperature distribution is expected when the reactor walls are adjusted to adiabatic condition, as has been demonstrated in the previous investigation [20]. The liquid phase consists of a precursor solution of zirconium *n*-propoxide (70 wt-% in *n*-propanol) and ethanol, with a total zirconium concentration of 0.5 mol/L. This solution is feed with a constant flow rate of 5 mL/min to the reactor and is atomized by 5 L/min dispersion oxygen, which gives a gas-to-liquid mass ratio (GLMR) of 1.7. The nozzle gap is adjusted to maintain a pressure drop of 1.5 x 10^5 Pa. The reactor operates either in open or enclosed condition, both at atmospheric pressure. In the enclosed configuration, air is supplied as co-flowing gas. From the open setup, the entrainment mass flow rate of gas is estimated. Several simulations (varying the gas co-flow rate) with the enclosed configuration are performed. These co-flow rates are 400 L/min (derived from estimations of entrainment gas with the open setup), 100 and 40 L/min. The liquid phase is already injected in the domain as spray droplets. The initial spray droplet size distribution is correlated by means of a Rosin-Rammler-Sperling-Bennet (RRSB) function to obtain the relevant parameters for the model setup and a stochastic Discrete Random Walk (DRW) model is applied to predict the turbulent droplet dispersion [21]. Proper droplet size distributions are obtained from previous studies [11, 22, 23].

Table 1. Boundary conditions assumed for numerical simulations.

Boundary name	Type	Value	Chemical composition
Dispersion gas	Mass-flow-inlet	1.19 x 10^{-4} kg/s (5 L/min)	100 wt-% O_2
Metallic plate	Wall	No-slip / Adiabatic	–
Nozzle wall	Wall	No-slip / Adiabatic	–
Outlet	Pressure-outlet	0 Pa	77 wt-% N_2 + 23 wt-% O_2
Support flame	Mass-flow-inlet	9.41 x 10^{-5} kg/s (4.7 L/min)	19 wt-% CH_4 + 81 wt-% O_2
Porous plate [a]	Wall	No-slip / Adiabatic	–
		8.50 x 10^{-3} kg/s (400 L/min)	
Porous plate [b]	Mass-flow-inlet	2.13 x 10^{-3} kg/s (100 L/min)	77 wt-% N_2 + 23 wt-% O_2
		8.50 x 10^{-4} kg/s (40 L/min)	
Reactor wall [a]	Pressure outlet	0 Pa	77 wt-% N_2 + 23 wt-% O_2
Reactor wall [b]	Wall	No-slip / Adiabatic	–

[a] For open reactor setup.

[b] For enclosed reactor setup.

Results and Discussion

Figure 2 presents CFD results concerning the gas velocity fields (a, c-e), gas entrainment (b) and gas recirculation (f) in a spray reactor. The mass flow of gas entrainment from the ambient – which is dragged into the spray region – increases with increasing the axial distance from the atomizer. Ricou and Spalding [24] proposed a linear correlation for the total mass flow rate of gas entrainment, $\dot{m}$, for a diffusion gas flame. Analysing the open setup (Figure 2a), the entrainment ratio at several heights above the burner, HAB, can be estimated (Figure 2b). By supplying sufficient amount of co-flow gas that satisfies the entrainment requirement of the spray – in this case ~400 L/min (Figure 2c) – a similar spray flow behavior and morphology as found in the open setup and negligible

recirculation are observed. In contrast, decreasing the co-flow rate (Figure 2d-e) strong vortex and recirculation zones are formed, which is typically observed in confined jets with reduced co-flow [18].

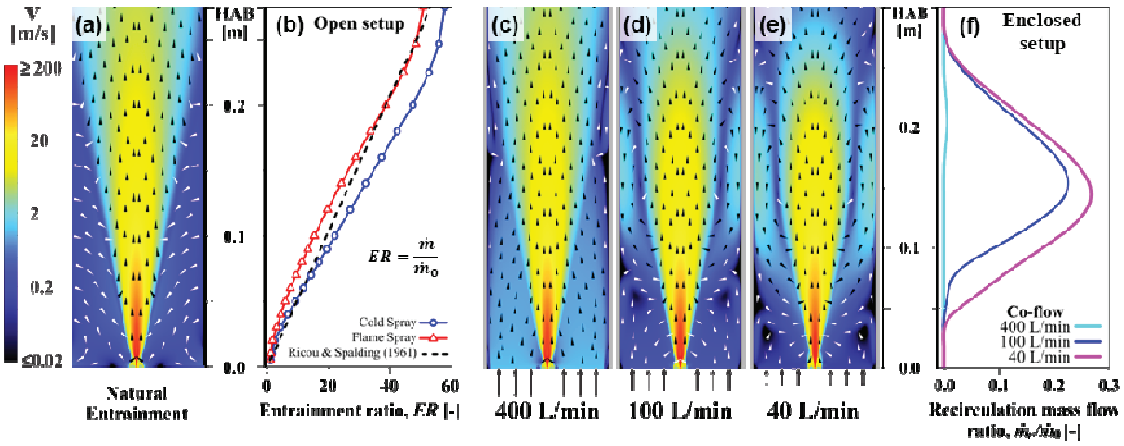

Figure 2. Gas velocity fields of open (a) and enclosed FSP reactor (c-e); analysis of entrainment ratio (b) at several heights above the burner (HAB) in an open FSP reactor and recirculation mass flow ratio (f) in an enclosed FSP reactor.

Figure 3 shows the predicted temperature distributions, the particle-residence-time, PRT as function of temperature, and primary particle diameter as function of HAB for the different investigated cases. In the open reactor and enclosed setup with 400 L/min co-flowing gas (Figure 3a and b, respectively), the temperature fields are quite similar, confirming the appropriate co-flowing gas is supplied. Reducing the co-flow also increases the reactor temperature fields, since the amount of quenching gas supplied to the reactor is lower and the recirculation of hot gas is stronger. As is shown in Figure 3b-d, the lower co-flow rates are, the stronger the vortex formation and recirculation zones become, leading, in turn, to higher temperature in the downstream of the reactor. The gas recirculation also increases the PRT in the flame/hot regions (Figure 3e) which results in larger particle formation (Figure 3f) with lower co-flowing gas rates. For the open configuration, the PRT has a maximum of ~0.10 s at just 450 K while for the enclosed setup with the lower co-flow rate, the maximal PRT is ~0.35 s (at 600 K). For temperature > 600 K, the PRT of the open and enclosed reactor with 400 L/min co-flowing gas present quite similar results, again, corroborating the appropriate co-flow gas is provided. As nanoparticle coagulation and sintering are determined by the temperature history, particles with similar size distribution are produced by both open and enclosed with 400 L/min configurations, since similar PRT in the same temperature range are found. Decreasing the gas co-flow rate extends the PRT in the high temperature zones. For the case with 40 L/min co-flowing gas, at 1500 K, the PRT is ~0.16 s and reaches values smaller than 0.005 s in the regions with temperatures of ~2250 K only. As observed in Figure 3f, the PRT in the high temperature zones impacts directly the powder size distribution. The longer the PRT in high-temperature regions, the larger is the size of produced particles.

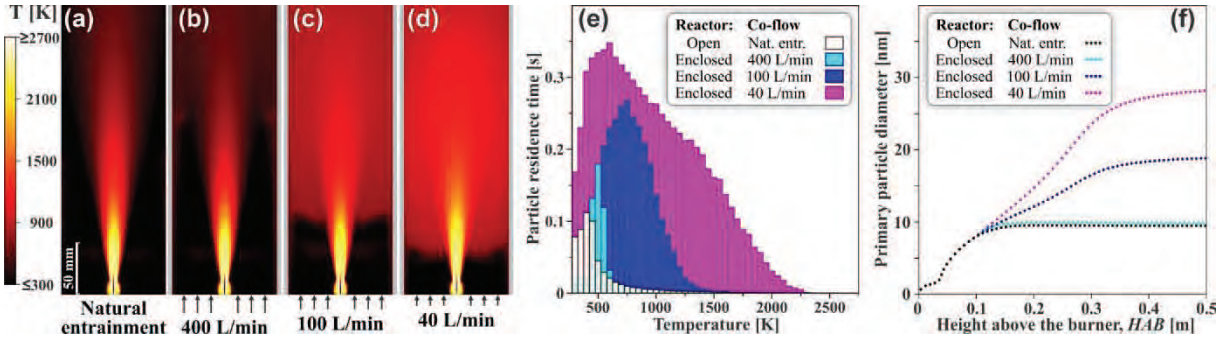

Figure 3. Simulated temperature fields of open (a) and enclosed FSP reactor (b-c); particle-residence-time, TRT, (e) and primary particle diameter (f) for the open and enclosed setups and different co-flow rates.

Nomenclature

$\dot{m}_0$	initial mass flow rate [kg s^{-1}]
$\dot{m}_r$	recirculation mass flow rate [kg s^{-1}]
$\dot{m}$	mass flow rate [kg s^{-1}]
CFD	computational fluid dynamics
DRW	Discrete Random Walk model
ER	entrainment ratio

FSP flame spray pyrolysis
GLMR gas-to-liquid mass ratio
HAB height above the burner [m]
PRT particle-residence-time [s]
RRSB Rosin-Rammler-Sperling-Bennet function

Acknowledgments
This contribution has received funding from the German Research Foundation – DFG (Project ID: FR912/33) and Coordination for the Improvement of Higher Education Personnel – CAPES (Process ID: BEX 12369/12-8) and is part of the framework program of the Brazilian-German Collaborative Research Initiative on Manufacturing Technology – BRAGECRIM (Project ID: 20/2012). Additional acknowledgement is also directed to The São Paulo Research Foundation – FAPESP, in Brazil (Project ID: 2017/04045-0).
The results reported here have been presented at the DIPSI Workshop 2018 in Bergamo and parts were also presented at ICLASS 2018 in Chicago [11].

References
[1] Fritsching, U., Spray Systems, in Multiphase Flow Handbook, CRC Press, Boca Raton, 2006.
[2] Fritsching, U., Uhlenwinkel, V., “Hybrid Gas Atomization Powder Production,” in *Powder Metallurgy*, In Tech, 2012.
[3] Lagutkin, S., Achelis, L., Sheikhaliev, S., Uhlenwinkel, V., Srivastava, V., *Materials Science and Engineering A,* 383: 1-6 (2004).
[4] Meierhofer, F., Hodapp, M. J., Achelis, L., Buss, L., Noriler, D., Meier, H. F., Fritsching, U., *Materials Science and Engineering Technology,* 45: 765-778 (2014).
[5] Achelis, L., Meierhofer, F., Hodapp, M. J., Buss, L., Noriler, D., Meier, H. F., Fritsching, U., *Proceedings of the ASME 2014 - 4th Joint US-European Fluids Engineering Division Summer Meeting,* 3-7 August 2014.
[6] Mädler, L., Kammler, H. K., Mueller, R., Pratsinis, S. E., *Journal of Aerosol Science,* 33: 369-389 (2002).
[7] Mädler, L., *KONA Powder and Particle Journal*, 22: 107-120 (2004).
[8] Mädler, L., Roessler, A., Pratsinis, S. E., Sahm, T., Gurlo, A., Barsan, N., Weimar, U., *Sensors and Actuators,* 114: 283-295 (2006).
[9] Gröhn, A. J., Pratsinis, S. E., Wegner, K., *Chemical Engineering Journal,* 191: 491-502 (2012).
[10] Waser, O., Groehn, A. J., Eggersdorfer, M. L., Pratsinis, S. E., *Aerosol Science and Technology,* 48: 1195-1206 (2014).
[11] Buss, L., Bianchi Neto, P., Meier, H. F., Fritsching, U., Noriler, D., *ICLASS 2018 - 14th Triennial International Conference on Liquid Atomization and Spray Systems,* 22-26 July 2018.
[12] Waser, O., Büchel, R., Hintennach, A., Novák, P., Pratsinis, S. E., *Journal ofAerosol Science,* 42: 657-667 (2011).
[13] Athanassiou, E. K., Grass, R. N., Stark, W. J., *Nanotechnology,* 17: 1668-1673 (2006).
[14] Waser, O., Brenner, O., Groehn, A. J., Pratsinis, S. E., *Chemical and Process Engineering,* 38: 51-66 (2017).
[15] Buss, L., Meierhofer, F., Noriler, D., Meier, H. F., Fritsching, U., *ILASS - Europe 2016, 27th Annual Conference on Liquid Atomization and Spray Systems,* 4-7 September 2016.
[17] Teoh, W. Y., Amal, R., Mädler, L., *Nanoscale,* 2: 1324-1347 (2010).
[18] Curtet, R., *Combustion and Flame,* 2: 383-411 (1958).
[19] Waser, O., Hess, M., Güntner, A., Novák, P., Pratsinis, S. E., *Journal of Power Sources,* 241: 415-422 (2013).
[20] Meierhofer, F., Buss, L., Noriler, D., Meier, H. F., Fritsching, U., *ICMF 2016 - 9th International Conference on Multiphase Flow,* 22-27 May 2016.
[21] Gosman, A. D., Ioannides, E., *Journal of Energy,* 7: 482-490 (1983).
[22] Noriler, D., Rosebrock, C. D., Mädler, L., Meier, H. F., Fritsching, U. *Atomization and Sprays,* 24: 495-524 (2014).
[23] Bianchi Neto, P., Buss, L., Meierhofer, F., Meier, H. F., Fritsching, U., Noriler, D., *Chemical Engineering and Processing,* 129: 17-27 (2018).
[24] Ricou, F. P., Spalding, D. B., *Journal of Fluid Mechanics,* 11: 21-32 (1961).

Spray measurements in SCR systems development

Ł.J. Kapusta
Warsaw University of Technology, Faculty of Power and Aeronautical Engineering, Institute of Heat Engineering, Poland
Lukasz.Kapusta@itc.pw.edu.pl

Introduction

Recently the importance of spray measurements in automotive urea-SCR (Selective Catalytic Reduction) systems development has strongly increased. Since the in-line under floor exhaust systems have been replaced with close-coupled to the engine designs, the distance available for UWS evaporation and urea decomposition has dramatically decreased. Close-coupled to the engine SCRs are preferred due to higher exhaust gas temperature and NOx reduction [1]. Near-engine location results in decreased distance for water evaporation and urea decomposition. Thus, spray properties need to be properly adjusted to specific SCR system design – this includes injector selection and its location optimization. One needs to be aware that properly adjusted spray alone is not sufficient to assure water evaporation and urea decomposition before the inlet to the catalyst in typical close-coupled SCR design. Therefore, the additional static mixing elements are needed to enhance mixing and provide proper NH_3 distribution at inlet to the catalyst. Majority of work related to static mixer designs and SCR design optimization is done using CFD (Computational Fluid Dynamics) simulations, where full SCR system designs are considered [2]–[5]. These simulations include both spray formation in the gaseous media and spray-wall interaction. Spray modelling in turn requires much data on the spray properties which needs to be determined experimentally. The simplified early-stage development process of SCR systems including experimental spray measurements is shown in Fig. 1.

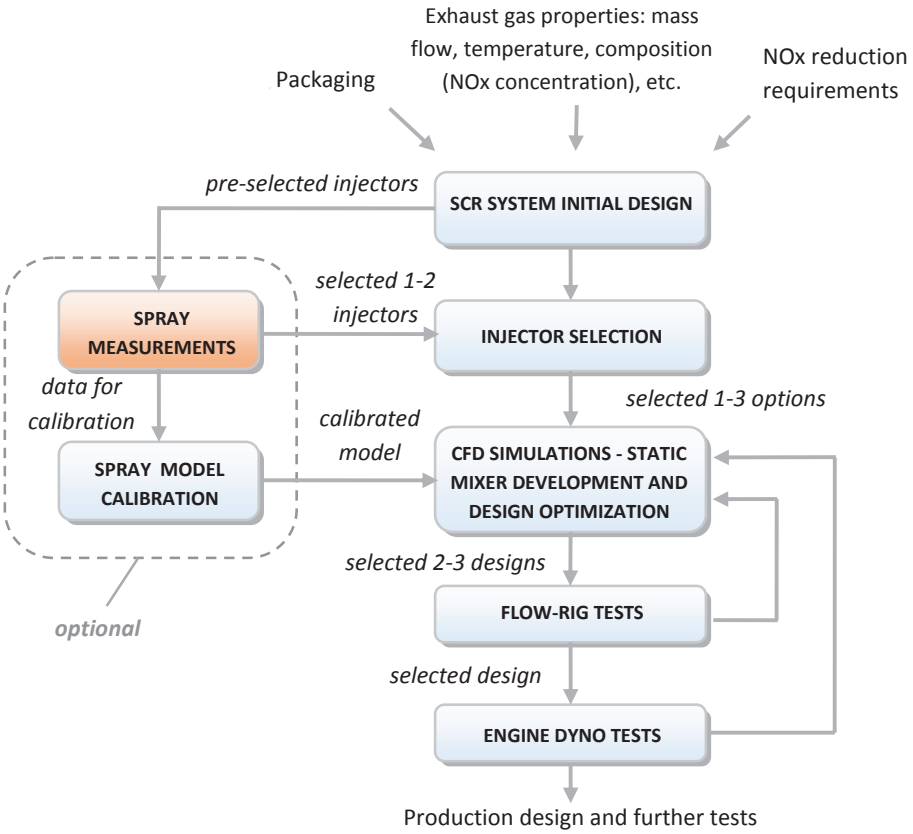

Figure 1. Simplified early-stage development process of SCR systems

As shown in Fig. 1 the spray measurements take place at very initial stage of SCR development in parallel to main activities. This comes out from the fact that the SCR system development can be done basing only on data provided by injector manufacturer, and thus spray measurements can be regarded as optional activities. However, simplified approach (excluding spray measurements) has strong disadvantage since data provided by manufacturer is usually limited while the injector characterization can provide additional data such as droplet spatial distribution which allows to properly select injector to specific system and calibrate spray models. Spray measurements included in the development process allow to directly compare injectors from different manufacturers assuring that the compared data is not affected by different experimental setups.
When additional spray measurements are included, the main activities in SCR system development remain the same, however the input data is different. In that case, directly after creating initial SCR system design which is done basing mainly on vehicle and engine features as well as target market needs (emissions limits), the initially preselected injectors are tested experimentally. Initial injector preselection is done using injector manufacturer data and CAD (computer aided design) simulations, i.e. fitting spray cones into exhaust system. Based on spray measurements the injector (max. 2 injectors – second as the alternative option) is selected to be used in the developed SCR systems. Moreover, the experimental data on spray properties is used to calibrate numerical models, which are then used to develop static mixers and optimize SCR design including injector location in the system. In this study the spray measurement procedure is shown, and techniques used to determine required spray parameters are discussed.

Material and methods

The spray parameters needed to select injector and calibrate spray models include spray angles (plume directions, plume angle and visualisation angle), spray tip penetration evolution and droplet size distribution. High speed imaging with global illumination was used for global spray parameters determination (visualisation angle, single plume angle, jet directions and spray tip penetration). As for the droplet size distribution, sprays for SCR applications due to relatively large droplets (typically around 100μm) and low number density offer huge potential in terms of applied techniques. In this study shadowgraphy with long distance microscope was used to determine droplet size distribution. Due to frequency of the laser limited to 10 Hz only one image per injection was taken, and the droplet size distribution was composed for 100 consecutive injections.
Due to limited field of view in shadowgraphy setup, additionally LIF/Mie approach (Laser Induced Fluorescence and Mie scattering) was used to determine qualitative droplet size distribution across the whole spray cloud. The LIF/Mie method was coupled with structured illumination to minimize noise signals caused by background reflections and multiple scattering. The setup for LIF/Mie measurements with structured illumination is shown in Fig. 2.

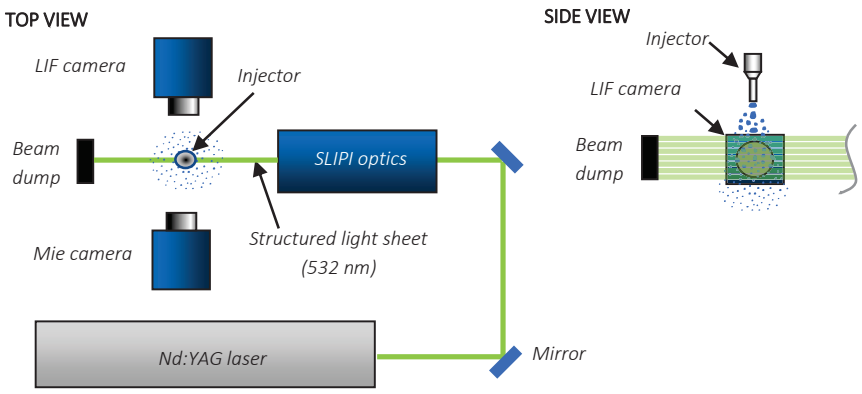

Figure 2. Schematic diagram of complete experimental setup [6]

Results and Discussion

The acquired data was used in both development stages, injector selection and spray model calibration for full SCR system CFD simulations. Injector selection was done basing on shadowgraphy results. The selection was done by both qualitative and quantitative comparison of the results. The raw shadowgraphy images were compared qualitatively in terms of spatial dispersion of the droplets (Fig. 3). Additionally, the droplet distribution was compared quantitively (Fig. 4).

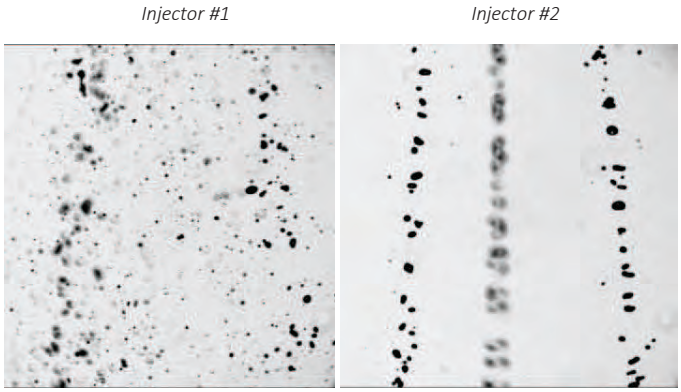

Figure 3. Shadowgraphy images of two tested injectors

The qualitative image comparison indicated that the droplets generated by injector #1 are more evenly distributed over the whole spray cloud while those emerged from injector #2 tend to travel along nozzle axes. The qualitative overview suggested also that injector #1 produces more medium and small droplets than injector #2. This was confirmed by quantitative comparison of droplet size distribution (Fig. 4). Moreover, it can be observed that injector #2 produced very large droplets (>200 μm), which were supposed to agglomerate either on inlet to the catalyst or exhaust system walls. Therefore, injector #1 was selected to be used in developed SCR system.

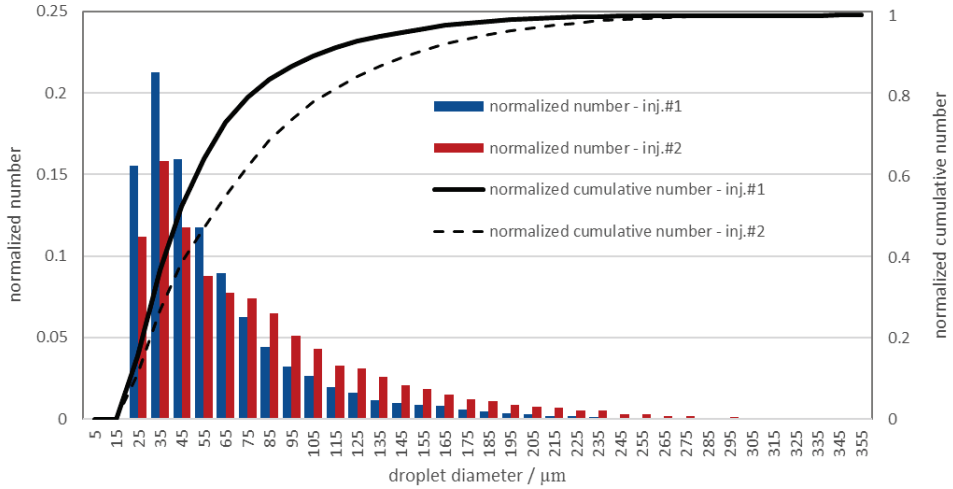

Figure 4. Droplet size distribution for two tested injectors

The experimental data obtained for selected injector was used for spray model calibration similarly as shown in [7]. Droplet size distribution shown in Fig. 4 was used as one of the input parameters for spray model. Spray angles (single plume angle and plumes directions) as well as initial jet velocity (determined by high speed imaging) were also used as input parameters, while the spray tip penetration evolution was used as target parameter for model matching.

Additionally, the selected injector was characterized using simultaneous LIF and Mie scattering visualisation according to setup presented in Fig. 2. These two signals were used to determine qualitative droplet size distribution across the whole spray cloud by means of LIF/Mie ratio. LIF and Mie signals alone can be used for mass distribution determination [8], however LIF/Mie ratio is more useful parameter for spray model performance verification in terms of droplet size distribution across the spray cloud as it was done in this study. The LIF/Mie ratio was used only for qualitative model verification as no size calibration was done. The droplet sizes as presented in Fig. 4 (above 20 μm) according to [9] provide close to linear correlation between Mie signal and droplet size when 3.8 deg solid angle is considered. Thus LIF/Mie ratio could be used in this setup as qualitative SMD (Sauter mean diameter) distribution indicator. LIF, Mie and LIF/Mie ratio results for selected injector are shown in Fig. 5.

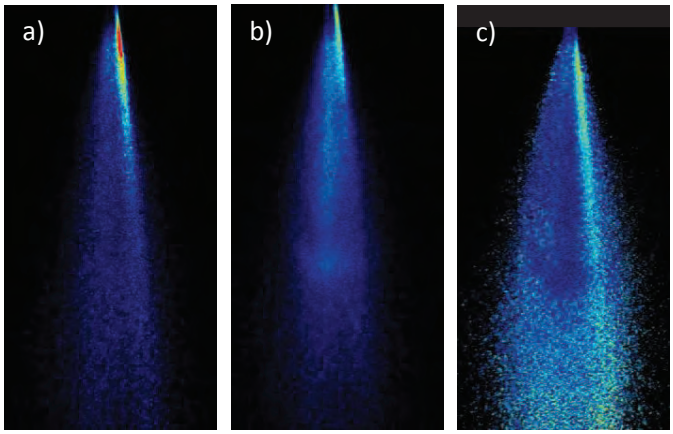

Figure 5. a) LIF, b) Mie, c) LIF/Mie ratio; (adopted from [6])

The spray model was further calibrated in terms of spatial droplet distribution and then used for static mixer development and SCR system design optimization (including injector position optimization).

Taking into account benefits related to direct comparison of sprays generated by different injectors from different manufactures using the same diagnostic setups (as shown in Fig. 3) and additional data available for spray model verification such as LIF/Mie ratio (shown in Fig. 5c), it can be concluded that spray measurement has strong positive impact on SCR systems development.

Nomenclature

CAD	computer aided design
CFD	computational fluid dynamics
LIF	laser induced fluorescence
SCR	selective catalytic reduction
SMD	Sauter mean diameter

Acknowledgments

The study was supported by Polish Ministry of Science through funds for statutory activities in 2017.

References

[1] H. Kojima, M. Fischer, H. Haga, N. Ohya, K. Nishi, T. Mito, and N. Fukushi, Next Generation All in One Close-Coupled Urea-SCR System, in SAE Technical Paper, 2015.
[2] P. Tai, Y. Shu, and M. Romzek, Enhancement of Flow Distribution and Pressure Drop Performance of SCR System for Commercial Vehicles, SAE Tech. Pap. 2013-01-1586, pp. 2–10, 2013.
[3] P. Wetzel, J. E. Mccarthy, and G. Griffin, Diesel Exhaust Aftertreatment System Packaging and Flow Optimization on a Heavy-Duty Diesel Engine Powered Vehicle, vol. 3, no. 1, pp. 143–155, 2011.
[4] A. Capetillo and F. Ibarra, Multiphase injector modelling for automotive SCR systems : A full factorial design of experiment and optimization, Comput. Math. with Appl., vol. 74, no. 1, pp. 188–200, 2017.
[5] R. Rafał, P. Jaworski, Ł. J. Kapusta, and A. Teodorczyk, The influence of the injection frequency on the urea selective catalytic reduction systems performance, Combust. Engines, vol. 170, no. 3, pp. 73–77, 2017.
[6] Ł. J. Kapusta, LIF/Mie Droplet Sizing of Water Sprays from SCR System Injector Using Structured Illumination, in Proceedings of ILASS2017 - 28th European Conference on Liquid Atomization and Spray Systems, 2017, pp. 580–587.
[7] J. Bachanek, R. Rogóż, Ł. J. Kapusta, and A. Teodorczyk, CFD spray model calibration for urea water solution injection in SCR systems, in Proceedings of the 8th European Combustion Meeting, 2017, pp. 996–1000.
[8] L. Postrioti, G. Brizi, C. Ungaro, M. Mosser, and F. Bianconi, A methodology to investigate the behaviour of urea-water sprays in high temperature air flow for SCR de-NOx applications, Fuel, vol. 150, no. x, pp. 548–557, 2015.
[9] G. Charalampous and Y. Hardalupas, Numerical evaluation of droplet sizing based on the ratio of fluorescent and scattered light intensities (LIF/Mie technique)., Appl. Opt., vol. 50, no. 9, pp. 1197–1209, 2011.

Nanofluid sprays for cooling applications

M. Malý[1], A.S. Moita*[2], J. Jedelsky[2], A.P.C. Ribeiro[3], A.L.N. Moreira[2]
[1] Faculty of Mechanical Engineering, Brno University of Technology, Brno, Czech Republic.
[2] IN+ - Center for Innovation, Technology and Policy Research, Instituto Superior Técnico, Universidade de Lisboa, Lisboa, Portugal.
[3] Centro de Química Estrutural, Instituto Superior Técnico, Universidade de Lisboa, Lisboa, Portugal.
*Corresponding author: anamoita@tecnico.ulisboa.pt

Introduction

Spray cooling is among the most popular liquid cooling strategies, given the high heat transfer coefficients that can be delivered [1]. However, increasingly demanding heat loads in applications such as electronics cooling have pushed researchers to further enhance the heat transfer processes, by altering the surfaces and/or the fluids e.g. [2-4]. Fluids with nanoparticles are pointed to have great potential to improve heat transfer processes, given their potentially higher thermal properties. However, increasing the concentration of the nanoparticles may alter significantly other physical properties such as the viscosity, which affect the fluid flow and may eventually reverse any advantage of adding the nanoparticles. Furthermore, while most authors have focused simply on the effect of the nanoparticles on the bulk properties of the fluid, studies on the wettability and on the interaction effects of the particles on the surfaces and on droplet-droplet interactions is scarcely reported. The actual effects of adding nanoparticles in the fluid flow characteristics and, particularly in the mechanisms of atomization, have also been drawn to a secondary plane.

In this context, the present work focuses on the effect of nanofluid preparation, particularly on the effect of the nanoparticles concentration, on the local physical properties of the resulting fluid and their consequent effect on the atomization characteristics (droplet size, velocity distribution, spray angle, etc) using nanofluids. The results are discussed focusing on how the spray characteristics affect the use of the resulting spray for cooling purposes. Nanoparticles of alumina (Al_2O_3) and Zinc Oxide (ZnO) are mixed in water-based solutions, for concentrations varying between 0.5% and 2% wt for alumina and between 0.01% and 0.1% wt for the zinc oxide particles. CuO (0.1% wt) and $FeCl_2.4H_2O$ (0.1% wt) were also used to infer on the effect of the nature (material) of the particles in the physico-chemical properties of the resulting solutions. High-speed imaging is combined with Phase Doppler Anemometry and Laser Scanning Confocal Microscopy to fully characterize the nanofluids properties and the spray characteristics.

The results show that liquid viscosity is an important parameter in predetermining the spray characteristics of the nanofluids, as it affects the primary breakup. However, only a minor increase is observed in the nanofluids viscosity, mainly for higher concentrations of alumina. This variation in the viscosity was observed to slightly affect droplet size distribution and to cause a small decrease in the cone angle of the spray. Hence, for the range of nanoparticles nature and concentration covered here, there is a positive balance in the use of the nanoparticles, increasing the thermal properties without a significant deterioration of other fluid properties such as viscosity, or spray dynamics.

Material and methods

The sprays are generated in a small pressure-swirl type atomizer, with a square cross-section 0.6 x 0.6 mm, which produces a wide cone spray. The discharge orifice is 0.42 mm.

The liquid is supplied from a small (3 l) pressure vessel, pressurized by air at 87 PSI. At this pressure (approx. 5 bar overpressure), the mass flow rate through the atomizer is approx. 7 kgh^{-1}.

The nanofluids are prepared following a two-step process. The particles are mixed with DI water, in concentrations ranging between 0.01 and 2% weight percentages and placed in an ultrasonic bath for 1 h. The specific nanofluid concentrations used in the present work are identified in Table 1. Citric acid was added as a surfactant, to maintain the particles dispersed and the nanofluids stable during the experiments. The nanoparticles are mainly composed by metals and oxide metals to enhance the thermal properties of the resulting nanofluids, for cooling applications.

The wettability of the nanofluids on the contact surfaces was quantified by equilibrium contact angles, using an optical tensiometer (THETA from Attension). Uncertainty of the contact angle measurements was at most of the order of ±5º.

The measurements were performed following the sessile droplet method, as detailed, for instance in [5]. In addition, a Laser Scanning Confocal Microscope (Leica SP8) was used to perform Laser Scanning Confocal Fluorescence

Microscopy – LSCFM - and 3D reconstruction, to visualize the micro-layer in the very vicinity of the triple contact line and characterize wettability within improved spatial resolution, as in [6].
As for the properties of the nanofluids, density was evaluated from the solutions concentration, by mass conservation principles and was very close to that of the water (DI) for all the samples tested (ρ = 998kgm^{-3}). The viscosity was measured with an ATS RheoSystems (a division of CANNON® Instruments, Co) under controlled temperature conditions, with an accuracy of ±5%. Finally, the surface tension was measured under controlled temperature conditions (20 ± 2ºC) with an optical tensiometer THETA (Attention), using the pendant drop method. The value taken for the surface tension of each solution was averaged from 15 measurements, with a maximum standard deviation of the mean of 0.04 mNm^{-1}.

Table 1. Composition and main physico-chemical properties of the nanofluids used in the present study.

Sample number	Weight percentage (wt %)					Size of the particles [nm]	μ_l	σ_{lv}
	Surfactant		Oxide		Deionized water		gm^{-1}s^{-1}	mNm^{-1}
1	Oleic acid	0.15	---		99.85 (pure)		1.02	74.2
2	Citric acid	0.15	Al_2O_3	2	97.85 (pure)	80	1.12	72.8
3	Citric acid	0.15	Al_2O_3	0.5	99.35 (pure)	80	1.05	73.4
4	Citric acid	0.15	ZnO	0.5	99.35 (pure)	80	1.02	74.3
5	Citric acid	0.15	ZnO	0.01	99.84 (pure)	80	1.28	73.0
6	Citric acid	0.15	CuO	0.1	99.75 (pure)	50	1.05	72.0
7	Citric acid	0.15	$FeCl_2$. $4H_2O$	0.1	99.75 (pure)	≥ 100	1.04	71.6

The spray was characterized combining high-speed imaging with phase Doppler anemometry measurements.
A Phantom v4.2 high-speed camera was used to obtain spray images, which were afterwards post-processed to analyse qualitatively the morphology of the sprays and to evaluate several additional parameters such as the spray cone angle. Images were taken at 15kHz, with a resolution of 192x192px^2.
Phase Doppler measurements were performed with a two-component system from Dantec, to describe size and velocity distributions in the resulting nanofluid sprays.
A measurement grid was used which considers a radial system, as defined in Figure 1, where r = 0mm corresponds to the center of the spray cone and z=0mm is at the exit of the spray nozzle. Measurements were performed for -20mm < r < 20mm, -20mm < y < 20mm and z = 10mm and Z = 20mm, in 2mm steps for each direction.
Detailed description of the experimental arrangement and of the measurement procedures is provided in [3].

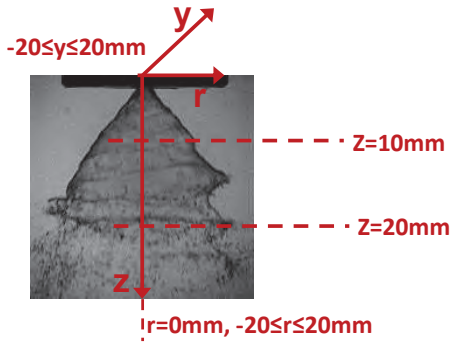

Figure 1. System of coordinates used in the measurements with the phase Doppler instrument.

Results and Discussion
Table 1 does not evidence significant differences between the surface tension values measured for the different nanofluid solutions. The viscosity, on the other hand, is observed to increase mildly, even for the low nanoparticle

concentrations used here. It is worth mentioning that the properties of the solutions were measured before and after atomization, to check on the stability of the solutions and on the possible effect of particles trapping in the atomizer in the liquid feeding system, which could alter the real concentration of the solutions and, consequently their physico-chemical properties. Any significant changes were observed in the measurements performed before and after the atomization. This slight increase in the bulk viscosity of the nanofluids was therefore further investigated to infer how it could be affecting the spray atomization processes. In line with this, the morphology of the various nanofluid sprays was observed from high-speed imaging. Image analysis and post-processing reveals no significant different between the morphology of the various nanofluid sprays. Also, the liquid sheet breakup length, evaluated based on these images was observed to occur at about 5–7 mm below the exit orifice, independently from the nanofluid used. Based on these observations, a more careful analysis was performed at two main axial distances from the nozzle, namely at z=10mm and z=20mm. While at the distance closer to the exit orifice the measurements are performed just after the primary breakup, which is definitly more affected by the liquid viscosity, the measurements performed at z=20mm may be less affected by viscosity, being therefore expected to be dominated by surface tension effects. Such relative dominance of viscous vs surface tension effects can be discussed, observing the spray cone angle and the integral Sauter mean diameter ID_{32}, as defined by [7], as a function of the dynamic viscosity, which in turn increases with the concentration of the nanoparticles, as obseved in Table 1.

Hence, the spray cone angle measurements performed at z=10mm, as depicted in Figure 2a show a small decline with increasing viscosity, evidencing a dominant effect of the viscous forces. This maybe so, since larger viscosity tends to promote dissipation inside the swirl chamber of the atomizer, thus lowering the flow velocities and consequently, decreasing the spray cone angle. However, as the measurements are performed farther away from the primary breakup region, the viscosity effect becomes negligleable, thus suggesting the dominance of the surface tension, which is hardly affected by the presence of the nanoparticles (Figure 2b).

These trends are supported by measurements of ID_{32}, also represented as a function of the nanofluids viscosity. Again, the effect of increasing the viscosity of the nanofluids, caused by the addition of the nanoparticles leads to a mild increase in the ID_{32} (Figure 3a) at the primary break-up region (z =1 0mm), which is hardly noticed at z = 20mm (Figure 3b).

The ratio between the liquid phase Weber and Reynolds numbers at z = 20mm, roughly varies between 0.35 and 0.5, depending on the nanofluid used, thus reinforcing the trend that the increasing concentration of the nanofluids strongly affects the region of the primary break-up, which is governed by the increased viscous forces, but has only a minor effect as the spray becomes fully developed.

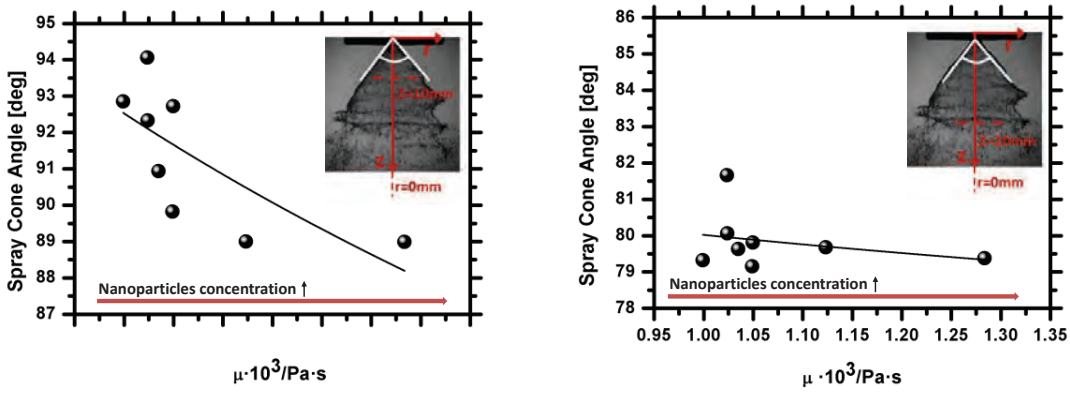

a) b)

Figure 2. Effect of the nanoparticles concentration (represented in the nanofluids viscosity) on the spray cone angle at a) z = 10 mm. b) *z* = 20 mm.

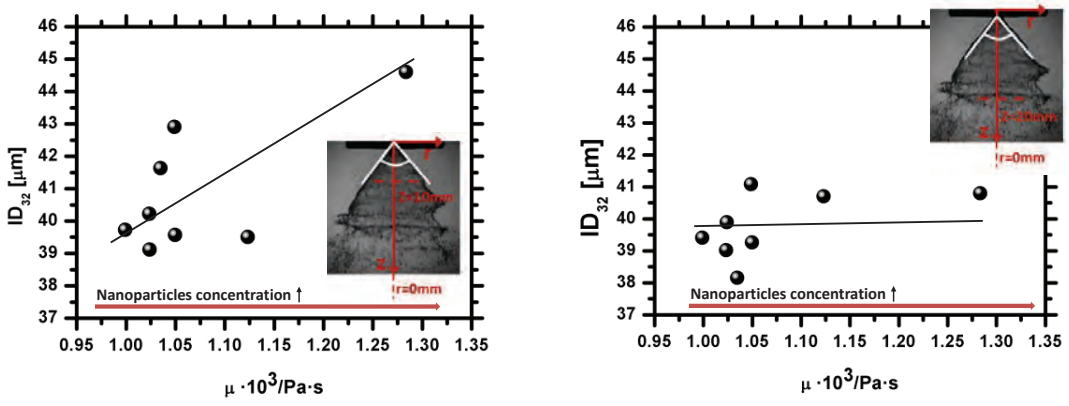

Figure 3 Effect of the nanoparticles concentration (represented in the nanofluids viscosity) on the characteristic size of the spray droplets. PDA measurements performed at a) z = 10 mm. b) z = 20 mm.

Conclusions

This work addresses the effect of nanoparticles concentration on the atomization processes of the resulting nanofluid sprays, to be used in the context of cooling applications.

Additional investigation is now required to widen the range of nanoparticles concentration and to study the spray dynamics and the heat transfer processes at imingement. However, these results are rather encouraging to use these nanoparticles for spray coooling applications, as they are able to enhance the thermal properties of the nanofluids without significantly compromising the spray characteristics, as the atomization processes in the fully developed region of the spray are mostly dominated by surface tension forces, which are hardly affected by the concentration of the nanoparticles.

Acknowledgements

This work has been partially supported by project No. 18-15839S funded by the Czech Science Foundation.

The authors are also grateful to Fundação para a Ciência e Tecnologia (FCT) for partially financing the research under the framework of the project RECI/EMS-SIS/0147/2012 and for supporting M. Maly with a research fellowship, during his stage at IN+. A. S. Moita acknowledges FCT for financing her contract and exploratory research project through the recruitment programme FCT Investigator (IF 00810-2015).

References

[1] Moreira, A.L.N., Moita, A.S., Panão, M.R., Prog. Energy Combustion Sci. 36:554-580 (2010).

[2] Kim, J., Int. J. Heat Fluid Flow 28(4):753-767.

[3] Maly, M., Moita, A.S., Jedelsky, J., Ribeiro, A.P.CP., Moreira, A.L.N., J. Thermal Analysis Calorimetry, In press (published online 12 June 2018).

[4] Duursma, G., Sefiane, K., Kennedy, A., Heat Transf. Eng. 30(13):1108-1120.

[5] Pererira, P., Moita, A.S., Monteiro, G., Prazeres, D.M.F., J. Bionic Eng. 11(3):436-259 (2014).

[6] Vieira, D., Moita, A.S., Moreira, A.L.N., 18th International Symposium on Applications of Laser and Imaging Techniques to Fluid Mechanics. Lisbon, Portugal, 04-07 July, 2016.

[7] Jedelsky, J. Jicha, M., App. Energy 132:485-495 (2014).

The dynamics of self-similar consumer sprays

H. Hinterbichler*, H. Steiner, G. Brenn
Institute of Fluid Mechanics and Heat Transfer, Graz University of Technology, Austria
*Corresponding author: hannes.hinterbichler@tugraz.at

Introduction

Spray flows may assume self-similar behaviour on which the modelling of their dynamics can be built. Self-similar phenomena in sprays were reported in many different works. For example, Li and Shen [1] demonstrated self-similarity of the mean axial droplet velocity, produced in air-assisted atomization using a coaxial nozzle with a high-speed air stream in the inner tube. Others modelled the spray as a variable-density single-phase jet [2-4]. They obtained similar results for the velocity decrease along the spray axis as in the case of the free submerged single-phase jet. Karpetis and Gomez reported on self-similarity of the gaseous flow field and the evaporation source term in spray flames [5]. In all the mentioned works, liquid and gas were injected simultaneously, often resulting in no slip velocity between gas and drops from close to the nozzle and therefore endorsing self-similarity as observed for single-phase jets. Our work, instead, focuses on the flow field of a spray, where the motion of the gas phase is induced by the ejected liquid phase exclusively, since only liquid is ejected from the nozzle. We show that this particular flow also exhibits self-similarity, although the cross-sectional average gaseous momentum flow rate increases downstream, which is not the case for a single-phase jet [6]. In the region of the spray investigated, the flow dynamics is dominated by the interfacial drag force, promoting the momentum transfer from the liquid to the gaseous phase. The interfacial drag forces depend on the velocity slip between the two phases, which therefore needs to be accurately quantified in the computational modelling of the flow field. Measuring the velocity of the gaseous phase by PDA as represented by the small-droplets velocities is a non-trivial task, though. We do not discuss the details of this aspect of the study here.

We first present the materials and methods used in the experiments, then show and discuss some important measurement results characterising the sprays, and finally deduce the self-similar behaviour of the gas flow field in the sprays. The paper ends with the conclusions.

Materials and methods

We investigate experimentally sprays generated with a standard consumer-type nozzle at two different consumer spray-typical liquid mass flow rates, using phase-Doppler anemometry (PDA). The measurements are carried out at selected cross sections of the sprays located between approximately 40 and 450 nozzle diameters downstream from the nozzle. The spray can may be considered as a simple pressurized single-phase dispenser with an approximate nozzle orifice diameter of $D_{or} = 0.4$ mm. Water is used as the test liquid. Two different liquid mass flow rates $\dot{m}_l$ of 2 g/s and 2.92 g/s are investigated in our experiments. All the measurements are carried out at temperatures of 20±1°C.

The experimental setup is depicted on the left-hand side of figure 1. The nozzle is mounted on a two-axes traverse and supplied with liquid from a pressurized tank. The laser light source of the DANTEC PDA system is a continuous Argon-Ion laser (Coherent Innova 90C-3). Two pairs of intersecting laser beams with the wavelengths 488 nm and 514.5 nm, respectively, form coinciding probe volumes (figure 1, right). The axial and radial velocity components u_l and v_l, as well as the diameter d of drops passing the probe volumes are detected. The geometrical parameters of the PDA system and the measuring ranges for the droplet properties are listed in table 1 for both liquid mass flow rates.

The sprays are considered as axially symmetric. Therefore, the measurement points are arranged along one radial axis r in each cross section of the sprays (see right hand-side of figure 1). Measurements are taken in several cross sections of the sprays with axial distances z from the nozzle exit ranging from 15 to 150 mm for $\dot{m}_l = 2$ g/s, and 15 to 180 mm for $\dot{m}_l = 2.92$ g/s. These ranges of the axial distance correspond to values of $z/D_{or} = 38$ to 375, and $z/D_{or} = 38$ to 450, respectively. In order to ensure sufficient statistical reliability of the PDA measurements, 100,000 samples were acquired at each measurement point. The edge of the spray flow field was defined at a radial position, where the detected drop frequency was 5 % of the maximum detection rate in the current spray cross section, or at least 300 Hz.

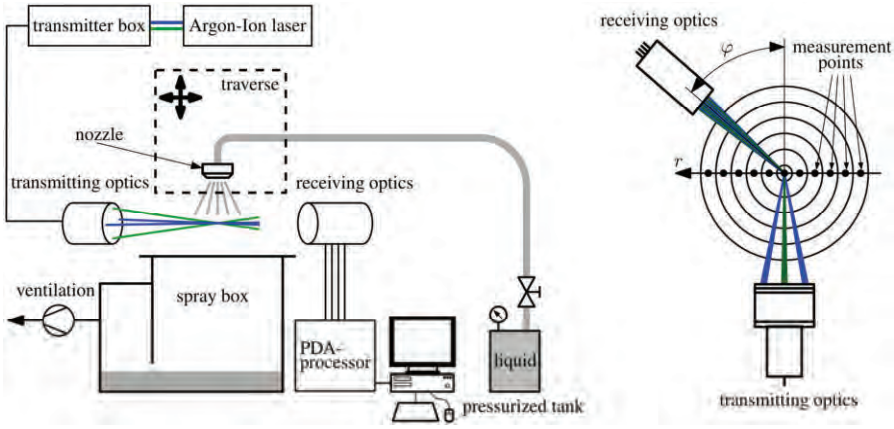

Figure 1. Experimental setup (left) and PDA optics (right).

Table 1. Geometrical parameters and measuring ranges of the PDA system.

PDA parameters	$\dot{m}_l = 2$ g/s	$\dot{m}_l = 2.92$ g/s
Scattering angle φ	50°	50°
Beam half angle	1.386°	1.386°
Phase factor P12	2.231°/µm	2.373°/µm
Phase factor P13	0.870°/µm	1.028°/µm
Measuring range d	up to 298 µm	up to 251 µm
Measuring range u_l	-63.8 to 63.8 m/s	
Measuring range v_l	-20.2 to 20.2 m/s	

Results and discussion

Spray properties

In the present section, exemplary mean quantities of the sprays are discussed. In figure 2, the mean droplet ter D_{10} and the mean axial drop velocity $\bar{u}_l$ are depicted for the liquid mass flow rates of $\dot{m}_l = 2$ g/s (left) and $\dot{m}_l = 2.92$ g/s (right). Due to the axial symmetry of the sprays, measurement points are concentrated on the positive half of the radial axis, whereas fewer points of measurement were placed on the negative half of the axis, mainly for checking symmetry. It can be seen for all displayed quantities that our assumption of axial symmetry is confirmed.

In the top row of figure 2, radial profiles of the arithmetic mean droplet diameter D_{10} are shown. For both cases, the smallest mean droplet diameters are found along the symmetry axis. The values increase towards the edge of the spray. This indicates that small droplets can be found rather in the dense region along the symmetry axis of the sprays, while larger drops with more inertia are found radially farther outwards. The mean drop diameter increases along the axis downstream, whereas the opposite is true in the radially outer regions of both sprays.

For the mean axial drop velocities $\bar{u}_l$ (see figure 2, bottom row), substantial differences between the two sprays generated at different liquid mass flow rates are observed. Whereas all profiles are rather bell shaped at the lower mass flow rate (left-hand side), two peaks in the mean axial velocity profile closest to the nozzle exit ($z = 15$ mm) are seen for the higher mass flow rate (right-hand side). Downstream, the profile shifts, and an additional third peak arises along the symmetry axis. The difference between the mean axial drop velocity profiles at the inflow of the two sprays may be attributed to the geometry of the nozzle and the state of flow. At larger flow rates, a hollow conical sheet is formed due to the swirl induced by the 90° redirection of the flow closely upstream from the nozzle exit.

Velocity of the gas flow field

Typically, the velocity of the gas flow field is deduced from PDA data under the assumption that the relaxation time scale of small droplets is very small, resulting in very small Stokes numbers. Therefore, the small droplets act like nearly massless tracer particles, representing the ambient gas flow field. This is especially true if the process of atomization is dominated by an independently imposed gas flow. However, for the present sprays the contrary is true.

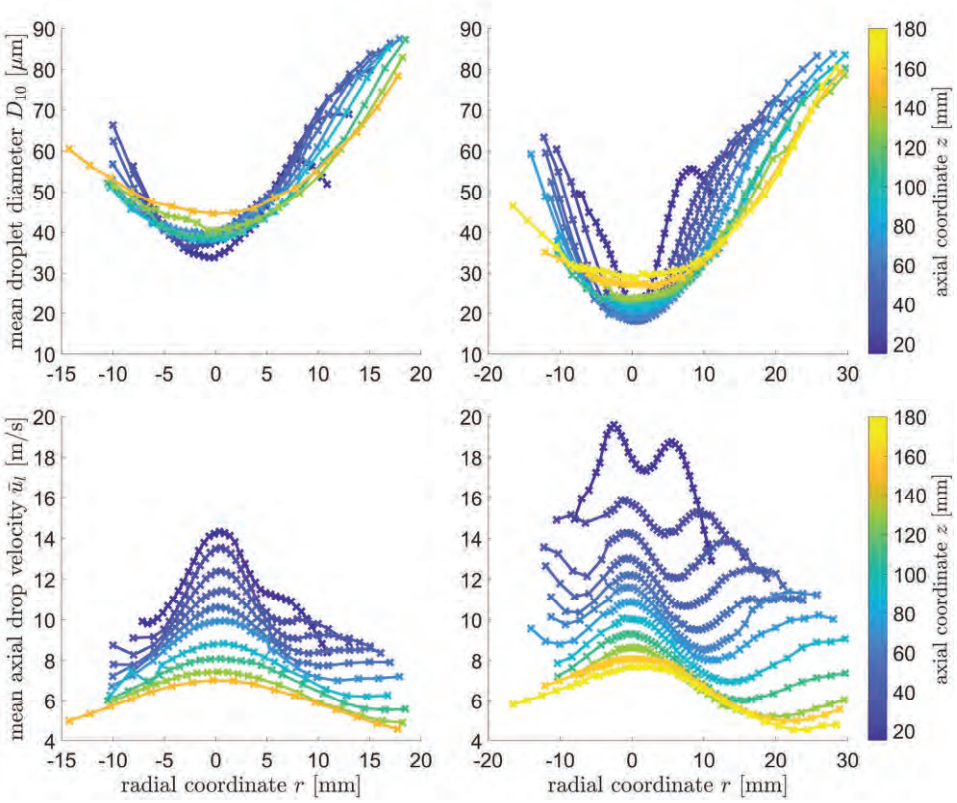

Figure 2. Experimentally measured spray properties: Left: $\dot{m}_l = 2$ g/s, right: $\dot{m}_l = 2.92$ g/s. Radial profiles of (top) number-mean drop size and (bottom) mean axial drop velocity.

Since only liquid is ejected from the nozzle, the gas phase is set into motion only due to the interaction with the droplets. Our measurements indicate that, especially in the cross sections close to the nozzle exit, not all small droplets act as tracer particles. A careful investigation shows that the velocity spectra of small droplets below 15 µm may be bimodal. For determining the gas velocity from the small droplet velocities, the drops forming the mode at the lower velocities must be used. Making use of for this we obtain gas velocity profiles as shown in figure 3.

Self-similar gas flow field

The analytical investigation of a possibly self-similar gas flow in the sprays assumes the flow field as a boundary layer-type flow. The corresponding boundary layer equations, with constant pressure in the flow field, transformed into a self-similar coordinate $\eta = Dr/(z - z_0)^{\alpha}$, with use of the stream function $\Psi = C(z - z_0)^{\beta}F(\eta)$ for the cylindrical flow field, yield the ordinary differential equation

$$(\beta - 2\alpha)F'^2 - \beta FF'' + \beta\frac{FF'}{\eta} = \frac{\nu}{C(z - z_0)^{\beta-1}}\eta\left[\eta\left(\frac{F'}{\eta}\right)'\right]' + \frac{E}{C^2D^4}\frac{\eta^2\omega_z}{(z - z_0)^{-4\alpha+2\beta-1-\gamma}} \qquad (1)$$

for the self-similar stream function $F(\eta)$, where the second term on the right represents the momentum source from the liquid phase $E(z - z_0)^{\gamma}\omega_z(\eta)$. The independence of z requires that $\beta = 1$ and $-4\alpha + 2\beta - 1 - \gamma = 0$. Determining the exponent α and the virtual pole of the flow z_0 by requiring that the ratio of the local axial velocity u in the flow field to the maximum value u_0 at $r = 0$ must be a constant along lines $\eta = \text{constant}$, and that the velocity along the symmetry axis $u_0(z)$ decreases $\propto (z - z_0)^{\beta-2\alpha}$, we get the values in table 2.

In figure 4 the normalized gas velocities are plotted as functions of the self-similar coordinate η divided by the constant D. The velocity profiles at various distances z from the nozzle exit collapse nicely on each other, showing the self-similar behaviour of the gas flow fields. The authors are presently working on the self-similar description of the momentum source from the liquid phase.

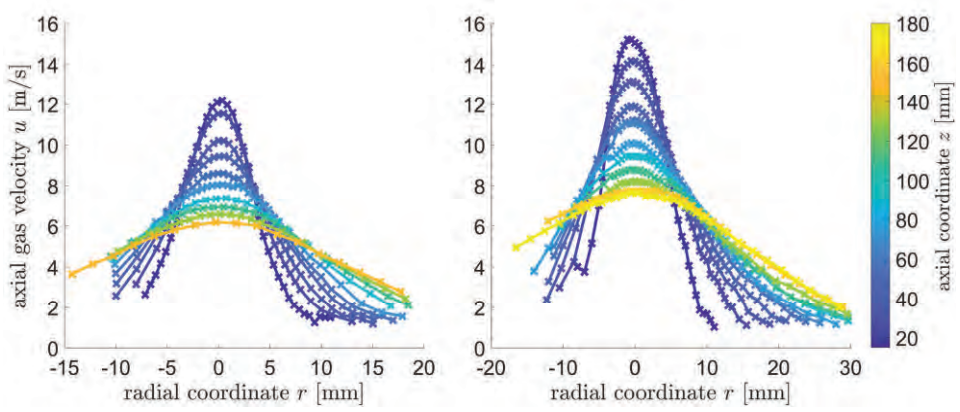

Figure 3. Axial velocity profiles of the gas flow field. Left: $\dot{m}_l = 2$ g/s, right: $\dot{m}_l = 2.92$ g/s.

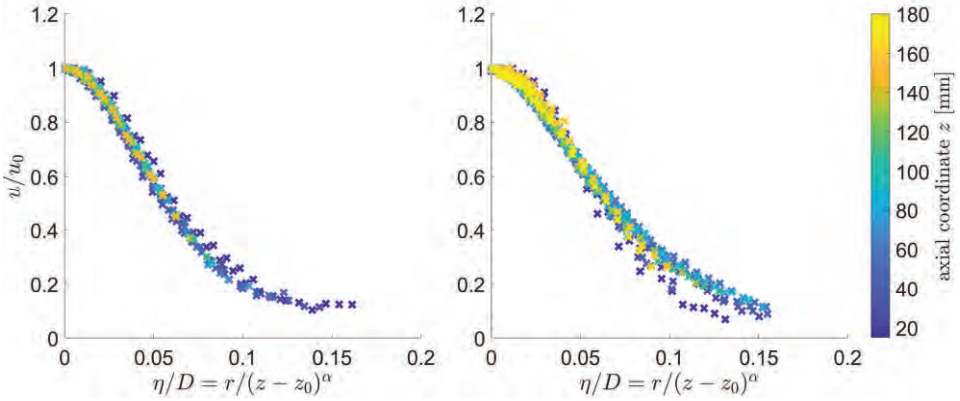

Figure 4. Self-similar profiles of the gas flow field. Left: $\dot{m}_l = 2$ g/s, right: $\dot{m}_l = 2.92$ g/s.

Table 2. Computed parameters to obtain a self-similar solution.

$\dot{m}_l$ [g/s]	2	2.92
α	0.67	0.70
z_0 [mm]	-2.5	-14.0

Conclusions

Consumer sprays were experimentally investigated with PDA at two different liquid mass flow rates relevant for the application. The measurements cover a region of the spray with large slip velocity between the liquid and the gaseous phases. We demonstrated a suitable approach to determine the velocity of the gaseous phase from PDA data, accounting for the bimodal velocity spectra observed for small droplets. This aspect was not detailed here. Furthermore, we show that the gas flow field of the spray can be represented in terms of self-similar variables, accounting for momentum transfer from the liquid to the gaseous phase. The observed decrease in the axial gas velocity with increasing downstream distance is significantly smaller than in a single-phase jet. Future tasks are the determination of the momentum source term from our PDA data and the solution of the self-similarity transform of the momentum equation.

References

[1] Li, X., Shen, J., Journal of Propulsion and Power 15: 103-110 (1999).
[2] Shearer, A.J., Tamura, H. Faeth, G.M., Journal of Energy 3: 271-278 (1979).
[3] Faeth, G.M., Progress in Energy and Combustion Science 9: 1-76 (1983).
[4] Panchagnula, M.V., Sojka, P.E., Fuel 78: 729-741 (1999).
[5] Karpetis, A.N., Gomez, A., Journal of Fluid Mechanics 397: 231-258 (1999).
[6] George, W.K., Advances in Turbulence (George and Arndt, eds): 39-73, Hemisphere, NY (1989).

Diesel fuel droplet impingement on heated surfaces

H. Jadidbonab*[1], I. Karathanassis[1], M. Gavaises[1]
School of Engineering and Mathematical Science, City, University of London
*Corresponding author: Hesamaldin.jadidbonab@city.ac.uk

Introduction

The impact of droplets on a solid surface is important in a number of industrial applications such as IC engines, fire suppression, thermal power plants and ink printing, among many others. Several parameters, such as droplet velocity, diameter and angle of impact [1], liquid physical properties [2], surface conditions [3], wall surface temperature (T_w) [4]and ambient pressure [5] are of key importance for the deformation of droplets upon impact and thus, define the impact outcome. Previous investigations show that the dynamic of droplet impact on a heated surface is different from those observed on a cold surface. in the present study, the impact of Diesel fuel droplets on a heated surface within a gaseous (air) environment at 1 and 2 bar has been investigated for a wide range of Weber number and surface temperature values employing both high speed visualization and CFD modelling.

Material and methods

The experimental setup and the image processing technique is shown in Figure 1 and comprises from the pressure chamber, the droplet generation system, the heated surface, the optical shadowgraphy system and the data acquisition system.

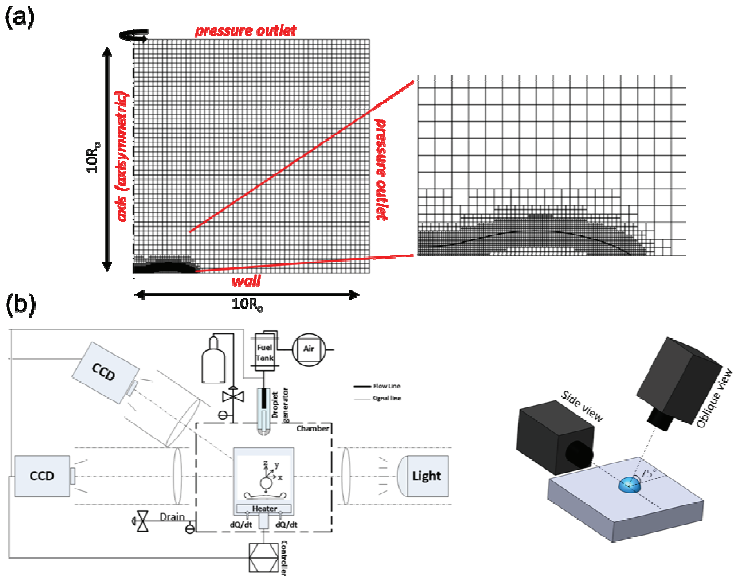

Figure 1: (a) 2D-axisymmetric computational domain and boundary conditions used for the simulation of Diesel droplet impingement and grid refinement of the liquid-gas interface (b) Schematic illustration of the test rig set-up utilised

The liquid used in this study was standard summer Diesel fuel with properties ρ=833 kg/m3, σ=28.9 mN/m and μ=2.7 cP at 25 °C. Droplet generation was achieved by a delicate electromagnetic injection system. Droplet injection and size was controlled from the compressed upstream air pressure and the opening time of the injector anchor; the achieved droplet size and velocity were in the range of 250-500 μm and 0.5-9 m/s, respectively. These correspond to impact Weber and Reynolds numbers in the range of 15-1000 and 91-1256, respectively. A transparent high pressure chamber equipped with three quartz glasses for optical access was utilized while experiments were performed at pressures of 1 and 2 bar; nitrogen was used to pressurize the chamber. The employed CFD model solves the Navier-Stokes equations for mass and momentum conservation, while it employs the VOF methodology to capture the liquid-gas interface. The energy equation coupled with a species transport equation for the vapour and a local evaporation model are utilized to simulate phase change [6]. The evaporation rate is based on the kinetic theory of gases, where

the driving force is the difference between the saturation conditions at the interface and the conditions on the vapour side.

Results and Discussion

In general, under the designated operating conditions, essentially six different macroscopic outcome regimes can have been identified, termed as: stick, splash, rebound, partial-rebound, breakup and breakup-rebound as illustrated in Figure 2.

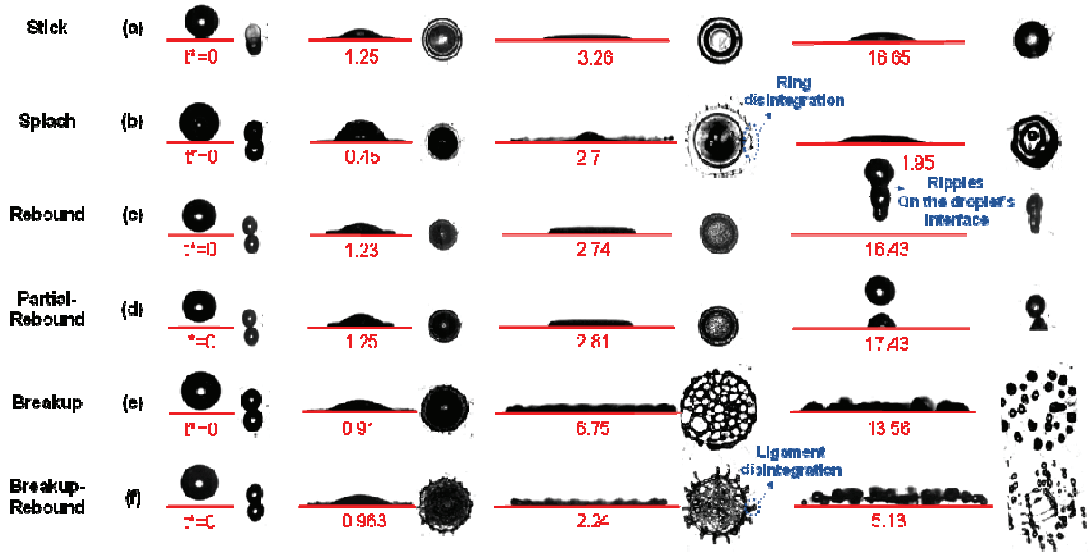

Figure 2: Temporal evolution of Diesel fuel droplet during impact on the heated flat aluminium surface for different values of Weber number and wall temperature; (a) stick regime at We=65, T_W=170°C; (b) splash regime at We=490, T_W=180°C; (c) rebound regime at We=65, T_W=350°C; (d) partial rebound regime at We=65, T_W=340°C; (e) breakup at We=490, T_W=340°C; (f) breakup-rebound regime at We=202, T_W=370°C

The impact outcomes are categorized and inserted into a non-dimensionalized map to identify the droplet impact based on the droplet Weber number (=$\rho U_0^2 D_0/\sigma$) and the surface temperature for the (Figure 3). Critical (We, T) pairs have been identified, which signify the transition to the breakup, splash and rebound regime.

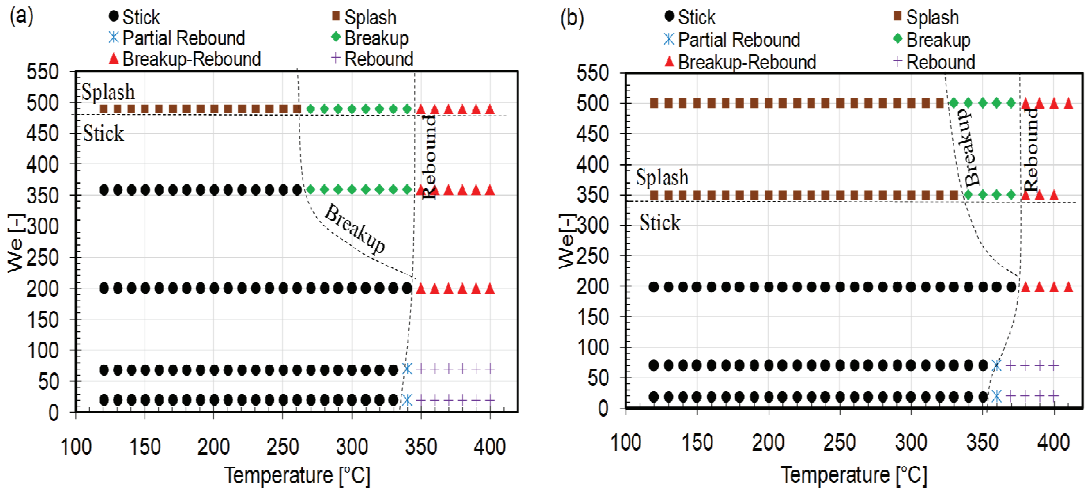

Figure 3: We-T regime diagram of Diesel fuel droplet impact on a heated aluminum surface at (a) P=1bar and (b) P=2bar

The effect of wall surface temperature and impact Weber number on wetting spreading factor and dynamic contact angle have been numerically and experimentally assessed (Figure 4 and Figure 5).

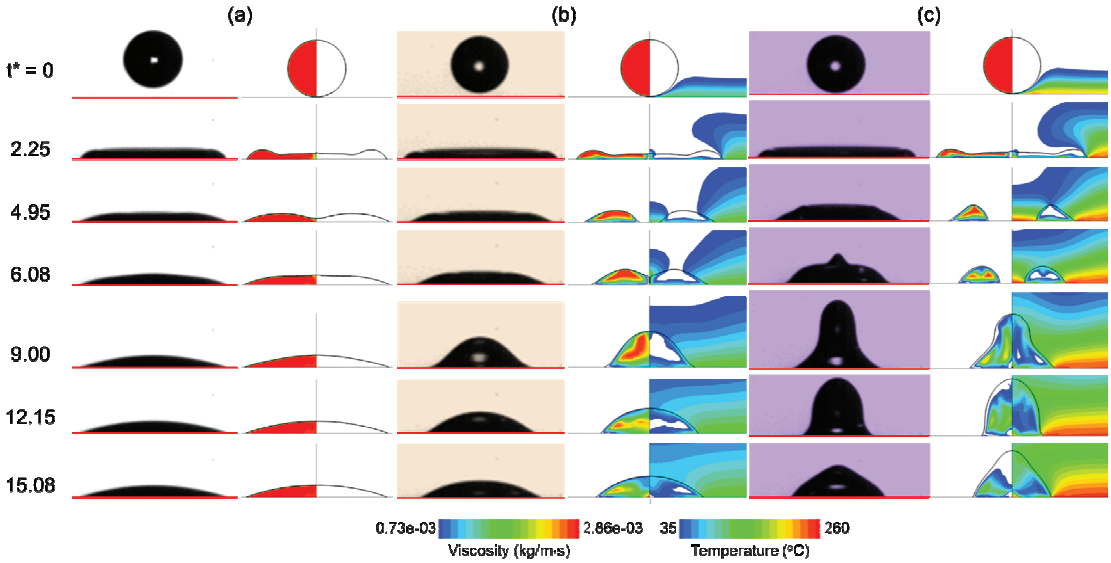

Figure 4: (a) Sequential images (experiment and simulation) of Diesel fuel droplet impact on a heated luminium surface for We=65 and P=1 bar: (a) T_W=25°C, (b) T_W=140°C and (c) T_W=260°C. For the simulation results, values of viscosity and temperature below

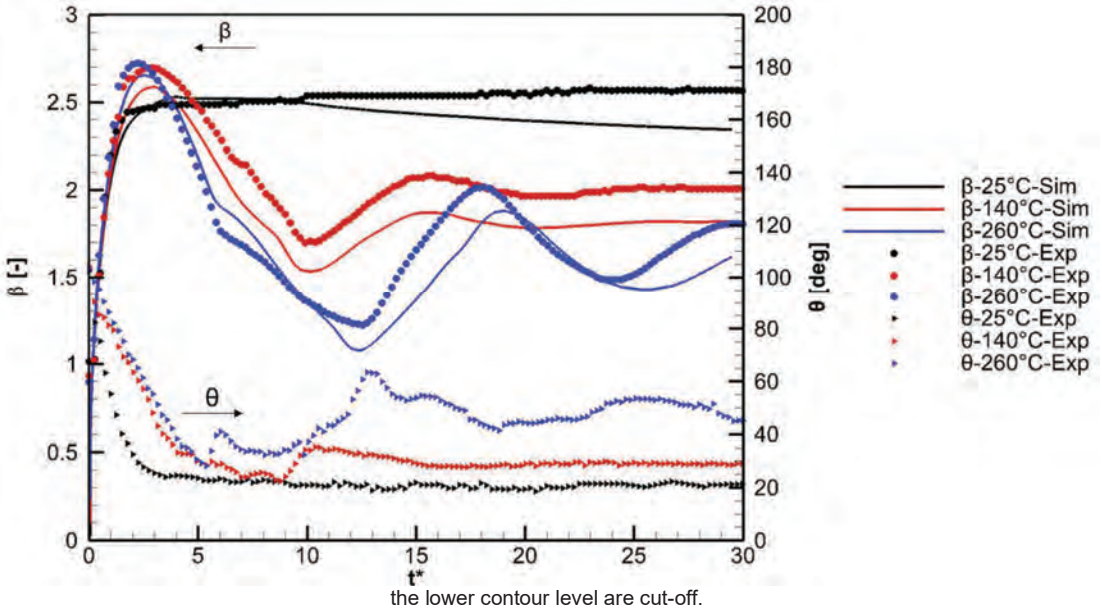

the lower contour level are cut-off.

Figure 5: Effect of surface temperature on time evolution of dynamic contact angle and spreading factor for We=65 and 1 bar chamber pressure at T_W=25, 140, 260°C

It has also been confirmed that by increasing wall-surface temperature, the droplet exhibits a strongly oscillating behaviour during the expansion and recoil phases, due to a reduction of liquid viscosity in the bulk of the liquid at higher surface temperature (Figure 6). This stronger recoiling behaviour also increases the value of the dynamic contact angle with the solid surface.

The effect of air pressure is quite insignificant on the wetting dynamic (Figure 7), however a weak suppression of the droplet spreading at P=2bar is observed, since the spreading factor obtains a lower value at P=1bar. This can be attributed to the increased aerodynamic drag effect at the triple contact point, as the density of the ambient air is doubled at 2 bar air pressure compared to atmospheric condition.

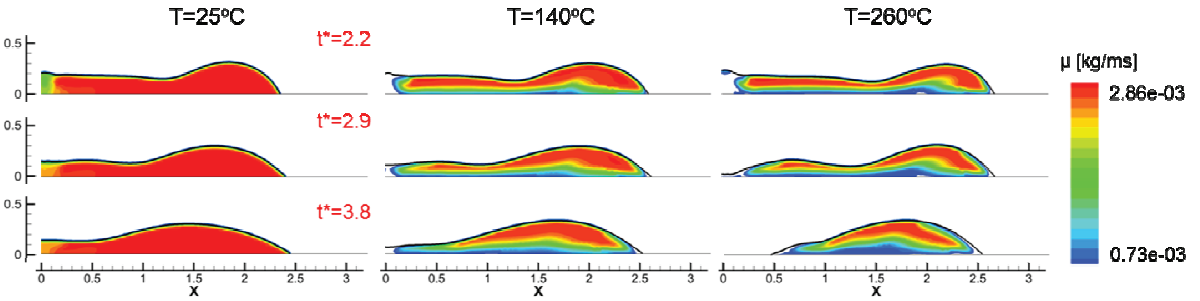

Figure 6: Droplet rim motion at 3 time instances (hysteresis and recoil) for 3 different surface temperatures of T_W=25, 140, 260°C,

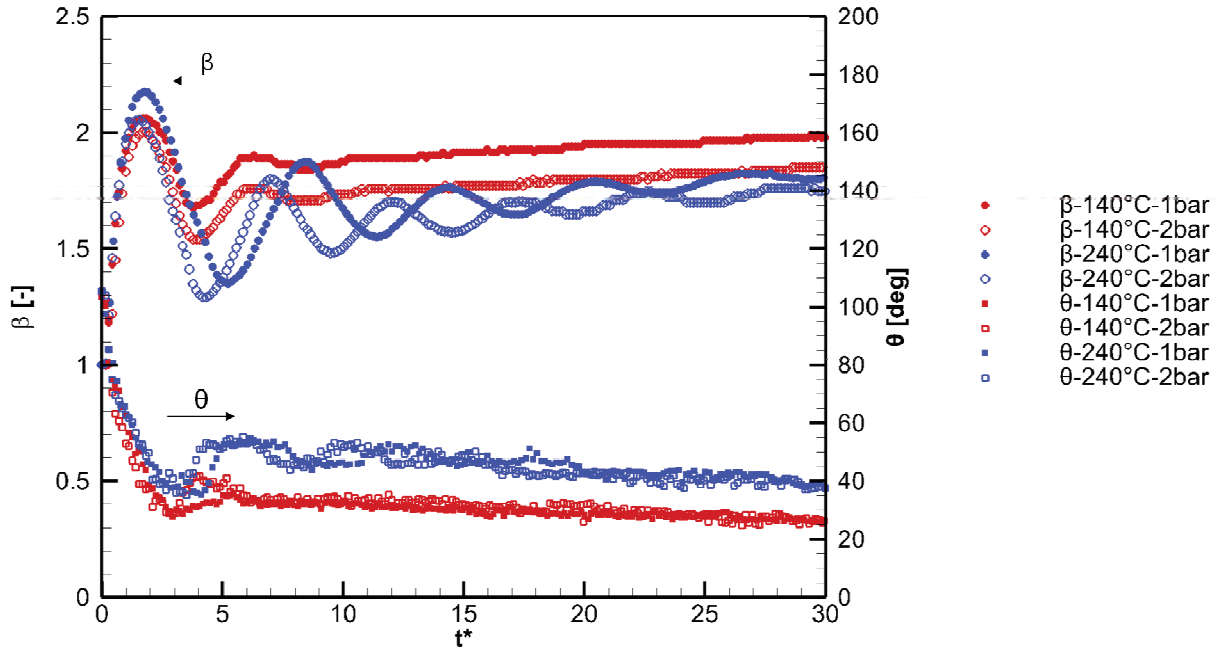

We=65 and 1 bar chamber pressure.

Figure 7: Temporal variation of (a) the dynamic contact angle θ and (b) spreading factor β for We=19 at TW=140 and 240°C

Nomenclature

T_L	Leidenfrost Temperature [°C]	t*	Dimensionless time ($t \times V_0/D_0$)
T_W	Wall surface temperature [°C]	We	Weber number ($\rho V_0^2 D_0/\sigma$)
P	Ambient pressure [bar]	V_0	Impact velocity [m/s]
ρ	Density [kg/m^3]	D_0	Droplet diameter at impact time [m]
σ	Surface tension [N/m]	μ	Viscosity [mPa.s]

References

[1] S. Yao and K. Cai, "The dynamics and Leidenfrost temperature of drops impacting on a hot surface at small angles," *Exp. Therm. Fluid Sci.*, 1988.

[2] R. Rioboo, C. Tropea, and M. Marengo, "Outcomes from a drop impact on solid surfaces," *At. Sprays*, 2001.

[3] Š. Šikalo, C. Tropea, and E. Ganić, "Dynamic wetting angle of a spreading droplet," *Exp. Therm. Fluid Sci.*, 2005.

[4] M. Shirota, M. van Limbeek, C. Sun, and A. Prosperetti, "Dynamic Leidenfrost effect: relevant time and length scales," *Phys. Rev.*, 2016.

[5] J. Liu, H. Vu, S. Yoon, and R. Jepsen, "Splashing phenomena during liquid droplet impact," *At.*, 2010.

[6] I. Malgarinos, N. Nikolopoulos, and M. Gavaises, "Numerical investigation of heavy fuel droplet-particle collisions in the injection zone of a Fluid Catalytic Cracking reactor, Part I: Numerical model and 2D simulations," *Fuel Process. Technol.*, vol. 156, pp. 317–330, 2017.

Experimental analysis of a GDI spray impacting on a heated wall

A. Montanaro*, L. Allocca
Istituto Motori CNR - Napoli, Italy
*Corresponding author: a.montanaro@im.cnr.it

Introduction

The greater control on the in-cylinder air-to-fuel ratio gives gasoline direct injection (GDI) engines the possibility to operate at higher compression ratios with respect to port fuel injection (PFI) ones, hence to achieve different charge characteristics depending on the specific load or speed, as the homogeneous mode for stoichiometric operation or stratified mixtures for lean overall operation. Since liquid fuel is directly injected into the combustion chamber, the fuel spray characteristics strongly influence the process of fuel-air mixing and combustion [1]. One important challenge for the GDI technology is that while it is essential to have a more uniform in-cylinder fuel distribution for better preparation of the combustion, the time available for fuel atomization and air mixing is very limited. Therefore, rapid atomization and vaporization of fuel spray are highly desirable. A key feature for better atomization is the fuel injection pressure. A higher injection pressure facilitates a higher atomization degree of fuel and vaporization but, at the same time, creates an over-penetrating spray so optimization is required [2]. However, due to the short distance between the injector nozzle and the piston head/cylinder walls, at high-injection pressure the fuel may impinge on walls before a fully vaporization and mixing with the air. On one hand, the spray impact accelerates the secondary atomization; on the other hand, a thin fuel film is deposited on the surface of the piston and/or the cylinder wall and both soot and un-burned hydrocarbon (UHC) were experimentally observed [3-6]. Therefore, a great need to characterize the DISI gasoline spray-wall interactions in details arises, not only to understand the fundamental transport processes, but to provide data to validate CFD predictions, too, which have become essential in the design of DISI engines.

Aim of this study is a detailed understanding of the interaction between the injected fuel and a flat wall under engine-like conditions, observing both the liquid and the vapour phases as the surface temperature varied (room to 573 K) in a controlled environment.

A customized algorithm, able to catch the contours of the liquid phase and the vapour/atomized zone, was used to extract the diffusion and evaporation parameters that characterized the impingement of the fuel.

Material and methods

The tests were performed in a constant-volume combustion vessel optically-accessible through three quartz windows allowing the admittance to the investigated area. A single-component fuel was used as fluid: iso-octane. The chosen injector was a solenoid-activated eight-hole direct-injection gasoline injector from the Engine Combustion Network (ECN) effort on gasoline sprays (Spray G). The nozzle holes are equally spaced and are 165 μm in diameter, according to the specifications. The injector was located on the top of the vessel in a holder including a jacket for the temperature setting of the nozzle nose and connected to a chiller for fluxing a cooling liquid. The fuel was supplied through a common rail system, heated by an electrical resistance and controlled in temperature by a J-type thermocouple based system located in the rail. Both the injector and the fuel temperature were kept at 363 K. The experimental work was carried out at the room temperature and atmospheric back-pressure except for the setting of the impinged wall temperature. Characterization of the spray impingement on a wall was made by introducing an 80 mm in diameter aluminum flat plate into the vessel, positioned 21 mm downstream the injector tip and facing orthogonal to the injector axis. The plate was heated in the range from 293 to 573 K (T_w) by electric resistances and controlled in temperature by a J-type thermocouple located in its center at 1.0 mm from the wall surface. Moreover, the spray-wall interaction was studied for three injection pressures, 5.0, 10.0, and 20.0 MPa. An optical setup of simultaneous Mie scattering and schlieren imaging techniques was applied for the spray-wall interaction test by using a Photron Fastcam SA4 high-speed camera to acquire the liquid/vapour spray at 25,000 fps with an exposure time of 39.33 μs. The arrangement was capable to acquire alternatively schlieren and Mie-scattering images in a quasi-simultaneous fashion using the same optical path. This methodology allowed complementing the liquid phases of the impact, obtained by the Mie scattering, with the liquid/vapor ones collected by the schlieren technique for determining both the phases inside a single cycle. The camera used a Tamron 90 mm lens with f-stop 1-2.8, with a spatial configuration realizing a resolution of 6.5 pixel/mm. More details on the adopted hybrid optical setup were reported in [7]. A homemade algorithm for image-processing was performed using a customized procedure developed under MATLAB platform to treat the batch and to outline the contours of the images.

Results and Discussion

Figure 1 reports an impacting spray sequence at different wall temperatures (from 293 to 573 K) from Mie scattering (top) and schlieren (bottom) optical technique. The imagines refer to the time step of 480 μs after the impact and the injection pressure is 20.0 MPa. For each column the effects of the wall temperature can be evaluated on liquid phase from Mie-scattering images and on both liquid and vapor from schlieren ones.

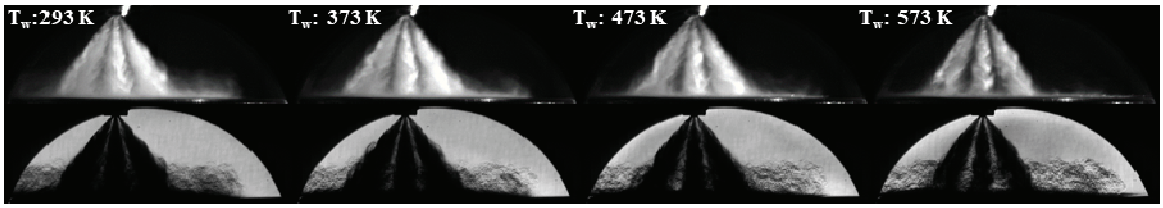

Figure 1. Mie scattering (top) and schlieren (bottom) impacting spray images at different wall temperatures

The impinging spray images showed an intact liquid core coming from the nozzle and flowing along the surface of the wall. Its maximum elongation in radial direction, as function of the time from the impact, was called “liquid width” and we referred to it as the intact liquid core. The impinged spray height (thickness) is considered as the maximum height in the perpendicular direction with respect to the impinged wall, which is caused by impingement regimes of splash, rebound or the free spray flowing over the thin film. The thickness of the intact liquid on the plate has not a regular shape, we refer to its maximum height as to “liquid thickness”. The liquid core is surrounded by an area composed of fuel vapour mixed to liquid ligaments and droplets more or less finely atomized. It extends itself on the plate beyond the “liquid width” and the “liquid thickness” and we refer to it as “vapor width” and “vapor thickness”. Five consecutive events were acquired for each injection condition for an evaluation of the jets spread. The increment of the wall temperature has an effect on both the liquid, with much dispersed droplets, and vapour phases. It determines a shift of the impact regime from deposition towards rebound or thermal break-up, thus leading to enhanced vaporization. Looking at the schlieren spray images in figure 1, the mixed area, overhanging the liquid portion (dark part immediately on the wall), includes ligaments, droplets more or less finely atomized and vapor phase. The growth of this area appears evident when the temperature increases.

Figure 2 depicts the liquid (on the left) and vapour width (on the right) behaviour of the impacted fuel while changing the wall temperature from room to 573 K at the injection pressure of 20.0 MPa.

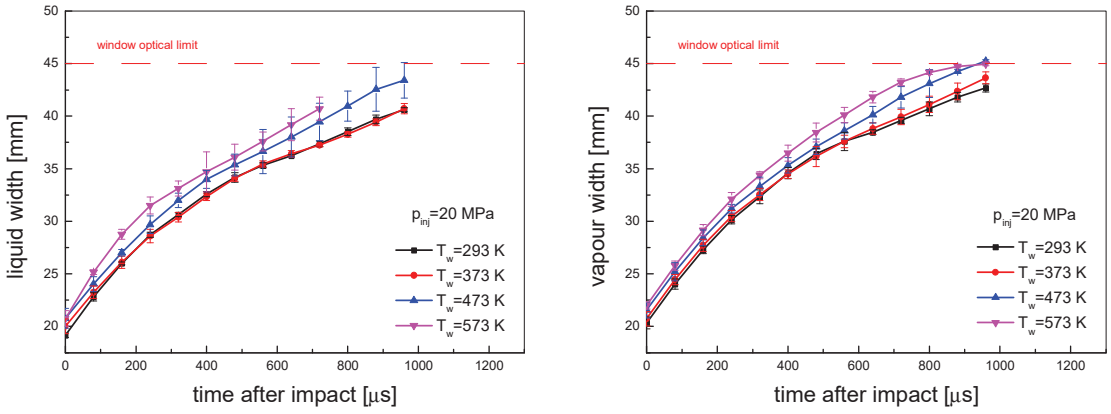

Figure 2. Liquid (left) and vapour (right) width at different wall temperatures

Both liquid and vapour profiles show a quasi-linear growth vs time for all the investigated wall temperatures. The increment of the wall temperature from 293 to 373 K doesn’t produce any effect on liquid and vapour slipping in fact the curves (black and red respectively) overlap all along the injection duration. For temperatures higher than vaporization value of the iso-octane (372 K), the curves show a well-scaled trend of both liquid and vapour length with respect to the wall temperature, the higher is the temperature and the faster the fuel slipping results.

The curves reported in Figure 3 depict the behavior of the liquid (left) and vapor thickness (right) rebounding from the wall surface as a function of the wall temperature at the same injection pressure of 20.0 MPa.

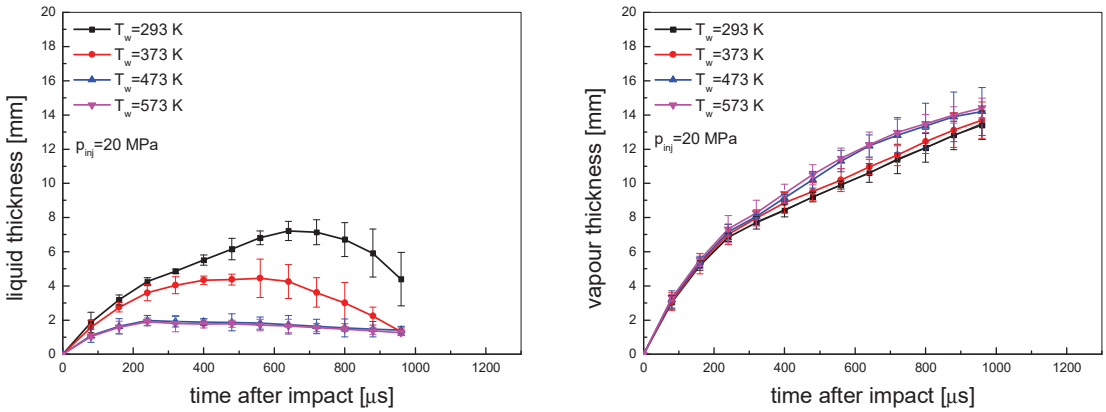

Figure 3. Liquid (left) and vapour (right) thickness at different wall temperatures

The increment of the temperature causes a reduction of the liquid thickness (on the left) and a growth of the vapour one (on the right). The thickness of the liquid phase shows an inverse trend with respect the wall temperature increase with a strongest rebound at room value (black line) and a quick tendency (at 473 and 573K) to saturate towards a stable value, around 2 mm, indicating a faster evaporation of the further incoming fuel. The behaviours of the vapour thickness curves are almost similar to the width ones (Figure 2) with a quasi-linear grow of the thickness up to the end of the injection process.

Finally, the effect of the injection pressure (ranging from 5.0 to 20.0) on both the liquid and the vapour phases after the impingement at the fixed wall temperature of 473 K was investigated. The injection duration was kept constant at 680 μs so the total amount of injected fuel increased with increasing of the injection pressure resulting equal to 5.0, 7.07, and 10.42 mg/stroke at 5.0, 10.0, and 20.0 MPa, respectively. Figure 4 reports the liquid (on the left) and vapour (on the right) width profiles as function of the injection pressure at the wall temperature of 473 K.

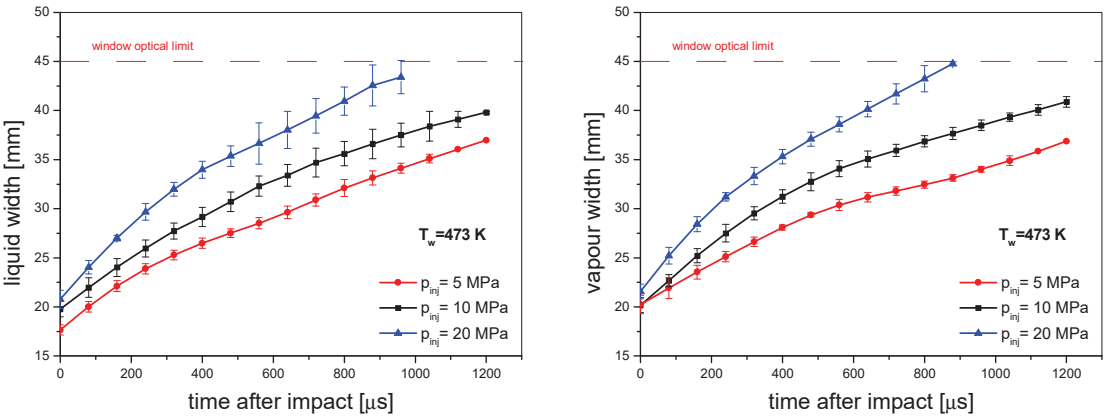

Figure 4. Effect of the injection pressure on liquid (left) and vapour (right) width at 473 K wall temperature

By increasing the injection pressure, the vapor phase increases prominently due to a finest atomization consequent the highest impact velocity and to an easier vaporization. The higher is the injection pressure, the longer is the width penetration because of the increased velocity (and the component parallel to the plate surface) of the impacting droplets. At impact completely developed, the gap between the curves slightly increases indicating a no-linear effect of the pressure on fuel slipping. Finally, the effect of the injection pressure was evaluated with respect to the thickness development, too. The results, here not reported for brevity, showed the vapour thickness increases with the increasing of the injection pressure while the liquid value remains stable around 2 mm and it is independent from the different injection pressures. More, liquid and vapour profiles begin to deviate each other just at the beginning of the impact, meaning that the existence of the vapour phase in addition to liquid one at 473 K as temperature of the wall is already present at the early stage of the impact and it is due to the vaporization process generated by the heat exchange with the plate.

Summary and Conclusions

Aim of this paper is a detailed understanding of the interaction and the heat exchange between injected fuel and heated wall under different engine-like conditions, studying both the liquid and the vapour phases as the wall

temperature varied from room to 573 K. Iso-octane was injected in a constant volume vessel, where gas was kept constant at atmospheric back-pressure and the injection pressure varied in between 5.0, 10.0, and 20.0 MPa. Mie-scattering and schlieren images techniques were coupled in a quasi-simultaneous timing to obtain information of both the liquid and the gaseous phases. A homemade software for the processing of the spray images was used to extract the diffusion and evaporation parameters that characterize the impingement of the fuel.

The optical technique combined with the adopted image processing procedure were well suitable to capture the peculiarities of the diverse phases of the fuel and were sensitive to the governing parameters:

- temperature: a scaling behavior of the liquid and vapor width/thickness vs. the time from the start of the impact
- injection pressures: a proportional increasing of the fuel slipping both along the radial and vertical direction

Finally, the data could be used to initialize and validate the spray-wall interaction models and to support the combustion system developments.

References

[1] Parrish, S., "Evaluation of Liquid and Vapor Penetration of Sprays from a Multi-Hole Gasoline Fuel Injec-tor Operating Under Engine-Like Conditions," SAE Int. J. Engines 7(2):2014, doi:10.4271/2014-01-1409.

[2] Zhao, F., Lai, M.C., Harrington, D.L., “Automotive Spark-Ignited Direct-Injection Gasoline Engines,” Progress in Energy Combustion Science, vol. 25, no. 5, pp. 437-562, 1999

[3] Drake, M.C., Fansler, T.D., Solomon, A.S., and Szekely, G.A., "Piston Fuel Films as a Source of Smoke and Hydrocarbon Emissions from a Wall-Controlled Spark-Ignited Direct-Injection Engine," SAE Tech-nical Paper 2003-01-0547, 2003, doi:10.4271/2003-01-0547.

[4] Lindagren, R. and Denbratt, I., "Influence of Wall Properties on the Characteristics of a Gasoline Spray after Wall Impingement," SAE Technical Paper 2004-01-1951, 2004, doi:10.4271/2004-01-1951.

[5] Behnia, M. and Milton, B.E., "Fundamentals of Fuel Film Formation and Motion in Si Engine Induction Systems," Energy Conversion and Management 42(15–17):1751-1768, 2001, doi:https://doi.org/10.1016/S0196-8904(01)00041-3.

[6] Stojkovic, B.D., Fansler, T.D., Drake, M.C., Sick, V. “High-speed imaging of OH* and soot temperature and concentration in a stratified-charge direct-injection gasoline engine”, Proc. Combust Inst., 30:2657-65, 2005. [1] Dukowicz, J., Journal of Computational Physics 2: 111-566 (1980).

[7] Montanaro, A., Allocca, L., and Lazzaro, M., "Iso-Octane Spray from a GDI Multi-Hole Injector under Non- and Flash Boiling Conditions," SAE Technical Paper 2017-01-2319, 2017, https://doi.org/10.4271/2017-01-2319.

Numerical simulations of planar jets stripping of liquid coatings

W. Aniszewski*[1], S. Zaleski[1], S. Popinet[1]
[1]Institut Jean le Rond d'Alembert - CNRS UMR 7190 - Sorbonne Universite, Paris, France
*Corresponding author: aniszewski@dalembert.upmc.fr

Introduction

In the process of *coating* - such as found in photography, lamination or metallurgy, a moving flat sheet of coated material (e.g. steel) emerges -- usually moving vertically -- from a bath of liquid coating material. Depending on parameters the resulting film formation process may be entirely laminar or turbulent [1]. This first stage process of film formation ends before film solidification, thus temperature evolution and energy can be disregarded. In some processes, the coat is complete after gravitational forming - in other applications it is modified.

In this work, we indeed focus on the *second stage*, which is modification of the formed coat/film by airflow, issuing from flat nozzles, known as "*airknives".* They strip excess coat from the product, resulting in film thickness orders of magnitude smaller than that formed in the first stage via gravity-governed flow. The airflow in the jets is strongly turbulent at Reynolds numbers Re > 15000, imposing high computation costs. Still, pressure profile converges to a bell-shaped curve centered at the impact line [2]. The resulting stresses modify liquid coat flow resulting in thinning of the coat above the impact zone.

Materials and methods

Numerical investigation of the coating mechanism benefit if the deposit is created gravitationally, even in the high-Reynolds number regime. Thus, our simulations include entire liquid coating basin filled with zinc, and the coated band up to the height at which nozzles are located (0.4m) with additional 0.25m - tall zone above to accommodate , resulting in a 0.65m - tall domain. In three dimensions, the upward-moving coated sheet/band is located in 0.2m wide domain's center. This, considering with a 10-100 μm coat thickness results in an extremely large range of scales. For a more precise study, we have also investigated another, more "academic" version of this study, wherein only half of the coated band is considered (with one air-knife present at its side) and a symmetry condition is used. Results from this setup are presented below.

Due to extreme range of scales, we apply the grid-refinement technique (local AMR, [3]) withing the in-house code *Basilisk* [5]**.** which is optimized for high efficiency in serial and parallel execution. The N-S solver uses finite differences, modern time progression schemes and Volume of Fluid method to track the interface. Even with that precautions, the computational cost of such simulation is prohibitive for current computers. We therefore limit the AMR technique in such way, that full resolution can be attained only close to the air-liquid impact zone and inside the nozzle. The former of these areas is where the gas-liquid momentum exchange takes place, and liquid is thinned by the airflow. The latter is obviously crucial as we need turbulence to develop properly inside the nozzle.

Results and Discussion

The simulation involves fully realistic industrial parameters: liquid density ϱ_l and viscosity μ_l correspond to liquid Zinc at ϱ=6500 kg m^3 and 0.00317 Pa s respectively. The upward-moving wall is first coated (the "first stage" mentioned in the Introduction) gravitationally, once it emerges from a bath full of liquid. The upward wall velocity is 2 m/s, which results in a turbulent withdrawal [1] (*Re* based on the zero-flux film thickness reaches 2500). One the coat is formed, airflow in the nozzle begins. The injection velocity u_{inj} is 200m/s, flat profile is injected. The distance between nozzle exit and the coated wall (and, hence, liquid film) is 1 centimeter. Coated wall is 0.512m tall, 0.15m wide (*z* extent) and 0.5mm thick. The nozzle slit is 1mm (measured along *y* axis). The nozzle is 0.25m wide (measured along *z* axis) and 0.511m long (measured along *x* axis). Naturally, the simulation domain is $0.512m^3$. It has to be noted that at the moment, the *Basilisk* code supports square/cubic domains only. Masks can be used to limit the simulation region shapes to non-cubic, however to simplify implementation we opt for a non-restricted, cubic domain with entire flow concentrated next to the '*x-'* wall. Since air injection is defined on the '*x+*' wall, air travels through entire domain length before issuing from the nozzle. This ensures - even numerically - a sufficient level of mixing in the airflow before it exits the nozzle.

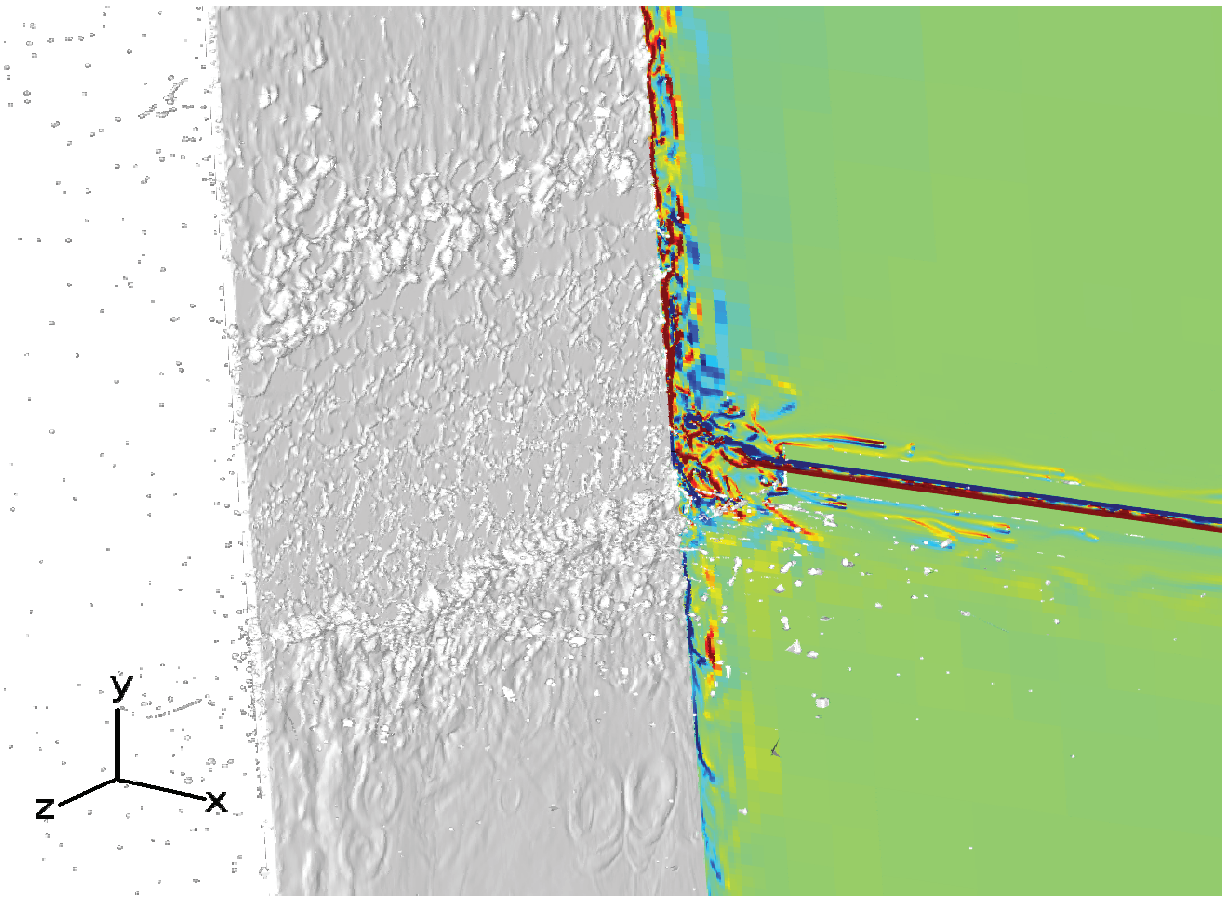

Figure 1. Film geometry at t=0.172s (i.e. 0.008s after impact). The nozzle, invisible in this visualization, extends in *z* direction and has a form of two flat plates (both parallel to *y*) separated by a *d*-sized slit (1mm in the simulation shown above). A cutplane is shown at *z*=0 colored by vorticity.

An example of a 3D coating simulation is visible in Figure 1 at 0.02s after the injection moment $t_{inj.}$ = 0.16s. In Figure 1, the interface is visible as a white/gray surface, with many ligaments and droplets in the impact zone. A cut-plane is placed at the z- wall, colored by vorticity ω. This helps us recognize the location of the "air-knife" (whose solid wall are not visible in Fig. 1 in order to not obscure the flow). We observe flat nozzle flow trace (along z axis). Pressure gradient restricts the flow within the film, so that a coat "bulge" is created below the nozzles with material crumbling down under gravity. Occasionally, the droplets impact back on the coat, resulting in circular wrinkles visible e.g. below the impact zone. The surface of the film is not strongly atomized, although it must be admitted that at the scale of Fig. 1, some small fluid packets might be simply to small to resolve visually, even if they're present in simulation. However, a stable thin film is created above the impact zone at thickness estimated at below 50 μm. This is a slight over-estimation compared e.g. to simplified model results of Hocking [6] and most likely results from lack of resolution.
Computational grid used for this simulation is non-uniform, with highest refinement level 12, which translates to minimal grid-size of $\Delta x=0.512/2^{12}=1.25\ 10^{-4}$m. (Some authors use the notion of grid equivalence between uniform-grids and these locally-refined. In such case, the 2^{12} grid has to be regarded as equivalent to a 4096^3 uniform grid). Despite this low resolution, it is possible using the Volume of Fluid [7] method that a computational grid-cell exists which is only partially filled, thus resolved film thickness may be smaller than Δx. Unfortunately such results have still to be regarded as preliminary and imperfect, since e.g. velocity field in such a thin film can not be correctly resolved. Thus, it is expected that much higher resolutions are needed to resolve the post-impact film thickness.

Figure 2 presents the side-view of the same moment in the simulated coating process as presented in Figure 1. In this view, the nozzle location is marked by semi-transparent dark region. Small liquid parcels are easily seen engulfed in the turbulent flow, some of them aligning with the vortical structures drawn in the back-drop cutplane. Note that Figure 2 is a three-dimensional image, thus we observe all droplets along the *z*-axis extent of the coated band at once. This effect of perspective has to be taken into account when examining Fig. 2, for example, accumulation of droplets is in fact somewhat lower than suggested by this image.

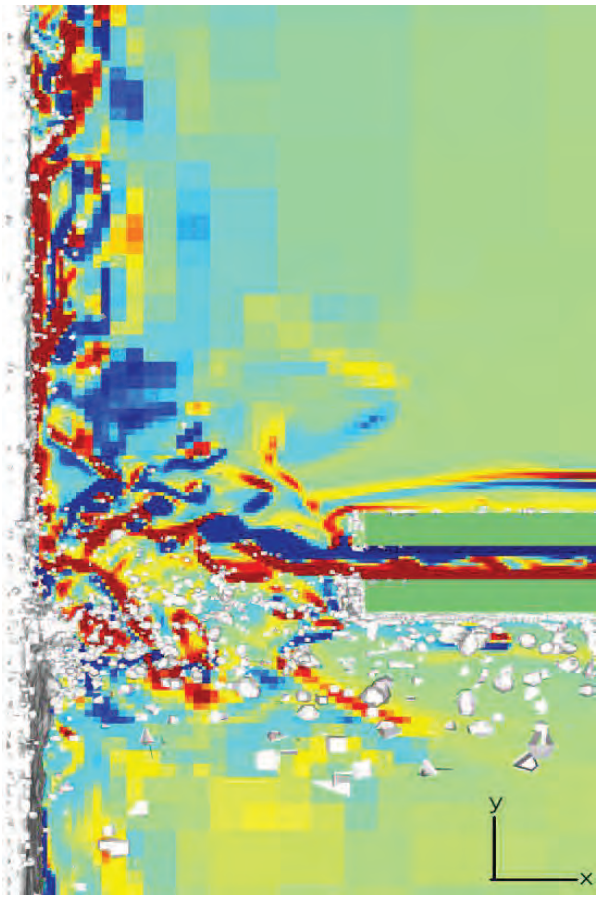

Figure 2. Film geometry at t=0.172s (i.e. 0.008s after impact) i.e. for exact same moment as presented in Figure 1. Lateral view with nozzle location marked by darkening. Decreased resolution far from the film is easily visible in the right hand side, upper part of the image.

Other useful fact that can be derived from Figure 2 is how the liquid packets are treated with lower resolution far from the film. We observe large grid-cells on the green cut-plane (colored by ω), but also, below the nozzle walls, we observe ejecta that is much less resolved that small droplets close to the impact zone. This is a result of intentional decrease of grid resolution far from the region of interest, and is a means to make the simulation feasible.

The simulations here are first of their kind, as the coating and airflow-coat interactions have never been simulated by a DNS approach with such detail in three dimensions. Previous results, e.g by Myrillas et al [8], have only provided time-averaged profiles of film shape. These profiles included no transient effects, and were two-dimensional. Simulations presented in this work are 3D and are eventually intended to reach the DNS resolutions close to the film. Results are expected to improve the control of the process in industrial practice (e.g. edge effects) and validate our analytical predictions for, among others, coat thickness above the injector, or the flow within heavy liquid during film formation. It is believed that by gradually converging the simulation resolution parameters to real-life values - which has to be accompanied by an increase in CPU processing power required - we will be able to achieve full stripping simulation which yields prediction about both film thickness and possible edge effects resulting from the interaction with airflow.

Nomenclature

u	velocity [m s^{-1}]
u_{inj}	gas injection velocity [m s^{-1}]
ω	vorticity [Hz]
ϱ_l	liquid density [kg m^3]
μ_l	liquid viscosity
m	mass [kg]

References

[1] P. Groenveld. Chemical Engineering Science,, 25:1259-l 266 ,1970.
[2] S. Kubacki, J. Rokicki, E. Dick Int. Journal of Heat and Fluid Flow 44 596–609, 2013
[3] S. Popinet Journal of Computational Physics 302 336–358, 2015
[4] Hsueh-Chia Cheng. Annual Review of Fluid Mechanics , 26:103-136, 1994.
[5] See website: www.basilisk.fr
[6] Hocking, G.C. et al. “Deformations during jet-stripping in the galvanizing process”. In: Kluwer Academic Publishers, 2010
[7] Popinet, S. “An accurate adaptive solver for surface-tension driven interfacial flows”. In: Journal of Computational Physics 228 (16 2009) pp. 5838-5866.
[8] Myrillas, Konstantinos et al. “Numerical modeling of gas-jet wiping process”. In: Chemical Engineering and Processing: Process Intensification 68 (2013), pp. 26 –31. ISSN: 0255-2701.

On the implementation of Structured Surfaces to FS3D

M. Baggio[1] and B. Weigand[1]
[1]Institute of Aerospace Thermodynamics, University of Stuttgart, Germany

Introduction: the DNS multi-phase code Free Surface 3D (FS3D)

Free Surface 3D (FS3D) is a multi-phase solver for the incompressible Navier-Stokes equations:

$$\frac{(\partial \rho \boldsymbol{u})}{\partial t} + \nabla \cdot [(\rho \boldsymbol{u}) \otimes \boldsymbol{u}] = -\nabla p + \nabla \cdot \mathbf{S} + \rho \boldsymbol{g} + \mathbf{f}_\sigma \tag{1}$$

Space discretization is based on finite volumes on a Cartesian grid. According to the VOF approach [1], the interface of the i-th phase is tracked by solving a transport equation for f_i:

$$\frac{(\partial f_i)}{\partial t} + \nabla \cdot (f_i \boldsymbol{u}) = 0 \tag{2}$$

where f_i is the volume fraction of the considered phase in the considered control volume.

Figure 1: Schematic overview of FS3D's numerical methods.

Representation of embedded boundaries

Similarly to [2], embedded boundaries are represented by their volume fraction f_b and their surface is approximated with the PLIC [3] scheme. The boundary is treated as a rigid body with infinite density. As a consequence, the fluid cannot enter those boundary cells ($0 < f_b < 1$) where the boundary occupies ($f_{b\,MCV} > 0$) 5 (3 in 2D) of the surrounding momentum control volumes (see figure 2). We bypass this problem with the following strategy:

- Identification of critical boundary cells (*slave* cells).
- Linking of *slave* cells to their neighbour (*master*) in the direction of the largest normal component $\boldsymbol{n}_b$.
- VOF-advection in *master-slave* couples.

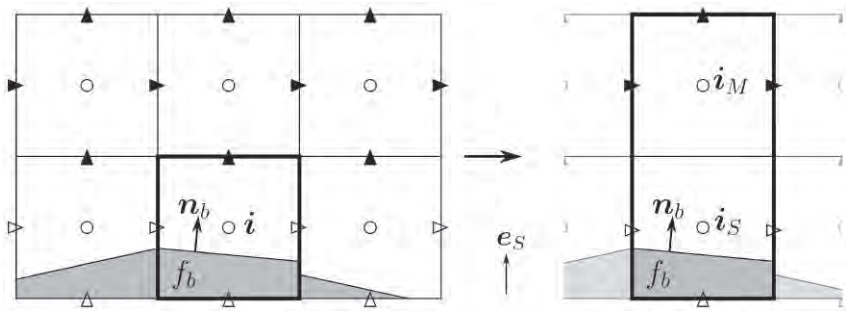

Figure 2: Left: "critical" boundary cell. Right: linking of this *slave* cell with its master. The vector $\boldsymbol{e}_S$ is the direction of the largest component of the normal vector $\boldsymbol{n}_b$.

FS3D's split advection scheme

VOF-advection occurs separately in each spatial direction [4], [3]:

$$\frac{f_i^* - f_i^n}{\Delta t} = -\frac{F_{i+\frac{1}{2}e_1} - F_{i-\frac{1}{2}e_1}}{\Delta x_i} + [(1-\beta)f_i^n + \beta f_i^*]\frac{u_{i+\frac{1}{2}e_1} - u_{i-\frac{1}{2}e_1}}{\Delta x_i} \tag{3a}$$

$$\frac{f_i^{**} - f_i^*}{\Delta t} = -\frac{F_{i+\frac{1}{2}e_2} - F_{i-\frac{1}{2}e_2}}{\Delta y_i} + [(1-\beta)f_i^* + \beta f_i^{**}]\frac{v_{i+\frac{1}{2}e_2} - v_{i-\frac{1}{2}e_2}}{\Delta y_i} \tag{3b}$$

$$\frac{f_i^{n+1} - f_i^{**}}{\Delta t} = -\frac{F_{i+\frac{1}{2}e_3} - F_{i-\frac{1}{2}e_3}}{\Delta z_i} + [(1-\beta)f_i^{**} + \beta f_i^{n+1}]\frac{w_{i+\frac{1}{2}e_3} - w_{i-\frac{1}{2}e_3}}{\Delta z_i} \tag{3c}$$

The first term on the right hand side is the contribution of the numerical fluxes through the cell boundaries; the second term is the divergence correction. Each one dimensional step in equations (3) requires three sub-steps:

- Interface reconstruction: calculation of interface position and interface normal vector $\boldsymbol{n}_b$.
- Geometrical calculation of the numerical fluxes F.
- Update of f by means of equations (3).

Each sub-step was adapted to the presence of the embedded boundaries.

Flux calculation in merged (*master-slave*) cells

An averaged velocity on master-slave upstream faces is used for geometrical calculation of the numerical fluxes (see figure 3).

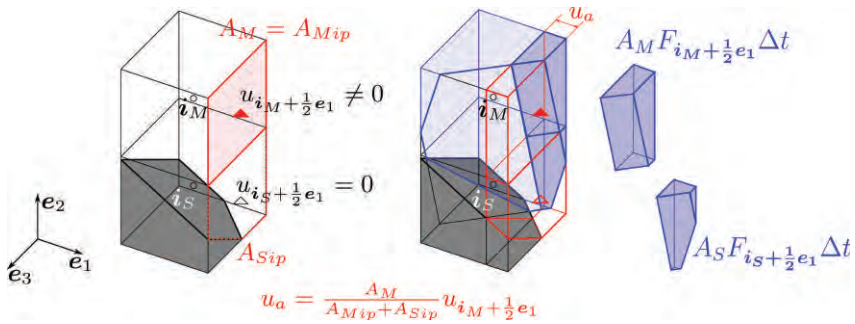

Figure 3: Left: velocity averaging on *master-slave* faces. Right: example of flux calculation in *master-slave* cells.

VOF-update in *master-slave* cells

Equations (3) are re-formulated as follows:

$$\frac{f_i^* - f_i^n}{\Delta t} = -\frac{F_{OUT} - F_{IN}}{V_{i_S} + V_{i_M}} + [(1-\beta)f_i^n + \beta f_i^*]\frac{\dot{V}_{OUT} - \dot{V}_{IN}}{V_{i_S} + V_{i_M}} \tag{4}$$

The divergence correction is modified to account for the presence of the boundary (see figure 4).

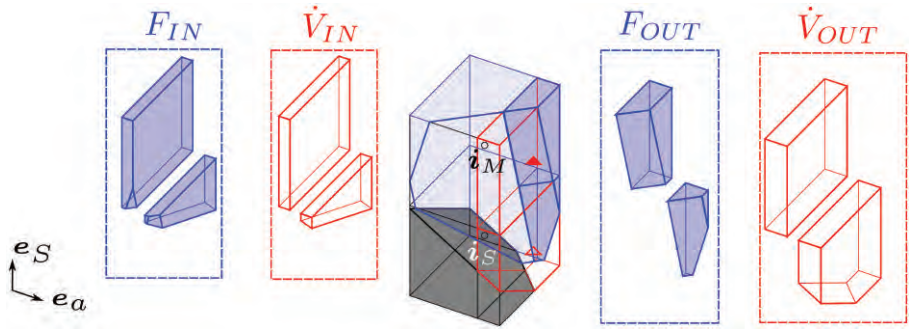

Figure 4: VOF-update in *master-slave* cells for the case $e_a \cdot e_S = 0$, where e_a is the advection direction, e_S. the direction by the largest n_b component in the slave cell.

Results

Results The method has been tested for drop impact on different geometries. The results for drop impact on hemispherical features are shown in figure 5.

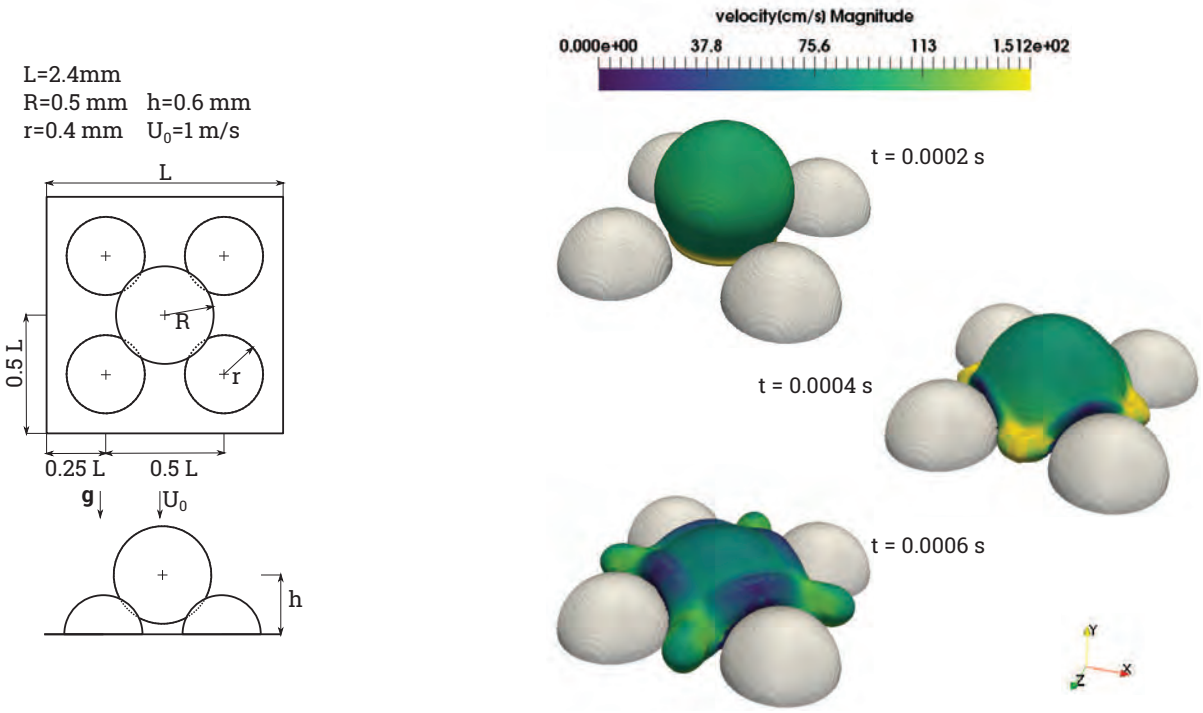

Figure 5: Results for drop impact on hemispherical features for $128 \times 64 \times 128$ computational cells.

Acknowledgements

We kindly thank the German Science Foundation (DFG) for the financial support within the international training group DROPIT (Droplet Interaction Technologies), GRK2160/1.

References

[1] C.W. Hirt and B.D. Nichols. In: *J. Comput. Phys* 1.39 (1981), pp. 201–225.

[2] P. Rauschenberger and B. Weigand. In: *J. Comput. Phys* 291 (2015), pp. 238–253.

[3] W.J. Rider and D.B. Kothe. In: *J. Comput. Phys* 2.141 (1998), pp. 112–152.

[4] M. Rieber. Doctoral thesis. University of Stuttgart, 2004.

Experimental Investigations on Multi-Phase Systems with X-Ray Micro-CT

R. Haide*[1], M. Santini[2], S. Fest-Santini[1]
[1]Department of Management, Information and Production Engineering, University of Bergamo, Italy
[2]Department of Engineering and Applied Sciences, University of Bergamo, Italy
*Corresponding author: robert.haide@unibg.it

Introduction

Micro-computed-tomography (micro-CT) provides a powerful tool for the visualization of interfaces in multi-phase systems. Obtained data can be used to validate or challenge existing models and hypotheses on multi-phase fluid displacement mechanisms and is essential in the derivation of boundary conditions for numerical simulations.

Material and Methods

Calibrated micro-porous model bodies of different complexity will be infiltrated with several fluid and scanned with the micro-CT setup, available at the University of Bergamo. The setup consists of a prototype X-ray source 160 kVp @ 200 µA, a high-precision air-bearing rotating stage and a custom-designed flat panel X-ray detector, based on an amorphous silicon sensor array. (See also [1])

For the current set of experiments, high-precision glass spheres were chosen to build up the solid matrix and water, air and n-dodecane present the variety of fluids.

Through scanning, the geometrical features of the solid structure can be characterized and the quality of the scans can be validated by comparing CT-derived parameters, such as porosity, specific surface area and pore size distribution to their analytically available values. The interfacial characteristics of the fluids can be analyzed and their evolution can be studied by conducting multiple scans at different states of saturation.

Preliminary Results and Discussion

Experiments, conducted to this date, illustrate the need for refinement of scanning strategies, in order to allow for accurate reconstruction of the scanned materials. Parameters, such as the voltage and amperage of the X-ray source, the sampling time and the used filters must be carefully optimized.

Another challenge poses the adequate segmentation of the resulting images. Here, different methods (e.g. Otsu [2]) need to be evaluated and post-processing strategies must be defined. (For further information see [3])

Robust and reliable algorithms need to be developed in order to analyze the obtained data thoroughly.

Pore network models can be generated from the obtained data and used to run simulations by help of an open-source software package [4].

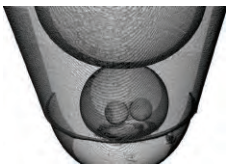

Figure 1. Reconstructed image of two glass spheres of a diameter of 1 mm , immersed in water and dodecane with air above

References

[1] Santini, M., Guilizzoni, M., Fest-Santini, S., X-ray computed microtomography for drop shape analysis and contact angle measurement, Journal of Colloid and Interface Science 409: 204-210, 2013.

[2] Otsu, N., A threshold selection method from grey-level histograms, IEEE Transactions on Systems, Man and Cybernetics 9(1), 1979.

[3] Schlüter, S., Sheppard, A., Brown, K., Wildenschild, D., Image processing of multiphase images obtained via X-ray microtomography: A review, Water Resources Research 50: 3615-3639, 2014.

[4] Gostick, J. et al., OpenPNM: A pore network modeling package, Computing in Science and Engineering 18(4): 60-74, 2016.

DNS-like simulations of atomization in the nozzle near field in plain-orifice atomizers

R. Payri, F.J. Salvador*, M. Crialesi
CMT-Motores Térmicos, Universitat Politècnica de València, Spain
*Corresponding author: fsalvado@mot.upv.es

Introduction

The understanding of the atomization process in energy generation is of fundamental relevance to achieve a cleaner combustion able to reduce the environmental impact. However, such an understanding is still not available due to the complex nature of this kind of multiphase flow. Multiphase DNS simulations are one of the most useful tools to obtain flow characteristics that can be effectively used to understand the flow physics and to interpret available experimental data.

As already proved in previous works [1], in this kind of simulations, the boundary inlet conditions for the spray are of great importance in order to accurately model the atomization process. In fact, it has been proved that turbulence is one of the main mechanisms that enhance and accelerates atomization process [2].

The present work aims to study the behavior of internal flow and effectively link it to the external flow. For the internal flow simulation, a Large Eddy Simulation approach has been used to model the turbulence structures inside a turbulent pipe (Re=5050). The open source code OpenFOAM has been chosen as a simulation environment, while an incompressible Wall Adaptive Local Eddy viscosity model has been selected to model the subgrid turbulence behavior. The simulation domain consists of a cylindrical pipe of L/D= 8, with a diameter of 90 μm.

Material and methods

For the external flow modelling, Direct Numerical Simulation (DNS) has been used due to its capability of providing a high amount of data on both space and time, while modelling all scales of motion in the flow. In this work the *one-fluid* method described in [3] and implemented in the PARIS-Simulator is used.

The main aim of this work is to effectively and accurately correlate the turbulence properties extracted from the analysis of the internal flow to the spray simulation though an algorithm for boundary condition generation. The algorithm used in this work is a *Digital Filter Based Method* from [4], which allows to control the size of the turbulent structures, their location and their temporal distribution, while maintaining the random behavior typical of the turbulent flows. This method calculates punctually the velocity turbulent component as:

$$u' = \sum_{n=-N}^{N} b_n r_{m+n} \qquad (1)$$

Where b_n are the filter coefficients, r_{m+n} are the zero-mean random data series components, N represents the filter support length and m indicates the grid point.

In order to determine the filter coefficients, the assumption of a fully developed homogeneous turbulent field is made in [4], consequently the autocorrelation from [5] for the u' is used as:

$$R_{u'u'}(d, 0, 0) = exp\left(\frac{\pi d^2}{4L^2}\right) \qquad (2)$$

Where L is the prescribed integral scale and d is the distance vector. Through the correction of these coefficients the temporal and spatial distribution of the turbulence can be adjusted, acting on the integral length scale, adequately interpreted for the time.

Finally, the velocity profile, as well as the radial turbulence distribution, needs to be implemented in the code. The velocity profile can be implemented once the linear wall correlation and the log-law wall respectively have been verified for the inner nozzle flow upstream of the spray simulation:

$$y^+ = y^+ \; ; \; u^+ = \frac{1}{\kappa} ln\, y^+ + B \tag{3}$$

Where κ is the von Karman constant and B is a fitting constant.

In order to determine the turbulence radial distribution, the coefficients of the diagonal form of the Reynolds stress tensor $a_{ii}(r)$ must be determined as function of the radius, so that the determination of the velocity can be achieved through the equation below:

$$u(r,t) = U \cdot f(r) + u'(t) \cdot a(r) \cdot I \tag{4}$$

Where $f(r)$ is a correlation derived from the solution of equation (3), by determining B and y^+ through the LES analysis and I is the turbulence intensity. The velocity profiles, as well as the turbulence distribution and maximum intensity can be obtained from the statistical analysis of the internal flow and validated against experimental results [6] and DNS results [7].

Results and Discussion

In Figure 1 the external spray (left) and vorticity (right) are depicted for two different cases. In the upper part, the case without considering turbulence inside the nozzle (flat profile without any velocity fluctuation) is represented. In the lower part, the case with a turbulence intensity of 5% and integral Length scale of *L*=0.1 *D* is shown.

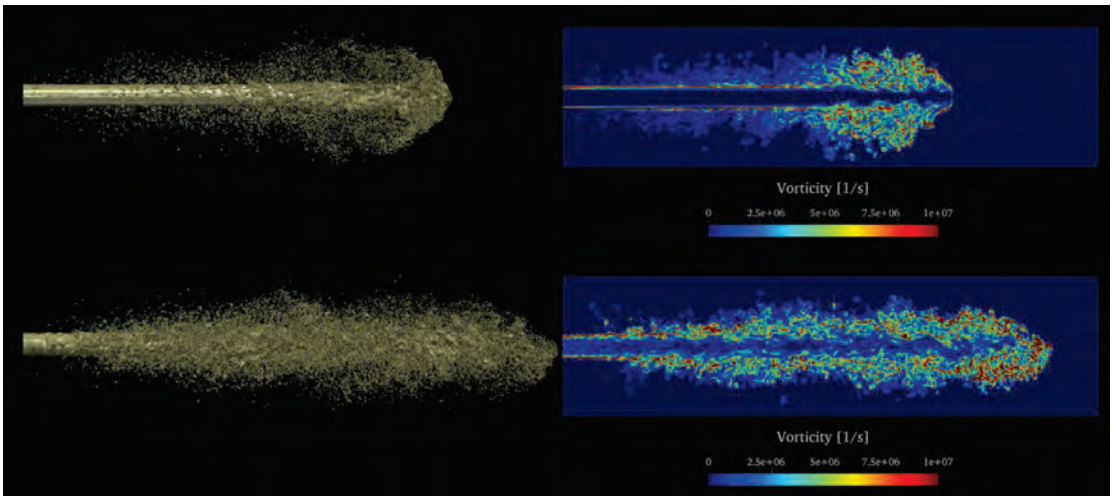

Figure 1. External appearance of the atomization process and vorticity for cases without turbulence inside the nozzle (upper part) and considering turbulence inside the nozzle (lower part).

As it can be noted, the atomization in the case where a flat velocity profile is used and turbulence is not considered (upper part of Figure 1), the atomization is very poor. In this case, it can be seen a long non-perturbed external length characterized by the presence of small quantity of droplets and atomization is produced mainly in the front of the spray, near of the spray tip characterized by the typical mushroom shape where, as can be seen in the upper part (right) of the Figure 1 vorticity is higher. On the other hand, in the case where a real velocity profile provided by LES simulation of the nozzle flow and so, considering turbulence, depicted in the lower part of that Figure, atomization starts faster and, therefore, closer to the nozzle exit. It can be noted that the number of droplets dramatically increases. In the right-hand picture, the vorticity field is depicted where it can be highlighted that maximum values are not only located in the front of the spray but even closer of the nozzle exit.

In Figure 2, the intact core length for the case considering turbulence is depicted. In the top, the time-averaged of the fuel volume fraction field is shown, where the typical cone shape representing the maximum probability of finding pure fuel is clearly seen. The same information is depicted in the bottom of the Figure but in this case for a given instant, and so, showing a more chaotic behavior.

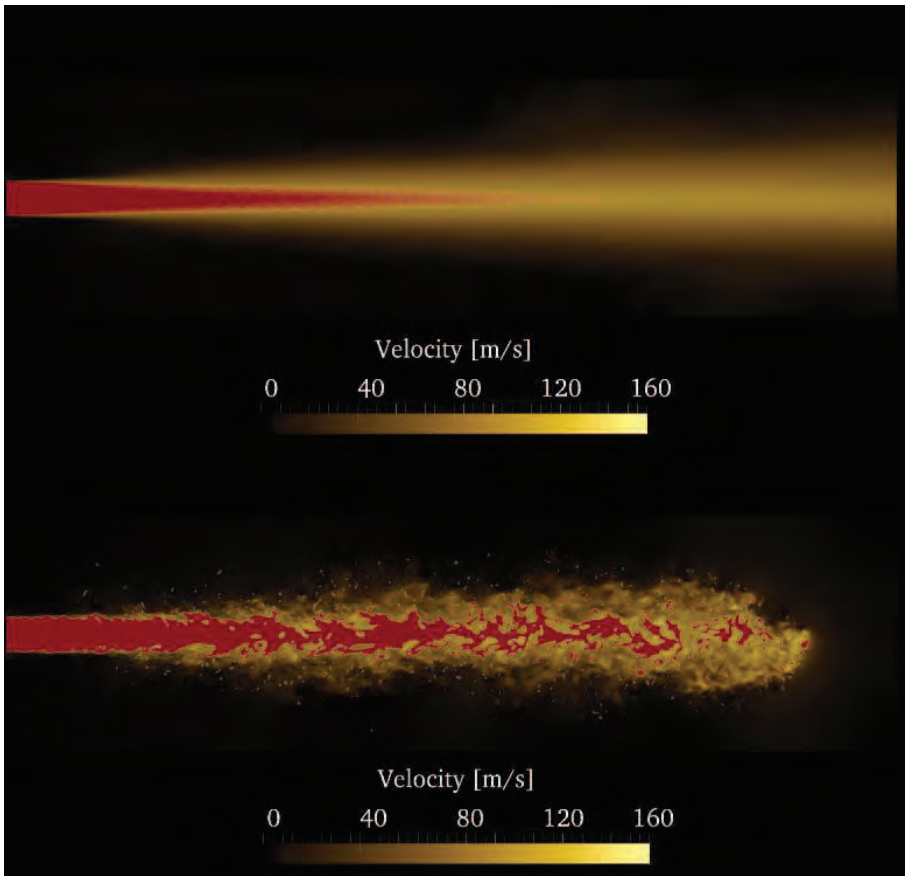

Figure 2. Time-averaged internal core length and instantaneous core length for the case considering turbulence inside the nozzle (Intensity, *I*= 5%, turbulence length scale L=0.1 *D*).

As a conclusion, it can be drawn that VOF DNS-like simulations are a powerful tool to study the mechanisms that enhance the atomization and it is of primary importance to take into account the turbulence generated in the nozzle since turbulence greatly improves atomization process, increasing the number of droplets and drastically reducing the external non-perturbed length and intact-core length. Further details on this investigation can be found in [8].

Nomenclature

B	Logarithmic law constant [-]
D	Nozzle Diameter [m]
I	Turbulence Intensity [%]
L	Turbulent lengthscale [m]
R	Autocorrelation function [-]
Re	Reynolds number [-]
U	Velocity mean component [m/s]
b	Filter coefficient [-]
d	Distance vector [m]
n	Discrete lenghtscale [m]
r	Random component [-]
u	Velocity field [m/s]

u' Velocity fluctuating component [m/s]
y^+ Non-dimensional wall distance [-]

References

[1] Salvador, F. J., Romero, J.-V., Roselló, M.-D., and Jaramillo,D. Numerical simulation of primary atomization in diesel spray at low injection pressure, J. Comput. Appl. Math., vol. 291, pp. 94–102, 2015.
[2] Reitz, R.D., and Bracco, F.V., Mechanism of atomization of a liquid jet, Phys. Fluids, vol. 25, no. 10, pp. 1730–1742, 1982.
[3] Ling, Y., Zaleski, S. and Scardovelli, R., Multiscale simulation of atomization with small droplets represented by a Lagrangian point-particle model, Int. J. Multiph. Flow, vol. 76, pp. 122–143, 2015.
[4] Klein, M., Sadiki, A. and Janicka, J., A digital filter based generation of inflow data for spatially developing direct numerical or large eddy simulations, *J. Comput. Phys.*, vol. 186, no. 2, pp. 652–665, 2003.
[5] Batchelor, G. K. The theory of homogeneous turbulence. Cambridge university press, 1953.
[6] Eggels, J. G. M. et al., Fully developed turbulent pipe flow: a comparison between direct numerical simulation and experiment, J. Fluid Mech., vol. 268, no. 1, p. 175, 2006.
[7] El Khoury, G. K., Schlatter, P., Noorani, A., Fischer, P.F., Brethouwer, G. and Johansson, A. V. Direct numerical simulation of turbulent pipe flow at moderately high reynolds numbers, Flow, Turbul. Combust., vol. 91, no. 3, pp. 475–495, 2013.
[8] Salvador, F. J., Ruiz, S., Crialesi-Esposito, M., Blanquer, I., Analysis on the effects of turbulent inflow conditions on spray primary atomization in the near-field by DNS , ,InternationalJournalofMultiphaseFlow102,pp.49-63,2018.

Visual Analysis of Interface Deformation in Multiphase Flow

Alexander Straub*[1], Grzegorz K. Karch[1], Sebastian Boblest[1], Jonas Kaufmann[1],
Filip Sadlo[2], Bernhard Weigand[1], Thomas Ertl[1]
[1]University of Stuttgart, Stuttgart, Germany
[2]Heidelberg University, Heidelberg, Germany
*Corresponding author: alexander.straub@visus.uni-stuttgart.de

Introduction

This project aims at investigating droplet-related phenomena, especially the influence of forces acting on the surface. To this end, we visualize interface deformation using two quantities: interface stretching and interface bending. This allows the visual analysis of droplet behavior and interface-related forces, such as the surface tension force and forces induced by Marangoni convection. For the latter, we show an application case for debugging and aiding the implementation of the Marangoni term in the solver *Free Surface 3D* (FS3D) [1]. Furthermore, we demonstrate the usefulness of our approach for prediction of droplet breakup.

The simulation data used in this context was generated by the solver FS3D and consists of a *volume of fluid* (VOF) [2] field and a velocity field, stored on a rectilinear grid. For interface reconstruction, *piecewise linear interface calculation* (PLIC) [3] was used. This is the same method as in FS3D and therefore yields results closest to the simulation concerning the surface and the topology of the fluid phases.

Interface Stretching

As a measure for interface stretching, the metric tensor is used, which represents the first fundamental form from differential geometry, defined for the deformation rate of the fluid surface. This technique was already introduced by Obermaier et al. [4]. Note that, while we are speaking of interface stretching, we acknowledge the fact that there cannot be an actual stretching because on a molecular view, this means that whenever the interface is *stretching*, molecules are just moving from the inside of the fluid to the interface. However, we use this expression as it conveys the idea as easily and graphically as possible.

To calculate the deformation gradient tensor **F** for a single time step, we can solve the equation

$$\Delta \boldsymbol{x}' = \Delta \boldsymbol{x} + \Delta \boldsymbol{d} = (\boldsymbol{I} + \boldsymbol{J_u}\Delta t)\Delta \boldsymbol{x} = \boldsymbol{F}\Delta \boldsymbol{x}, \quad (1)$$

with displacement $\Delta \boldsymbol{x}$, the change of displacement $\Delta \boldsymbol{d}$, the identity matrix $\boldsymbol{I}$, the Jacobian matrix $\boldsymbol{J_u}$ of the velocity field $\boldsymbol{u}$, and the time step Δt. Using two orthonormal vectors on the PLIC interface and generating the matrix $\boldsymbol{N} = (\boldsymbol{e_r}, \boldsymbol{e_s})$, we get the metric tensor defined on the PLIC plane spanned by $\langle e_r, e_s \rangle$ as

$$\mathbf{I_f} = (\boldsymbol{FN})^T(\boldsymbol{FN}) \quad (2)$$

From this, the eigenvectors and corresponding eigenvalues can be calculated. While the square roots of the eigenvalues $\sigma_i = \sqrt{\lambda_i}$ directly give the stretching factors, thus $\sigma_i > 1$ indicating stretching and $\sigma_i < 1$ indicating contraction, the eigenvectors $\boldsymbol{\epsilon_i}$ have to be transformed back to 3D space by multiplying with the matrix of the PLIC vectors, hence $\boldsymbol{\epsilon_i}' = \boldsymbol{N}\boldsymbol{\epsilon_i}$. They represent the stretching direction.

Interface Bending

As interface bending, we understand the change of curvature at an interface position $\boldsymbol{x}$ from one time step to the next. For its calculation, we now use the shape tensor. This tensor can be calculated from the paraboloid difference of two paraboloids fitted to the interface using least squares, one for the original interface positions, and one for their convected counterparts, as shown in figure 1. The idea to calculate the interface curvature from paraboloid-fitting was discussed by Popinet [5] and is part of the method used in the solver FS3D for the calculation of the interface curvature and the

surface tension force. The convection is computed by using a modified, local velocity field, where for the neighborhood around a position $\boldsymbol{x_c}$, the velocity is set to

$$\tilde{\boldsymbol{u}}(\boldsymbol{x_i}) = \boldsymbol{u}(\boldsymbol{x_i}) - \boldsymbol{u}(\boldsymbol{x_c}) - \boldsymbol{\omega} \times \boldsymbol{x}_i. \tag{3}$$

Here, the advection velocity is set to the original velocity minus the velocity at the center and a possible rotation of the interface, where $\boldsymbol{\omega}$ is the average angular velocity. This ensures, that both paraboloids share the same origin and orientation. An example of this is shown in figure 1. The set of advected interface points is thus given by

$$\boldsymbol{x_i'} = \boldsymbol{x_i} + \Delta t\, \tilde{\boldsymbol{u}}(\boldsymbol{x_i}). \tag{4}$$

The paraboloid difference is then $p_d = p_{adv} - p_{orig} = a_0 r^2 + a_1 s^2 + a_2 rs$ and can be used to define the shape tensor

$$\boldsymbol{S} = \begin{pmatrix} 2a_0 & a_2 \\ a_2 & 2a_1 \end{pmatrix}. \tag{5}$$

From this, the principal curvatures $\kappa_{1,2}$ and their corresponding directions $\boldsymbol{k_{1,2}}$ can be calculated. While the directions show again the orientation, the principal curvatures represent the respective curvature change, with $\kappa_i < 0$ indicating an increase in convexity, and $\kappa_i > 0$ an increase in concavity.

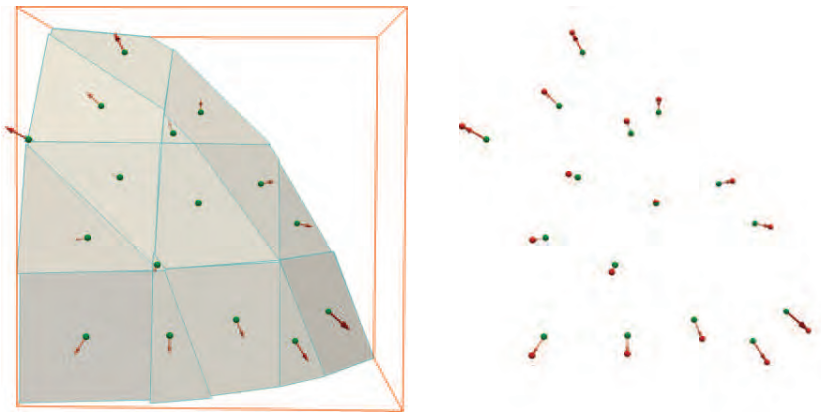

(a) (b)

Figure 1. Advection of interface points. In (a) one can see the original interface points and the modified simulation velocity on the PLIC interface. In (b), both the original and the advected points are shown.

Results and Discussion

In this section, we show the usefulness and applicability of our approach using two datasets. On the first one, a dataset from simulating two rain drops colliding in an off-center heads-on collision, we discuss interface stretching. On the other one from a simulation of two coalescing droplets, we demonstrate the application of interface bending. In both cases, we use colored tube glyphs, their orientation visualizing the direction of stretching and bending, respectively, and the color indicating their magnitude.

Colliding rain drops

In figure 2, the visualization of interface stretching is presented. For magnitudes larger than one and indicating stretching we use red, for magnitudes smaller than one and indicating contraction we use blue. For values close to one, the color is gray. As the values can lie between 0 and infinity, logarithmic scaling is applied. In figure 2 (a) and (b) you can see the larger and the smaller eigenvalues and eigenvectors, respectively. Looking at the tunnel-like structures, one can observe that there is an elongation along the tunnel and a contraction perpendicular to that. This indicates that the fluid is moving from the tunnels into the larger formations, while at the same time the tunnels are becoming thinner. From this, one can predict that the tunnels are going to collapse and the formations break up into droplets. This is supported by the topology of the subsequent time steps in figure 2 (c) and (d) which indeed show a droplet breakup.

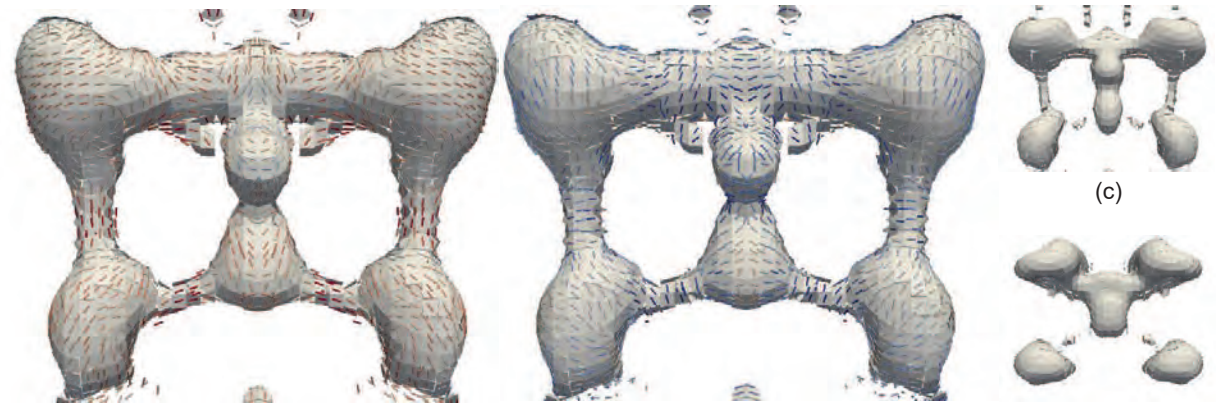

Figure 2. Interface stretching. In (a), the larger eigenvalues and corresponding eigenvectors are shown in red. In (b), analogously, the smaller values are visualized indicating contraction in blue. Subsequent time steps are depicted in (c) and (d).

Coalescing droplets

To show the usefulness of the visualization of interface bending, we apply it to a dataset which was generated in a simulation performed by the FS3D solver considering Marangoni convection in a work-in-progress implementation. The start configuration of the simulation consists of two droplets, one water droplet on the left and one ethanol droplet on the right, at the onset of coalescence. Due to the resulting gradient of the surface tension force, the Marangoni convection induces a force that acts along the surface. This leads to the coating of the left droplet with fluid of the right one. In figure 3, interface bending is visualized with red glyphs for an increase in concavity and blue glyphs for an increase in convexity. Gray glyphs indicate no change for values around zero. One can observe a capillary wave forming at the junction of the two coalescing droplets and moving along the surface to the left. This is an expected phenomenon. Here, our method helps in identifying this wave: in front of the wave we can see an increase in convexity and behind an increase in concavity. Thus, by only looking at a single time step, we can assess the movement of the wave.

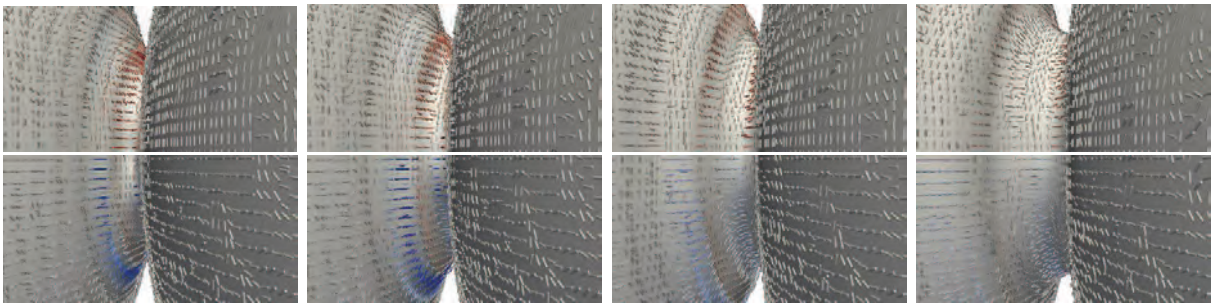

Figure 3. Interface bending. The time steps from (a) to (d) show an increase in concavity in the upper row and an increase in convexity in the bottom row. Because of symmetry, both rows show the same dataset mirrored on the x-axis.

References

[1] Eisenschmidt K., Ertl M., Gomaa H., Kieffer-Roth C., Meister C., Rauschenberger P., Reitzle M., Schlottke K., Weigand B., Direct numerical simulations for multiphase flows: An overview of the multiphase code fs3d, in: Applied Mathematics and Computation 272, Part 2 (2016), 508 – 517.

[2] Hirt C., Nichols B., Volume of fluid (VOF) method for the dynamics of free boundaries, in: Journal of Computational Physics 39, 1 (1981), 201–225.

[3] Karch G. K., Sadlo F., Rauschenberger P., Meister C., Eisenschmidt K., Weigand B., Ertl T., Visualization of Piecewise Linear Interface Calculation, in: Proceedings of IEEE Pacific Vis 2013 (2013), pp. 121–128.

[4] Obermaier H., Joy K. I., Derived Metric Tensors for Flow Surface Visualization, in: IEEE Transactions on Visualization and Computer Graphics 18, 12 (2012), 2149–2158.

[5] Popinet S., An Accurate Adaptive Solver for Surface-tension-driven Interfacial Flows, in: Journal of Computational Physics 228, 16 (2009), 5838–5866.

Gas-Kinetic Simulation of Microdroplet-Gas Interaction

W. Reschke* and S. Fasoulas
Institute of Space Systems, University of Stuttgart,
Pfaffenwaldring 29, 70569 Stuttgart, Germany
*Corresponding author: reschke@irs.uni-stuttgart.de

Introduction

Most numerical approaches to handle gas-fluid interactions are based on continuum methods. A main disadvantage is the necessity of continuum assumptions including local thermodynamic equilibrium or limitations to quasi-steady conditions.

Within this project the interaction between gas flows and liquid nano-scale droplets will be simulated using the Direct Simulation Monte Carlo (DSMC) method [1]. DSMC approximates the gas flow from a microscopic point of view and discrete simulation particles allow for a treatment of non-equilibrium effects. Consequently, a comparison between DSMC and existing analytical results will be of fundamental interest to analyse the effects of equilibrium assumptions and flow unsteadiness.

In this work the used methods and tools are presented. The used models are described and the first results are presented and discussed.

Direct Simulation Monte Carlo

The gas phase is modelled by approximatively solving the Boltzmann equation (1) with the DSMC method where t is the time, $\vec{v}$ the velocity, $\vec{x}$ the spatial position, F the external forces and m the species mass.

$$\left(\frac{\partial}{\partial t}+\vec{v}\cdot\nabla_{\vec{x}}+\frac{\vec{F}}{m}\cdot\nabla_{\vec{v}}\right)f(\vec{x},\vec{v},t)=\frac{\partial f}{\partial t}|_{Collision} \tag{1}$$

The focus is to statistically reconstruct the particle distribution function $f(\vec{x},\vec{v},t)$ with N discrete particles distributed in space with

$$f(\vec{x},\vec{v},t)=\sum_{p=1}^{N} w_p\cdot\delta\left(\vec{x}-\vec{x}_p(t)\right)\cdot\delta\left(\vec{v}-\vec{v}_p(t)\right) \tag{2}$$

Where $w_p=N_{real}/N_{sim}$ is the weighting factor of the simulated particles, δ the delta function, $\vec{x}_p(t)$ and $\vec{v}_p(t)$ the time dependant particle position and particle velocity respectively. In contrast to Molecular Dynamics simulations the deterministic description of each microscopic particle state and interaction is not of interest. Movement and collision are decoupled in every simulation time step and collisions are solved statistically using phenomenological probability models and comparison to random numbers. Macroscopic values like number density and heat fluxes are then calculated from moments of the resulting sampled particle distribution, E.g., particle number density $n=\int f\,dv$ and heat flux $\dot{q}_i=\frac{m}{2}\int c^2\cdot c_i\cdot f\,dc$ with the thermal velocity $c_i=v_i-u_i$.

Plasma Flow Solver PICLas

PICLas [2], a highly flexible tool for simulation of rarefied 3D plasma flows, is used for the shown simulations. PICLas is cooperatively developed by the Institute of Aerodynamics and Gasdynamics (IAG) and the Institute of Space Systems (IRS) at the University of Stuttgart. Figure 1 illustrates a representative simulation time step in PICLas, where the Particle in Cell (PIC) and DSMC method are coupled. Particle in Cell (PIC) calculates the interpolation of electromagnetic forces and DSMC the intermolecular collisions. Additionally other continuum based particle methods are in development to approximately solve the total Boltzmann equation such as Fokker-Planck (FP), Bhatnagar-Gross-Krook (BGK) and Low-Difusion (LD).

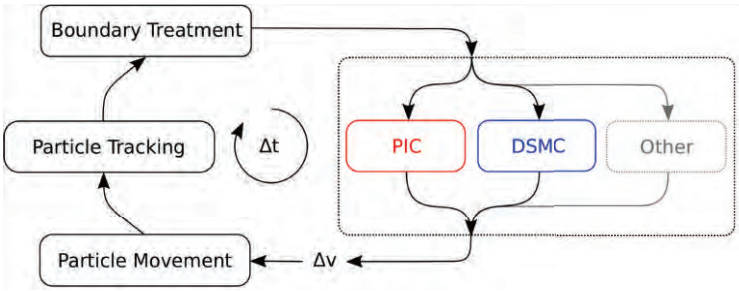

Figure 1. Scheme showing one simulation time step (Δt) of PICLas with the loadable solver modules

Liquid boundary

For the simulation of liquid boundaries a simple evaporation / condensation model is implemented. To calculate the number of evaporating particles ΔN per time step Δt from a liquid surface area A_{liq} the Hertz-Knudsen equation (3) is used. The saturation pressure p_s is defined by the Antoine equation (4) for a given liquid temperature T_{liq} with A, B and C being species specific parameters. Energies and velocities of evaporating particles are sampled from a Maxwell distribution at liquid temperature. For condensation every liquid species particle colliding with the liquid surface is removed and gas species particles are reflected applying diffuse scattering. This represents a condensation coefficient $\sigma_c = 1$. The described implementation is tested by simulating a 3D domain with periodicity in x and y direction representing a quasi-1D test case of H_2O evaporation into pure O_2 gas as shown in figure 2. Furthermore, figure 3 shows the velocity distribution sampled in the vicinity of the liquid boundary for both species.

$$\frac{\Delta N}{\Delta t} = \sigma_c A_{liq} \frac{p_s}{\left(2\pi m k_B T_{liq}\right)^{1/2}} \tag{3}$$

$$\log_{10}(p_s) = A - \frac{B}{C - T_{liq}} \tag{4}$$

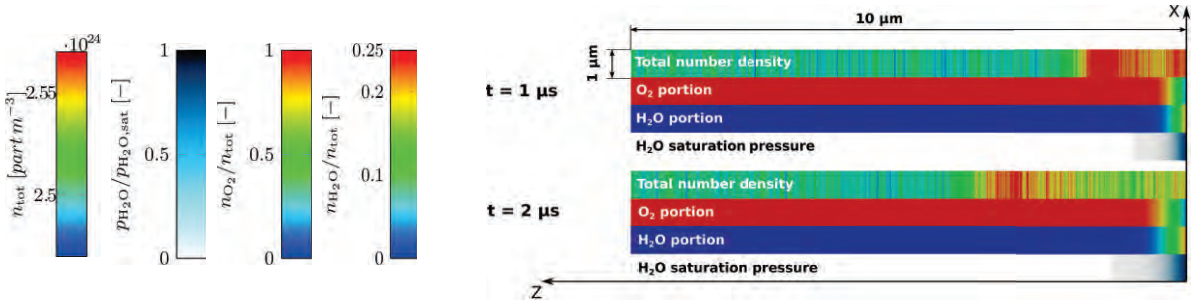

Figure 2. Simulation of liquid evaporation with liquid boundary at z = 0 µm. Domain is symmetric in x and y direction with an open boundary at z = 10 µm. Initial values: p_∞ = 10 000 Pa, $T_{O_2} = T_{H_2O}$ = 293 K.

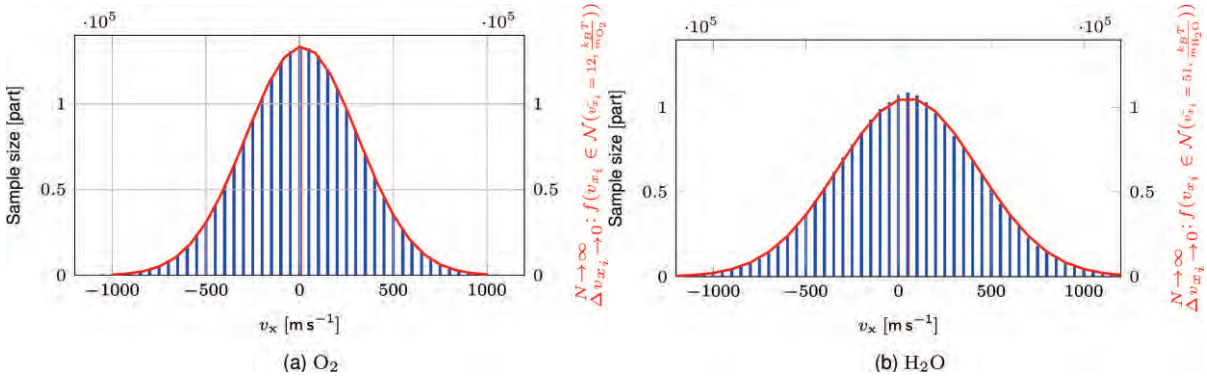

Figure 3. Plots showing comparison of sampled (blue bars) particle velocity distribution (z-component) to calculated (red line) distribution for infinite particle numbers at liquid boundary within Δz = 1µm.

Simulation of evaporating droplet

To investigate influences of microscopic effects of droplet evaporation a 3D simulation setup of a flow around an evaporating droplet was constructed. Due to the physical constraints of DSMC for this density region, the number of simulated particles is quite high. To reduce computational effort the computational domain was reduced to a $\frac{1}{4}$ sphere. Table 1 shows chosen parameters for the simulation and figure 4 shows a 2D slice showing a density result.

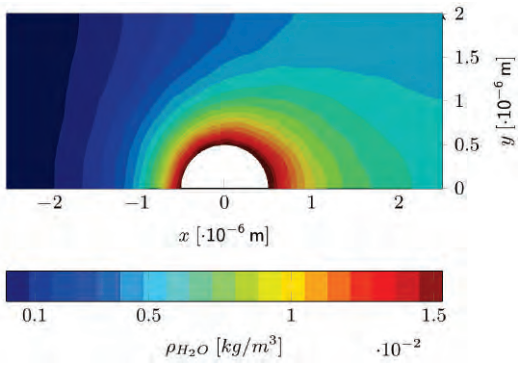

Figure 4. Vapor density around an evaporating H_2O droplet in a O_2 flow for given parameters at t sample simulated with a $\frac{1}{4}$ sphere 3D domain.

Table 1. Parameters used for simulation of droplet evaporation. 3D quarter sphere chosen as computational domain.

Parameter		Dimension	Value
v_x	Flow velocity	[m s^{-1}]	10
T_{O_2}	Gas temperature	[K]	293
$T_{droplet}$	Droplet temperature	[K]	293
ρ_{O_2}	Gas density	[kg m^{-3}]	1.165
d	Droplet diameter	[µm]	1
Kn_d	Knudsen number (reference length $L = d$)	[-]	0.05
t_{sample}	Sampling time interval	[$\cdot 10^{-6}$ s]	1
Δt	Simulation time step	[$\cdot 10^{-11}$ s]	1

Influences of droplet size on drag coefficient

Simulations using droplet sizes from table 2 were performed for a solid and evaporating sphere using the previous setup of a $\frac{1}{4}$ sphere. Additionally, the drag forces F_d on the sphere in x direction were sampled.

Figure 5 shows the results of the drag coefficient calculated from respective simulation results with equation (6). Those results are compared to an analytic equation (5) for the drag coefficient at low Reynolds numbers [3]. The results match for the higher Reynolds number case. However, for the lower Reynolds number case the simulated drag coefficient seems to be underpredicted by the simulation. The reason might be continuum breakdown effects indicated by higher Knudsen numbers of 0.05 for this case as shown in table 2. However, to further investigate this behaviour additional simulations have to be conducted.

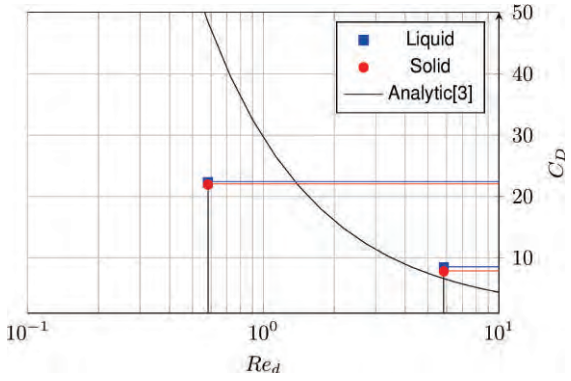

Figure 5. Drag coefficient for evaporating and solid sphere simulated with PICLas and analytic values for respective Reynolds and Knudsen number values given in table 2.

$$C_d = C_0\left[1+\left(\frac{\delta_0}{Re_d}\right)^{1/2}\right]^2 \qquad C_0\delta_0=24,\ \delta_0=9.06 \tag{5}$$

$$C_d \overset{\text{sim}}{=} \frac{2F_d}{\rho_\infty u_\infty^2 A_{ref}} \qquad A_{ref}=\pi\left(\frac{d}{2}\right)^2 \tag{6}$$

Table 2. Resulting Reynolds and Knudsen numbers for respective diameters of simulated droplets.

Parameter		Dimension	Set 1	Set 2
d	Droplet diameter	[µm]	1	10
Re_d	Reynolds number (reference length $L = d$)	[-]	0.5825	5.825
Kn_d	Knudsen number (reference length $L = d$)	[-]	0.05	0.005

Nomenclature

- f particle distribution function [-]
- x position / distance [m]
- t time [s]
- F force [N]
- d diameter [m]
- A surface area[m²]
- T temperature [K]
- m mass [kg]
- w_p weighting factor of particle p [-]
- N_i particle number of i [part]
- $\dot{q}$ heat flux [W m⁻²]
- c thermal velocity [m s⁻¹]
- v total velocity [m s⁻¹]
- u drift velocity [m s⁻¹]
- ρ density [kg m⁻³]
- p pressure [Pa]
- Re_d Reynolds number for reference length d [-]
- Kn_d Knudsen number for reference length d [-]
- σ_c condensation coefficient [-]
- k_B Boltzmann constant [J K⁻¹]

References

[1] Bird, G. A., Molecular Gas Dynamics and Direct Simulation of Gas Flows, Oxford Science Publications 42, 1994.
[2] Munz, C.-D. et al., Coupled particle-in-cell and direct simulation monte carlo method for simulating reactive plasma flows, Comptes Rendus Mécanique 342 (10) 662–670 (2014).
[3] F. F. Abraham, Functional dependence of drag coefficient of a sphere on reynolds number, The Physics of Fluids 13 (8) 2194–2195 (1970).

Effect of local surface curvature on heating and evaporation of deformed droplets

S. Tonini*, G.E. Cossali
Università di Bergamo, Via Marconi 6, 21044, Dalmine (BG) Italy
*Corresponding author: simona.tonini@unibg.it

Introduction

Drop evaporation in gaseous flows is of fundamental importance for a wide range of engineering applications (automotive, aeronautic, fire suppression, painting, medical aerosol, meteorology, etc.). This process involves simultaneous heat and mass transfer and a wide literature is available on the modelling of the complex physical phenomena involved (see [1] for a recent review on the subject). Liquid droplets interacting with the carrier gas phase are subject to deformation, due to the interaction of surface tension and fluid-dynamic stresses on the drop surface. While surface tension force induces a spherical shape, fluid-dynamic forces are the primary sources of drop deformation. This is clearly evident in case of liquid drop with Weber number above 2, typical of spray combustion applications, which are appreciably non-spherical. The simplifying hypothesis of drop sphericity, which is the basis of all the models currently implemented in CFD codes for spray analysis [2], can only be considered as an idealisation. Recently [3], this hypothesis was removed, developing analytical solutions to the problem of heating and evaporation from spheroidal and triaxial ellipsoidal drops. The present investigation aims to extend the previous work, proposing a model based on the analytical solution of the species and energy conservation equations within the gas phase surrounding a single-component deformed drop and to analyse the effect of local curvature on the local evaporation and heat fluxes for a wider range of drop shapes.

Mathematical modelling

The species conservation equations for a single component drop evaporating under quasi-steady conditions are:

$$\nabla_j N_j^{(p)} = 0 \quad p = (0,1) \tag{1}$$

where:

$$N_j^{(p)} = N_j^{(T)} y^{(p)} - cD_{10} \nabla_j y^{(p)} \tag{2}$$

are the molar fluxes, p=1 stands for the evaporating species while p=0 for the non-evaporating one, $N_j^{(T)} = N_j^{(0)} + N_j^{(1)}$ and $y^{(p)}$ is the molar fraction of the species p and c is the molar gas density that, under the assumption of ideal gas mixture, can be calculated as:

$$c = \frac{P_T}{RT} \tag{3}$$

To notice that the usual way to approach this problem is by using a mass form of the species conservation equations (see [2]), but it can be shown (see [4]) that for single component drops the two approaches are equivalent and the mass flux can be obtained by $n_j^{(p)} = N_j^{(p)} Mm^{(p)}$.

Assuming that the non-evaporating component p=0 does not diffuse into the liquid and considering that, for the quasi-steady approach, the drop surface is assumed to be still, the molar flux of this species is nil everywhere and:

$$N_j^{(1)} = N_j^T = cD_{10} \nabla_j H \tag{4}$$

where $H = \ln\left(y^{(0)}\right)$. Summation of equations (1) yields the mass conservation equation:

$$\nabla_j \left(\rho U_j\right) = 0 \tag{5}$$

and, since under the mentioned assumptions: $\rho U_j = n_j^{(T)} = n_j^{(1)} = Mm^{(1)} N_j^{(T)}$, equations (4) and (5) yield:

$$\nabla^2 H = 0 \tag{6}$$

The steady energy equation, assuming constancy of the thermo-physical properties, using equations (5) and neglecting some minor terms (see [5] for a more detailed discussion), becomes:

$$\nabla_j H \nabla_j T - Le_M \nabla^2 T = 0 \tag{7}$$

where the modified Lewis number is defined as: $Le_M = k \Big/ \left(Mm^{(1)} c D_{10} c_p \right)$.

1.1. Coordinate systems and solutions

Equations (6) and (7) must be solved imposing boundary conditions at the drop surface and at infinity. For the present analysis the condition on the drop surface and at infinity will be assumed of Dirichlet type and uniform, i.e.:

$$\begin{aligned} &T\left(\zeta = \zeta_0\right) = T_s; \;\; T\left(\zeta = \infty\right) = T_\infty \\ &y^{(1)}\left(\zeta = \zeta_0\right) = y_{sat}\left(T_s\right); \;\; y^{(1)}\left(\zeta = \infty\right) = y_\infty^{(1)} \end{aligned} \tag{8}$$

The problem set by equations (6), (7) and (8) is clearly independent of the choice of the coordinate system and holds for any shape of the evaporating drop. However, proper choices of coordinate systems allow simpler solutions for a variety of drop shape. In the present work five curvilinear orthogonal coordinate systems are considered: spherical, prolate and oblate spheroidal, inverse prolate and oblate rotation cyclide, which are defined as follows [6]:

$$\begin{aligned} x &= a \frac{\sqrt{\zeta^2 + \alpha}}{\Theta} \sqrt{1 - \eta^2} \cos\varphi = \Phi\left(\zeta, \eta\right) \cos\varphi \\ y &= a \frac{\sqrt{\zeta^2 + \alpha}}{\Theta} \sqrt{1 - \eta^2} \sin\varphi = \Phi\left(\zeta, \eta\right) \sin\varphi \\ z &= a \frac{\zeta \eta}{\Theta} = \Psi\left(\zeta, \eta\right) \end{aligned} \tag{9}$$

where the values of α and Θ are given in table 1 for the selected coordinate systems.

Table 1. Parameters of the selected coordinate systems [6].

Shape	α	Θ		$J_n(\zeta)$
Sphere	0	1	$0 \le \zeta < 1$	$\zeta^{(n+1)}$
Oblate	+1	1	$0 \le \zeta < \infty$	$Q_n(i\zeta)$
Prolate	-1	1	$1 \le \zeta < \infty$	$Q_n(\zeta)$
Inverse oblate	+1	$\zeta^2 + \alpha(1-\eta^2)$	$0 \le \zeta < \infty$	$P_n(i\zeta)$
Inverse prolate	-1	$\zeta^2 + \alpha(1-\eta^2)$	$1 \le \zeta < \infty$	$Q_n(\zeta)$

The drop surface is always defined by the equation $\zeta = \zeta_0$, although it must be noticed that the coordinates η and ζ have different definitions in the different coordinate systems, as an example, $\zeta = R_0/r$ and $\eta = \cos\theta$ for the spherical coordinates, where R_0 is the radius of the spherical particle defined by the equation $\zeta = 1$ (i.e. $\zeta_0 = 1$). To notice that for a general shaped drop, an equivalent radius can be always defined as: $R_0 = \sqrt[3]{3V/4\pi}$, where V is the drop volume. In the following, the drop surface will be always defined to maintain the same equivalent radius to allow a direct comparison of the evaporation characteristics of different shaped drops having the same volume.
Spheroidal drops appear when drop oscillation is considered. The oscillation mode n=2, which is the long lasting one since viscous damping is more intense for the higher modes, it is in fact characterized by an oblate-prolate shape alternation. Drops of different shapes can be found in other kind of process, for example the head on impact of two drops at low velocity shows shapes that can be well approximated by rotational cyclides, as reported for example, in [7]. These shapes can be easily approximated in inverse oblate and inverse prolate coordinates [6].
The solutions of equations (6) and (7) assume the following forms:

$$H = \Theta^{1/2} g_0 \frac{J_0\left(\zeta\right)}{J_0\left(\zeta_0\right)} + \Theta^{1/2} \sum_{n=1}^{\infty} g_n \frac{J_n\left(\zeta\right)}{J_n\left(\zeta_0\right)} P_n\left(\eta\right) + H_\infty \tag{10}$$

$$T = \frac{e^{\left(H_s - H_\infty\right)/Le_M} T_\infty - T_s}{e^{\left(H_s - H_\infty\right)/Le_M} - 1} + \frac{T_s - T_\infty}{e^{\left(H_s - H_\infty\right)/Le_M} - 1} e^{\left(H - H_\infty\right)/Le_M} \tag{11}$$

where the function J_n are defined in table 1 for the different coordinate systems.
The normal component of the sensible heat flux at drop surface is:

$$\varphi_\zeta = -k \frac{1}{h_\zeta} \left(\frac{\partial T}{\partial \zeta} \right)_{\zeta_0} \tag{12}$$

where h_ζ is the proper scale factor.

2. Mass fluxes and surface curvatures

The vapour fluxes at drop surface can be found, from their definitions (4), once the function H is calculated. The available results on evaporation from non-spherical drops have considered that a direct relation between flux and surface curvature should exist. For example [8] assumed a proportionality between the vapour fluxes at drop surface and the mean curvature. Recently [3], it has been proven that for spheroidal drops there exist a perfect proportionality of the vapour flux with the fourth root of the Gaussian curvature. However, for a general drop shape the one-to-one relationship between vapour flux and local curvature has been only conjectured. The results of this investigation prove that such a conjecture cannot be supported by theory.
The principal curvatures of a generic rotational surface defined parametrically as:

$$x = \Lambda(\zeta_0, \eta) cos\, \varphi; \;\; y = \Lambda(\zeta_0, \eta) sin\, \varphi; \;\; z = \Psi(\zeta_0, \eta) \tag{13}$$

can be calculated as:

$$k_1 = \frac{-sign(\Lambda)\left[\Lambda_{\eta\eta}\Psi_\eta - \Lambda_\eta \Psi_{\eta\eta}\right]}{\left(\Lambda_\eta^2 + \Psi_\eta^2\right)^{3/2}}; \quad k_2 = \frac{\Psi_\eta}{|\Lambda|\left(\Lambda_\eta^2 + \Psi_\eta^2\right)^{1/2}} \tag{14}$$

and the corresponding Gaussian and mean curvatures are defined as:

$$\bar{K}_G = k_1 k_2; \quad \bar{C}_m = k_1 + k_2 \tag{15}$$

respectively. To generalize the analysis, considering that the drop size is always defined by the equivalent radius, the non-dimensional Gauss and mean curvature are defined as:

$$K_G = R_0^2 \bar{K}_G; \quad C_m = R_0 \bar{C}_m \tag{16}$$

In the next session the relationship between these curvatures and the corresponding non-dimensional vapour fluxes:

$$n_{\zeta,ad} = \frac{n_\zeta^{(1)} R_0}{\rho D_{10}\left(H_\infty - H_s\right)} \tag{17}$$

which are independent of the species properties, will be analysed.

3. Curvature map and vapour fluxes

From equations (16) the Gauss and mean non-dimensional curvatures can be calculated for the above reported drop shapes. Figure 1(a) shows a sample of the contour distribution of the two non-dimensional curvatures for two rotational cyclides (inverse oblate and inverse prolate), while figure 1(b) shows the corresponding 2D map for all the selected drop shapes. Different shapes are characterised by different non-dimensional local curvatures as a function of shape (i.e. ζ_0) and position on the surface (i.e. η), and the map shows that there exists a relatively narrow region where four drop shapes, namely oblate and prolate spheroids, inverse prolate and oblate cyclides, have the same Gauss and mean curvature in some positions over the drop surface.
Since the curvature characteristics of a surface are completely defined by these two curvatures, the existence of a direct relationship between surface curvature and vapour flux would imply that the four drops have the same vapour fluxes at the locations where the curvatures are the same.
Figure 2 reports the map of the non-dimensional vapour flux for the four surfaces, calculated into the above mentioned overlapping region. The shape of the map for the oblate/prolate spheroids confirms the known direct dependence to the fourth root of the Gaussian curvature, a results that was established not only for spheroidal shapes but also for triaxial ellipsoids (see [3]). However, the map for the other two drop shapes shows a quite different dependence.
This proves that the vapour flux from a deformed drop cannot in general be only a function of local curvature. This does not disprove the above mentioned results for ellipsoidal drops, in the sense that it is possible, as above stated, that for a certain class of shapes a relationship exists, but this cannot be considered a general rule.

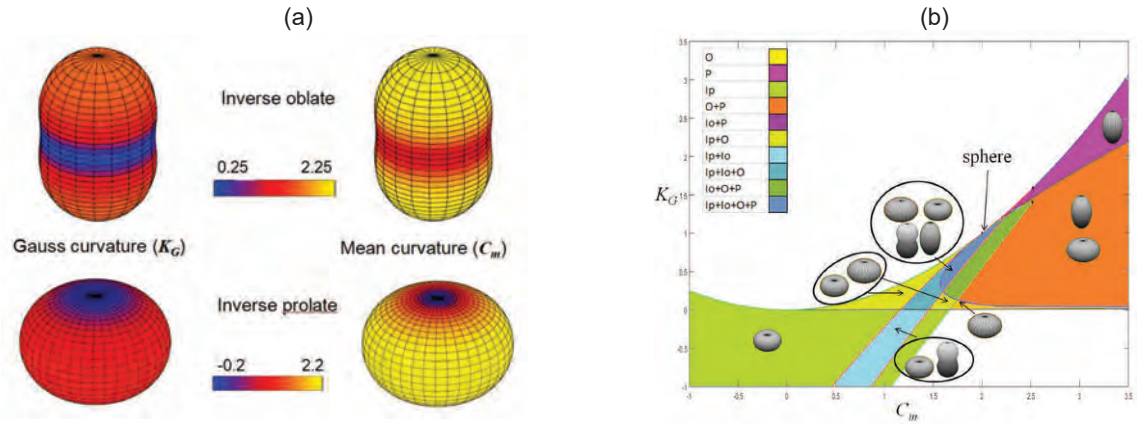

Figure 1. (a) Samples of contour distributions of Gauss and mean curvatures for two rotational cyclides; (b) map of Gauss and mean surface curvatures for different drop shapes.

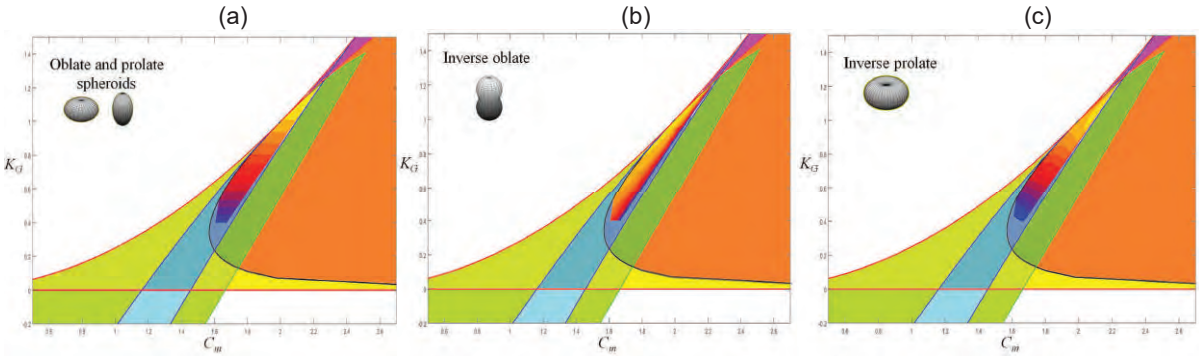

Figure 2. Map of the non-dimensional vapour fluxes for (a) the oblate and prolate spheroids, (b) the inverse oblate and (c) inverse prolate cyclides, calculated into the overlapping region.

4. Conclusions

An analytical model has been developed to calculate the drop evaporation accounting for the effect of drop deformation. The model is applied to five drop shapes, namely the sphere, the oblate and prolate spheroids, and two rotation cyclides (inverse oblate and prolate spheroids). Some common simplifying hypotheses, like steady-state, constant gas properties, single component drop, are assumed. The conservation equations are solved in each natural coordinate system, depending on the drop shape, imposing uniform Dirichelet boundary conditions at the drop surface and at free-stream. The local vapour flux over the drop surface is calculated and correlated, where possible, with the local curvature. It is confirmed that for spherical and spheroidal drops the local vapour flux is proportional to the fourth root of the surface Gaussian curvature, and this result can be also extended to triaxial ellipsoidal drops, while for inverse spheroidal drops the local fluxes depend both on the local curvature and the whole drop shape.

This proves that the local vapour flux from a deformed drop cannot in general be only a function of local curvature, although this can happen for certain classes of drop shapes (like for ellipsoidal drops).

References

[1] Sazhin, S.S., Droplets and Sprays, Springer, 2014.
[2] Abramzon, B., Sirignano, W.A., International Journal of Heat and Mass Transfer 32(9): 1605-1618, (1989).
[3] Tonini, S., Cossali, G.E., International Journal of Heat and Mass Transfer 97: 301-307 (2016).
[4] Tonini, S., Cossali, G.E., International Journal of Heat and Mass Transfer 92: 184-189 (2016).
[5] Slattery, J.C., Momentum, Energy and Mass Transfer in Continua, Edition R. Krieger Publ., New York, 1981.
[6] Moon, P., Spencer, D.E., Field Theory Handbook, 2nd ed., Springer-Verlag, Berlin, 1988.
[7] Quin, J., Law, C.K., Journal of Fluid Mechanics 331: 59 (1997).
[8] Mashayek, F., International Journal of Heat and Mass Transfer 44(8): 1517-1526 (2001).

Modelling of heat and mass transfer from spheroidal drops with general non-uniform Dirichlet boundary conditions

G. Varma Raja Kochanattu*, G.E. Cossali, S. Tonini
Department of Engineering and Applied Sciences, University of Bergamo, Italy
*Corresponding author: g.varmarajakochan@studenti.unibg.it

INTRODUCTION

The process of liquid drop evaporation has wide range of applicative fields like spray combustion, spray painting, fire control, medical applications, etc. [1]. The modelling of evaporation of liquid droplets in gaseous environment has been extensively studied since Maxwell proposed the first model [2]. The classical approach for modelling this problem includes some assumptions like drop sphericity, constant gas density and properties, ignoring the Dufour and Soret effects, etc. 1-D analytical approach for modelling evaporation of deformed droplet was developed in [3]. The effect of non-uniform drop surface temperature on the heating and evaporation of spheroidal droplet was initially studied in [4], which proposes an analytical solution for the steady-state species conservation equations and a numerical solution for the energy equation for spheroidal drops in gaseous mixture, imposing non-uniform drop temperature profiles. The results suggested that the correlation of the vapor flux as function of the Gaussian curvature [3] holds only with uniform drop temperature case. The application of the model to the study of the transient drop heating and evaporation was first proposed in [5], enlightening the contribution of drop temperature non-uniformity on heat and mass transport within the liquid phase. The present work extends the model to general non-uniform Dirichlet boundary conditions, including the variation of the drop temperature along the azimuthal angle, proposing a fully 3-D analytical solution of the species conservation equation for spheroidal drops. The next sections describe the mathematical modelling and the analytical solution proposed, followed by same samples of the results obtained applying the model to spherical and spheroidal geometries under different operating conditions. Extension to the solution of the energy equation will be part of a future work.

MATHEMATICAL MODELLING

CONSERVATION EQUATIONS

The steady-state species conservation equations can be written in the general form for a binary system as:

$$\nabla_j n_j^{(\alpha)} = 0 \tag{1}$$

where the mass flux $n_j^{(\alpha)}$ (with α = (1, 2) for gas and vapour, respectively) assumes the form:

$$n_j^{(\alpha)} = \rho U_j \chi^{(\alpha)} - \rho D_v \chi^{(\alpha)} \tag{2}$$

where $\chi^{(\alpha)} = \frac{\rho^{(\alpha)}}{\rho}$ is the mass fraction, D_v is the mass diffusivity and U_j is the Stefan flow velocity. Using equations (1) and (2) and accounting for $\chi^{(1)} + \chi^{(2)} = 1$ yields the usual mass conservation equation $\nabla_j \left(\rho U_j\right) = 0$. Assuming still drop surface and neglecting gas diffusion within the liquid phase yields nil gas flux everywhere. Defining $G = \ln\left(1 - \chi^{(2)}\right)$, the equation (2) becomes:

$$U_j = D_v \nabla_j G \tag{3}$$

and under further assumption of constant diffusion coefficient, the Laplace equation for the variable G is obtained:

$$\nabla^2 G = 0 \tag{4}$$

The steady-state energy equation, neglecting minor terms like dissipation by viscous stress, and assuming constant transport properties within the gas mixture (refer to [6] for the complete expression), can be written as:

$$U_j \nabla_j T = \frac{k}{\rho c_p} \nabla^2 T \tag{5}$$

Using equation (3), equation (5) becomes:

$$\frac{\rho c_p D_v}{k} \nabla_j G \nabla_j T - \nabla^2 T = 0 \tag{6}$$

The present model proposes an analytical solution of equation (4) for spherical and spheroidal drops, imposing non-uniform Dirichlet boundary conditions at the drop surface.

SOLUTION IN SPHERICAL AND SPHEROIDAL COORDINATE SYSTEMS

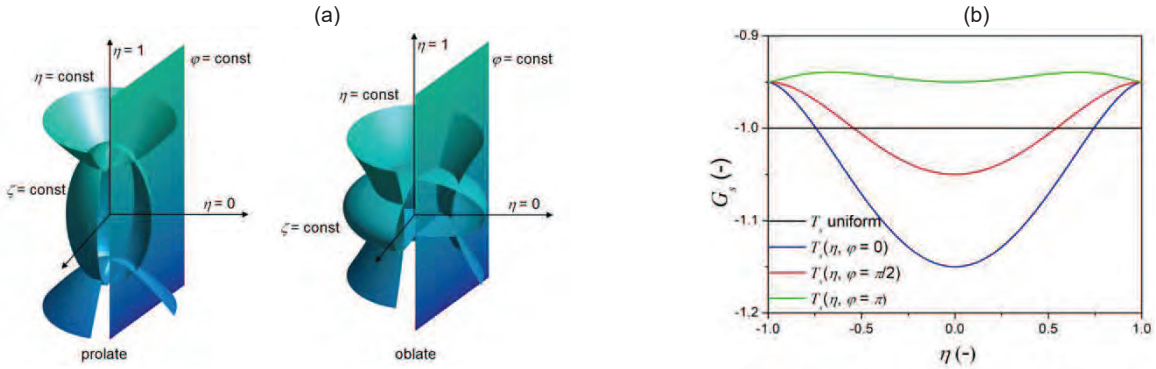

Figure 1: (a) Spheroidal coordinate system configuration: oblate (left), prolate (right). (b) η-profiles of the variable G at the drop surface for the different test-cases investigated.

The Laplace equation (4) was solved in spherical and spheroidal oblate and prolate coordinate systems, which definitions are given by the equations (7) (refer to figure 1a for a schematic configuration) [7]:

$$x = a\sqrt{\zeta^2+\alpha}\sqrt{1-\eta^2}\cos\phi;\;\; y = a\sqrt{\zeta^2+\alpha}\sqrt{1-\eta^2}\sin\phi;\;\; z = a\zeta\eta \tag{7}$$

where α is equal to 0, -1, +1 for the spherical, prolate spheroidal and oblate spheroidal geometries, respectively. The drop surface is always defined by the equation $\zeta = \zeta_0$, although it must be noticed that the coordinates η and ζ have different definitions in the different coordinate systems, as an example, $\zeta = R_0/r$ and $\eta = \cos\theta$ for the spherical coordinates, where R_0 is the radius of the spherical particle defined by the equation $\zeta = 1$ (i.e. $\zeta_0 = 1$). To notice that for a general shaped drop, an equivalent radius can be always defined as: $R_0 = \sqrt[3]{3V/4\pi}$, where V is the drop volume. In the following, the drop size will be always defined to maintain the same equivalent radius allowing a direct comparison of the evaporation characteristics of different shaped drops having the same volume.

The scale parameter in equations (7) is defined as $a = R_0\dfrac{\left|1-\varepsilon^2\right|^{1/2}}{\varepsilon^{1/3}}$, where $\varepsilon = \dfrac{a_z}{a_r}$ is the deformation parameter defined with respect to the axial (a_z) and radial (a_r) semi-axis. The analytical solution for the Laplace equation (4) assumes the following form [7]:

$$G - G_\infty = \sum_{n,m} g_{n,m} W_n(\zeta) P_n^m(\eta)\cos(m\varphi) \tag{8}$$

where $P_n^m(\eta)$ are the associated Legendre functions of the first kind [8] and the functions $W_n(\zeta)$ depend on the coordinate system:

$$W_n(\zeta) = \frac{\zeta^{n+1}(\zeta)}{\zeta_0^{n+1}(\zeta_0)}\;\; sphere;\;\; W_n(\zeta) = \frac{Q_n^m(\zeta)}{Q_n^m(\zeta_0)}\;\; prolate;\;\; W_n(\zeta) = \frac{Q_n^m(i\zeta)}{Q_n^m(i\zeta_0)}\;\; oblate \tag{9}$$

where Q_n^m are the associated Legendre functions of the second kind [8].

The coefficients g_{nm} are calculated imposing the boundary conditions at the drop surface. The values of the drop temperature on the drop surface are imposed and the corresponding values of the variable G are calculated assuming that the vapour is saturated in the region close to the liquid/drop interface. To notice that the function G on the surface is monotonically decreasing with surface temperature. The selected profile of the temperature and the function G at the drop surface should satisfy some constrains: the symmetry conditions at the pole $\eta = 1$ yields $\partial G/\partial\eta = 0$; the symmetry at the equator yields $G_s(\eta,\varphi) = G_s(-\eta,\varphi)$. Furthermore the knowledge of the minimum and maximum values of the temperature profile, and then of the function G on the surface, assumed monotonic along the variable η, assures the closure of the problem. Figure 1(b) shows a sample of the distribution of G as function of the coordinate η along the drop surface, for three values of the azimuthal angle φ.

Once the solution of the species conservation equation is obtained, the vapour fluxes can be calculated along each coordinate directions:

$$n_{v,j} = \rho D_v \nabla_j G \quad with\; j = (\zeta,\eta,\varphi) \tag{12}$$

where the gradients of the variable G assume the form:

$$\nabla_\zeta G = \frac{1}{h_\zeta}\sum_{n,m} g_{n,m} W_n'(\zeta) P_n^m(\eta)\cos(m\varphi) \tag{13a}$$

$$\nabla_\eta G = \frac{1}{h_\eta}\sum_{n,m} g_{n,m} W_n(\zeta) P_n^{m'}(\eta)\cos(m\varphi) \tag{13b}$$

$$\nabla_\varphi G = -\frac{1}{h_\varphi}\sum_{n,m} m g_{n,m} W_n(\zeta) P_n^m(\eta)\sin(m\varphi) \tag{13c}$$

being $W_n^{'}$ the derivatives with respect to ζ *and* $P_n^{m'}$ the derivative with respect to η.

RESULTS AND DISCUSSION

The model has been applied to calculate the effect of different boundary conditions at the drop surface on the vapour flux distribution for spherical and spheroidal drops. Three different boundary conditions have been investigated, namely a uniform distribution of the surface temperature, a distribution only function of the variable η and a distribution function both of the variable η and the azimuthal angle φ. The three distributions have been applied to three drop shapes having the same volume: a spherical drop, a spheroidal prolate drop with ε = 1.5 and a spheroidal oblate drop with ε = 0.5. Figure 1(b) shows the corresponding profiles of the variable $G = \ln\left(1-\chi^{(2)}\right)$, along the drop surface as function of the η-coordinate. The test-case with temperature and G only function of the variable η corresponds to the profile with $G_s(\eta, \varphi = \pi/2)$, while for the test case with the temperature and G function of both coordinates η and φ, three profiles have been plotted as a sample, corresponding to φ=0, π/2 and π. Figure 2 shows the contour distribution of the ζ-component of the non-dimensional vapour flux defined as $\tilde{n}_{v,\zeta} = \dfrac{n_{v,\zeta} R_0}{\rho D_v (G_\infty - G_s)}$ at the drop surface imposing uniform drop temperature for the two spheroidal drops, while the arrows represent the flux vectors. The graphs shows that the flux is depending on the drop curvature, and for the particular case with uniform temperature conditions at the drop surface the flux results to be proportional to the fourth root of the drop Gaussian curvature, as found in [3]. This is confirmed in figure 3(a), which plots the profile along the η-coordinate of the non-dimensional flux for the spherical and two spheroidal drop shapes imposing the uniform temperature distribution at the drop surface. The corresponding profiles obtained imposing a temperature distribution only function of the η-coordinate (red profile of figure 1b) are reported in figure 3(b). The imposed temperature has a peak at the drop equator (minimum of G_s) and a minimum at the poles (maximum of G_s). The vapour flux for the oblate drop reflects the imposed boundary conditions, with the maximum value reached at the drop equator and minimum values at the drop poles. For spherical and prolate drops the minimum value of the non-dimensional vapour flux is not reached at the poles and this is more evident in the case of prolate drop where the curvature is higher at the drop poles.

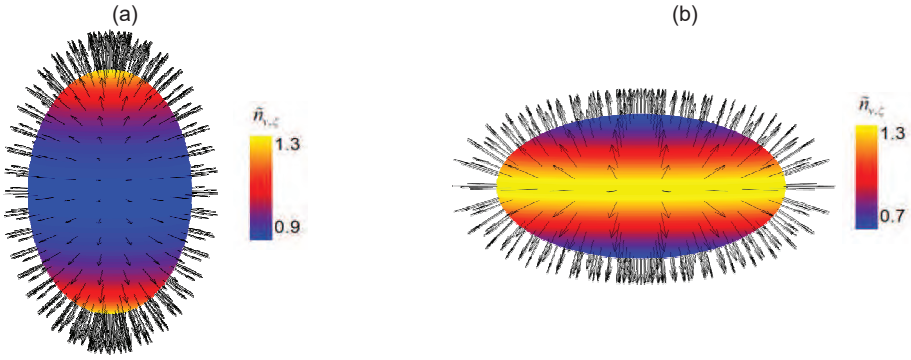

Figure 2: Non-dimensional vapour flux distribution at the drop surface for (a) prolate (ε = 1.5) and (b) oblate (ε = 0.5) drop with uniform temperature distribution as boundary conditions.

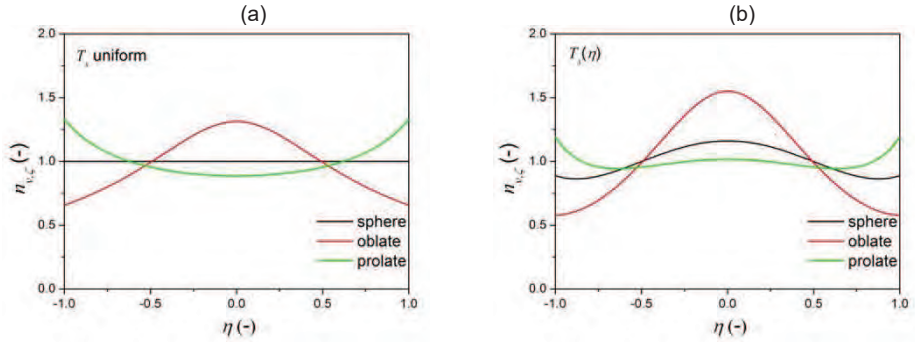

Figure 3: Non-dimensional vapour flux profiles along η-coordinate for spherical, prolate (ε = 1.5) and oblate (ε = 0.5) drops with (a) uniform temperature distribution and (b) temperature distribution function of η.

The effect of more general temperature distribution on the non-dimensional vapour flux distribution is shown in figure 4 for the three drop shapes. The corresponding profiles of the variable G_s as function of the h-coordinate along three azymuthal angles are reported in figure 1(b). The results suggest that the complexity of the temperature distribution reflects to the disuniformity of the vapour fluxes, and this is particularly evident for the

oblate drop, as confirmed by the distribution of the non-dimensional vapour flux as function of η-coordinate reported in figure 5 for all the three selected drop shapes.
This evidences the importance of accounting for non-uniform temperature distribution when modeling deformed drop evaporating in stagnant air. The model may be extended to include the solution of the energy equation to predict the combined effect of heat and mass transport within the gas mixture for spherical and spheroidal drops with non-uniform boundary conditions at the drop surface. This represents the main target for future investigation.

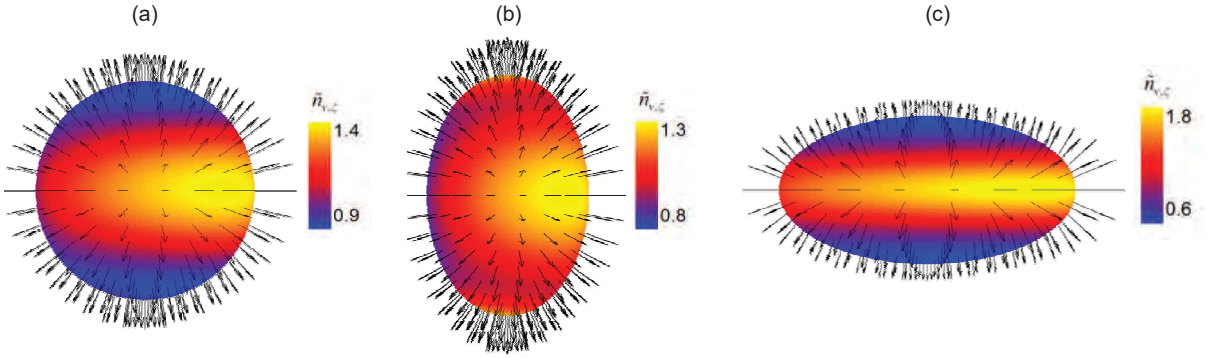

Figure 4: Non-dimensional vapour flux distribution at the drop surface for (a) sphere, (b) prolate (ε = 1.5) and (c) oblate (ε = 0.5) drop with non-uniform temperature distribution as boundary conditions.

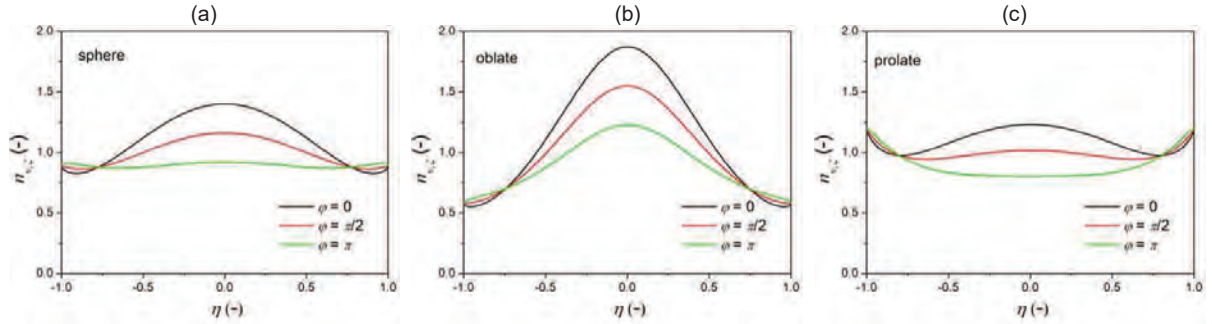

Figure 5: Non-dimensional vapour flux profiles along η-coordinate for three azymuthal angles φ, for (a) sphere, (b) prolate (ε = 1.5) and (c) oblate (ε = 0.5) drops with non-uniform temperature distribution as boundary conditions.

CONCLUSION AND NEXT STEP IN RESEARCH

The steady-state analytical solution of the species conservation equations has been analysed for spherical and spheroidal drops evaporating in stagnant air by accounting for the effect of non-uniform drop temperature as boundary conditions at the liquid/drop interface. The model has been applied to predict the vapour flux distribution for three drop shapes imposing different temperature distribution at the drop surface. The model will be extended to include the solution of the energy equation accounting for the combined effect of heat and mass transfer on a drop evaporating in a gas mixture.

References

[1] Crowe, C.T., Sommerfeld, M., Tsuji, Y., Multiphase Flows with Droplets and Particles, CRC Press, 1998.
[2] Maxwell, J.C., 9th edition, Diffusion, Encyclopaedia Britannica, 1877.
[3] Tonini, S., Cossali, G.E., International Journal of Heat and Mass Transfer 97: 301-7 (2016).
[4] Tonini, S., Cossali, G.E., International Journal of Heat and Mass Transfer 121: 747–758 (2018).
[5] Zubkov, V.S., Cossali, G.E., Tonini, S., Rybdylova, O., Crua, C., Heikal, M., Sazhin, S.S., International Journal of Heat and Mass Transfer 108: 2181–2190 (2017).
[6] Slattery, J.C., Momentum, Energy and Mass Transfer in Continua, 2nd-edition, R. Krieger Publ. New York, 1981.
[7] Moon, P., Spencer, D.E., Field theory handbook: Including Coordinate Systems, Differential Equations and their Solutions, Springer, 2012.
[8] Olver, F.W.J., Lozier, D.W.R., Boisvert, F., Clark, C.W., NIST handbook of Mathematical functions, 2010.

Author index

ISBN – 978-88-97413-27-1